Efficient Numerical Modelling of Wave-Structure Interaction

Philip David Siddorn

Brasenose College

Trinity Term 2012

A thesis submitted in partial fulfilment of the requirements for the degree of Doctor of Philosophy at the University of Oxford

Department of Engineering Science

University of Oxford

Parks Road

Oxford OX1 3PJ

Abstract

Offshore structures are required to survive in extreme wave environments. Historically, the design of these offshore structures and vessels has relied on wave-tank experiments and linear theory. Today, with advances in computing power, it is becoming feasible to supplement these methods of analysis with fully nonlinear numerical simulation.

This thesis is concerned with the development of an efficient method to perform this numerical modelling, in the context of potential flow theory. The interaction of a steep ocean wave with a floating body involves a moving free surface and a wide range of length scales. Attempts to reduce the size of the simulation domain cause problems with wave reflection from the domain edge and with the accurate creation of incident waves.

A method of controlling the wave field around a structure is presented. The ability to effectively damp an outgoing wave in a very short distance is demonstrated. Steep incident waves are generated without the requirement for the wave to evolve over a large time or distance before interaction with the body. This enables a general wave-structure interaction problem to be modelled in a small tank, and behave as if it were surrounded by a large expanse of water.

The suitability of the boundary element method for performing this modelling is analysed. Potential improvements are presented with respect to accuracy, robustness, and computational complexity. Evidence of third order diffraction is found for an FPSO model.

Contents

List of Figures

1 Introduction

1.1 FPSO's in the Ocean Environment

In the design of offshore structures subject to extreme wave environments, fully nonlinear computation is becoming a feasible supplement or alternative to the traditional wave-tank experiments and linear and second order theory in the context of Stokes expansions. The demand for accurate modelling of wave forces and response in steep waves is increasing, driven by the increased exploitation of resources in deep water and exposed environments.

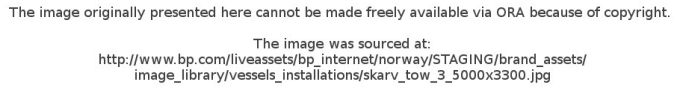

Figure 1: Skarv FPSO ©BP plc.

Of particular current interest is modelling the use of very large turret moored FPSO's (a Floating Production, Storage and Offloading unit) in deep water. A photograph of the Skarv FPSO, which has a length overall of 292 m, is shown in figure 1. While they bear some outward similarity to large trading vessels such as supertankers, there are key differences in their design and use which might be expected to cause the FPSO to suffer increased wave loading.

Kharif and Pelinovsky (2003) report that at least 22 supercarriers were lost

due to rogue waves between 1969 and 1994. In comparison to a trading vessel, an FPSO may operate for longer periods of time in more exposed conditions, and has little means of avoiding large storms.

In addition to the greater wave loading resulting from greater exposure, a report by the Health and Safety Executive (2000) highlighted two key design features of FPSO's (and also Floating Storage Units) which also require attention. Firstly:

- "Trading vessels can be steered into waves but the majority of FPSO/FSUs 'weather vane' and, although wind and wave are sometimes collinear, the wind may often hold a vessel at a heading that will give unfavourable wave direction loading. This could result in greater loads on the side of the vessel, especially if the vessel does not have a lateral control system."

Crossing sea states, in which swell waves from a distant storm combine with wind blowing in a different direction, have the potential to cause large and steep wave events, as discussed by Adcock et al. (2011). For an FPSO the yaw behaviour in these sea states is somewhat unpredictable. As can be seen in figure 1, the sides of the vessel are much lower than the bow, and the impact of a steep wave on the side of the vessel could be extremely dangerous. Even a smaller deviation in heading, of the order of 10°, might result in a large run-up along the side of the vessel and a green water on deck scenario.

A second design feature highlighted by the Health and Safety Executive (2000) report is:

- "FPSO/FSU bow shapes are often rounded, whereas the more pointed bow shapes of trading vessels considerably reduce wave slam loading from head seas."

The flared shape of the bow, which is prominent in figure 1, contributes to highly nonlinear slam loading. Such slam loading has been observed to cause damage in

the case of the Schiehallion FPSO reported by Gorf et al. (2000). The purpose of the high flared bow is to reduce the likelihood of a green water event for a large wave which is met head on, but the effect it has on flow behaviour is not fully understood.

In order to address these issues with FPSO design, there is a requirement for computational techniques which are both efficient and fully nonlinear. While linear and second order modelling remains a useful tool to indicate where potential problems may occur, fully nonlinear codes are required to provide a more accurate indication of slamming and green water events.

Efficient codes are important because the interaction problem involves a wide range of length scales, from long swell waves to very short waves created by nonlinear diffraction. As the order of nonlinearity increases, the wavenumber increases with the square. Thus to resolve third order sum components requires a ninefold increase in resolution. For work in three dimensions, this increase in resolution requires an even greater increase in the number of computational elements. Without a focus on efficiency, this scaling quickly becomes prohibitive.

It would also be beneficial to be able to simulate long time histories. While focussed wave groups, discussed in section 1.4, are both very useful for modelling steep wave events and also conveniently short in duration, for an analysis of FPSO yaw in crossing seas long random sea-state simulations may be required.

1.2 Potential Flow

With the present state of computer hardware, we appear to be in a transitional period where fully nonlinear, three-dimensional and high resolution simulation of FPSO behaviour is becoming viable for the first time. However, for the purpose of this thesis, we retain the simplifying assumption of potential flow theory and the Euler equations, rather than the full rotational Navier-Stokes equations. While we

foresee that fully rotational models will increasingly be used in ocean engineering, at the present moment there is still much to be understood from potential flow modelling.

Potential flow cannot model the effect of flow separation, and the pressure drag that this causes. Lin (2008) argues that potential flow theory is valid only when the body size is much larger than the fluid trajectory under a wave. For the special case of flow past a cylinder, this ratio of the fluid motion to the body size is the well known Keulegan-Carpenter number (Keulegan and Carpenter, 1958). As pointed out by Wu et al. (2001), it is often appropriate to either model the flow as a viscous fluid and neglect the effect of the free surface, or to model the wave diffraction and neglect viscosity.

For waves interacting with an FPSO it is often a reasonable assumption that the fluid motion is small compared to the body, although in very violent flow this may require careful consideraion. Separation may also occur at sharp corners, where locally the body radius is small, but as was mentioned previously we are primarily interested in the behaviour caused by the rounded bow. There are some aspects of the modelling for which potential flow theory is unsuitable, such as the damping of roll motion by a bilge keel, but for analysis of the two design issues identified in section 1.1 potential flow theory provides a useful simplification to the computation.

A particularly problematic location for fluid modelling is the intersection line between the free surface and a body surface. Yeung and Yu (1995) highlighted the importance of the viscous effects at this location. Some of the difficulties associated with the boundary conditions at this location are discussed in section 2.5.

1.3 Computational Methods

In this section we conduct a brief review of the main computational methods which are applied to simulation involving steep ocean waves. The computational methods used have progressed from the mostly two dimensional work reviewed by Tsai and Yue (1996) to mostly three dimensional work reviewed more recently by Dias and Bridges (2006). There are a small variety of methods and implementations in use. This present work builds directly on the Boundary Element Method (BEM) implementation presented in Bai and Eatock Taylor (2006), with subsequent development and application presented in Bai and Eatock Taylor (2007) and Bai and Eatock Taylor (2009). However, many of the new techniques developed in this thesis are of wider application, and are not limited to use by the BEM only.

The fully nonlinear simulation method used throughout this thesis is a variation of the Boundary Element Method (BEM). This has both advantages and disadvantages in comparison to alternative methods, as is discussed below. The primary theoretical advantage is that because of the reduction in the number of dimensions, from the requirement to discretize the entire fluid volume to just the surface, it may be computationally efficient, especially in deep water.

1.3.1 Numerical Wave Tanks

In an attempt to categorize the variety of Numerical Wave Tanks (NWT), a first distinction can be made between "surface-fitting" methods and "surface-capturing" methods. These differ in how the location of the free surface, and functions on the free surface such as velocity, are tracked and used in computation.

Surface-fitting methods use computational nodes located on the free surface, forming a mesh of triangles or quadrilaterals. An arbitrary Lagrangian-Eulerian

(ALE) description is usually used to track the motion of the nodes, maintaining an even coverage of the free surface.

Surface-capturing methods make use of a fixed Cartesian grid, with the moving free surface lying between grid points. These methods are not the focus of this thesis, but some recent examples of their use can be found in Akkerman et al. (2012), Elias et al. (2009), Lee and Mizutani (2009), and Takizawa et al. (2007).

1.3.2 Surface-Fitting Methods

Within the category of surface-fitting methods for irrotational flow, there is a fundamental distinction between volume discretization, usually implemented with the Finite Element Method (FEM), and surface discretization using some form of Boundary Integral Equation (BIE). In the context of three dimensional work, this integral equation is derived from Green's second identity, and the resulting method of solution is known as the BEM. In two dimensions, Green's identity can still be applied, but there is also the alternative of a Cauchy integral formulation.

Two separate FEM implementations which have been extensively tested and continue to be improved are presented in Ma et al. (2001), (with further development in Ma and Yan (2006) and Ma and Yan (2009)) and Wang and Wu (2006) (with following work in Wang et al. (2007)). Finite element methods are reasonably well understood and very widely used in other areas of engineering.

Boundary element methods are less widely used outside the field of Ocean Engineering, and as a result there is considerable variety in the form of BEM used. Constant panel methods were originally popular but have fallen out of favour to the development of higher order elements. There are alternative methods for force calculation. The choice of time integration is not settled, with investigations into Runge-Kutta, predictor-corrector, Taylor series expansion and symplectic methods.

For the purposes of this work the "standard" BEM is presented in Bai and

Eatock Taylor (2006). Other recent BEM implementations and applications to various water wave problems include Celebi et al. (1998), Liu et al. (2001), Grilli et al. (2001), (with further work in Fochesato et al. (2005) and Fochesato and Dias (2006)), Boo (2002), Ferrant et al. (2003), Hamano et al. (2003), Sung and Grilli (2008), and Sun and Faltinsen (2009). It is also possible to couple a BEM with a FEM, as demonstrated in Eatock Taylor et al. (2008), in order to take advantage of their relative strengths and weaknesses.

In comparison with the FEM, the BEM has a reduced number of unknowns due to only discretizing the surface. It might therefore be expected to be computationally faster for large problems, particularly for deep water. However, the interaction matrix for the FEM is narrow banded, compared to the full banded BEM, and this causes the straightforward BEM to scale badly.

An important algorithm for improving the performance of the BEM is the Fast Multipole Method (FMM). This significantly accelerates the calculation of the interaction between all nodes of the discretized surface. The FMM was first developed in Greengard and Rokhlin (1987) and Greengard and Rokhlin (1997), and in the context of water waves has been implemented by Utsunomiya et al. (2001), for open water by Fochesato and Dias (2006), and for diffraction and radiation problems by Borgarino et al. (2011).

1.4 Focussed Wave Groups

Many wave tank experiments, both physical and numerical, involve the generation of a focussed wave group as an incident wave. These groups are convenient to work with because they are limited in both time and space, requiring only moderately large wave tanks and short experiments. The focussing enables a very steep wave event to be created from generation of much lower amplitude waves.

Perhaps more importantly, focussed wave groups provide a useful model for

large ocean waves. Lindgren (1970) and Boccotti (1983) showed that for a linear random model of wave generation, the average shape of a large crest is a scaled autocorrelation function. In offshore engineering a wave of this type is commonly known as a NewWave .

The idea behind NewWave is that a sea state consists of a superposition of independent sinusoidal components, each with random phase, and with amplitude given by a spectrum such as Jonswap (Hasselmann et al., 1973). The largest waves are expected when there is phase congruence, so that many of the independent components contribute positively towards a large elevation. The full derivation of this theory was given by Tromans et al. (1991).

The shape of a steep ocean wave is altered by local nonlinear effects as the wave components come into focus. The NewWave model has been verified to accurately represent the linearized behaviour of large offshore waves observed in field data by Jonathan and Taylor (1997). Modification of the NewWave profile to include nonlinear corrections up to fifth order has been performed by Walker (2006), in order to represent the extremely large Draupner New Year wave analysed by Hagen (2002).

Due to a nonlinear instability, very large long-crested waves occur more often than predicted by linear random models (Dysthe et al., 2008). The assumption of a linear random process provides a useful approximation to the shape of many large wave events, but the nonlinear effects should be taken into account when considering the statistics of how often these large waves occur.

1.5 Wave Generation and Damping

For any simulation method, it is important to minimize the size of computational domain, both in time and space. The use of a focussed wave group can help with this. In principle only a small region of water needs to be simulated for a short

duration of time. In practice, problems with wave reflection from the numerical tank walls and the nonlinear components of an incident wave can require a much larger region to be simulated, for a longer time.

An ideal NWT would be able to create a specified design wave, which then interacts with a structure and behaves as if it were free to propagate out into a large expanse of water. However in both experimental and computational work we are constrained to working within a limited domain. The main difficulty this causes is due to the interference of reflected waves from the domain boundary. To mitigate this problem there is a compromise between using a larger low resolution wave tank, or performing simulations of very short duration.

Damping regions, in which an outgoing wave is absorbed, have been implemented previously, but generally suffer from large reflection coefficients. Existing methods, which use either a surface treatment as in Kwon et al. (2003), a piston-like wall condition such as Duclos et al. (2001), or a combination such as Clement (1996), all require a large amount of space to achieve the wave damping, or otherwise relatively large waves will be reflected back into the wave tank. This presents a significant problem, as either the extra space quickly becomes prohibitively computationally expensive, or only simulations of very short duration can be performed. An improved method of wave damping was presented in Clamond et al. (2005) in the context of a spectral scheme, which is unsuitable for modelling the interaction with a solid body of general geometry.

A related problem is the generation of an incident wave, including the reproduction of waves observed in experiment. The usual method of wave generation is to model the dynamics of a piston wave-maker. Westphalen et al. (2012) demonstrated the reproduction of very steep focussed wave groups by this method. However this procedure requires significant effort to calculate the flow near the piston, and a long domain to avoid interference from nonlinear error waves. A more compact wave generation method, capable of generating steep

groups without much extra space would be of great benefit.

A new method for wave damping and generation presented in this thesis allows the computational domain to be kept very small. Although this new method is applied to simulations based on the BEM, in principle it could also be applied to any other form of numerical wave tank.

1.6 Aims of the Thesis

1. Demonstrate the performance of a new method of wave damping in a numerical wave tank. This enables the use of very small computational domains, making it possible to perform high resolution simulation of nonlinear problems.

2. Demonstrate the ability of the method to accurately create arbitrary incident waves, which may be both steep and multi-directional.

3. Investigate the nonlinear fluid dynamics associated with the interaction of steep waves and an FPSO. Of particular importance is the highly nonlinear behaviour created at the bow.

1.7 Structure of the Thesis

In sections 2 and 3 we develop and extend a numerical method for fluid simulation. This includes both previous work by other authors and new work which is presented here for the first time. A distinction is made between the work in section 3, which is applicable only within the context of the BEM, and the work in section 2, which may also be applicable to other simulation methods such as the FEM or surface-capturing schemes.

In section 4 we present a major development of this thesis: a method for the damping and generation of waves within a numerical wave tank. The equations

for wave damping follow from the work in a spectral scheme described in Clamond et al. (2005). We extend this to an unstructured grid and apply it to the generation of experimental waves for the first time.

In sections 5 and 6 we demonstrate the performance of the numerical method by comparsion with three sets of experimental data. By application of the new wave damping/generation method we are able to obtain results using very small numerical wave tanks.

The first comparison in section 5.1 is made with experiments performed with a bottom mounted cylinder in the shallow water basin at DHI, reported in Zang et al. (2010). For this geometry we demonstrate the reproduction of an experimental wave by the new wave generation method, and the accuracy of the force calculation

The second experimental comparison in section 5.2 is with an oscillating cone reported in Drake et al. (2009). This choice of geometry is motivated by the flared shape of an FPSO bow. We achieve good results for both the force and run-up in a very small wave tank, using the new damping method to prevent reflection from the tank walls.

The third comparison in section 6 is with an FPSO model used in experiments reported by Zang et al. (2006). For this geometry we not only obtain good agreement with the experimental data, but also are able to perform a further analysis and visualization of the nonlinear flow behaviour. This includes the identification of second and third order free waves created by the diffraction.

Finally in section 7 we conclude by summarizing the achievments of this project, and describing relevant further work.

2 Fluid Modelling

In this section we investigate the suitability of the BEM for modelling the interaction of steep waves with floating bodies. We first review the established method, similar to that presented in Bai and Eatock Taylor (2006). We then identify the primary issues which impose limits on its use. In the remaining sections of this chapter we discuss new extensions to the established method which aim to address these issues.

2.1 Review

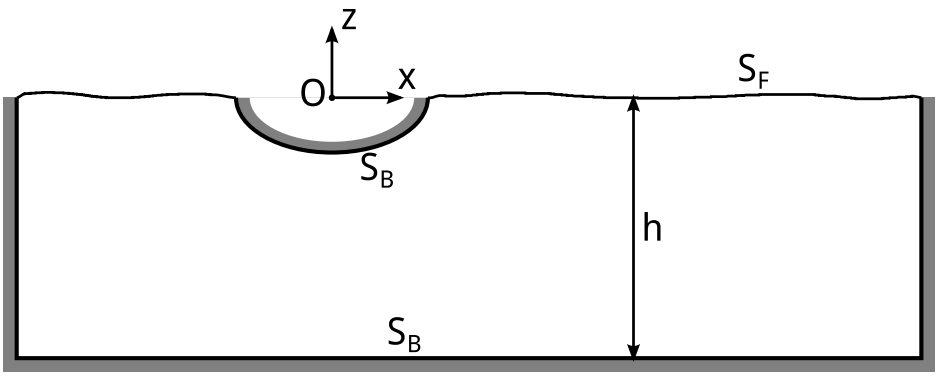

Figure 2: Definition sketch

The motion of a Newtonian fluid in a wave tank satisfies the Navier-Stokes equations, with the material derivative:

$$\frac{\mathrm{D}\mathbf{v}}{\mathrm{D}t} = -\frac{1}{\rho}\nabla p + \frac{\mu}{\rho}\nabla^2\mathbf{v} - \mathbf{g}, \tag{1}$$

where the symbols have the usual meanings: $\mathbf{v}$ velocity, t time, ρ density, p gauge pressure, μ viscosity and $\mathbf{g}$ acceleration due to gravity. We assume incompressible flow, which implies the continuity condition:

$$\nabla \cdot \mathbf{v} = 0. \tag{2}$$

On the solid surfaces S_B, there is the no-slip boundary condition:

$$\mathbf{v} = \mathbf{v}_B \in S_B, \tag{3}$$

where $\mathbf{v}_B$ is the velocity of a surface position on the solid surface. On the free surface S_F, the fluid pressure is assumed equal to the undisturbed atmospheric pressure:

$$p = 0 \in S_F, \tag{4}$$

We now seek to assume irrotational flow, and remove the dependence on viscosity. By Helmholtz decomposition the fluid velocity can be decomposed into the sum of an irrotational and rotational part:

$$\mathbf{v} = \nabla\phi + \nabla \times \mathbf{A}, \tag{5}$$

and we set $\mathbf{A} = 0$, $\mathbf{v} = \nabla\phi$.

The irrotational part of the velocity alone cannot in general satisfy the no-slip boundary condition (3). The usual assumption is to enforce instead the no-penetration condition, which is associated with setting $\mu = 0$:

$$\frac{\partial\phi}{\partial n} = \mathbf{v}_B \cdot \mathbf{n} \in S_B. \tag{6}$$

It should be noted that this boundary condition, while widely used and normally taken without argument, does introduce some inconsistency with the physical condition (3). In the treatment of full rotational problems, it can be seen that the irrotational part alone does not exactly satisfy (6). We will return to this issue in the discussion of corner points in section 2.5, where enforcing the no-penetration condition may lead to large and non-physical slip velocities.

The velocity potential ϕ must satisfy the incompressible continuity condition

(2). This is also the case even if the rotational component is not neglected, as $\nabla \times \mathbf{A}$ is solenoidal. This results in the Laplace equation:

$$\Delta\phi = 0. \tag{7}$$

Assuming irrotational flow, the dependence on viscosity in (1) vanishes:

$$\frac{\mathrm{D}}{\mathrm{Dt}}\nabla\phi = -\frac{1}{\rho}\nabla p - \mathbf{g}. \tag{8}$$

We now remove the gradient from both sides, and insert the pressure condition (4) to get the dynamic boundary condition on the free surface:

$$\frac{\mathrm{D}\phi}{\mathrm{D}t} = -g\eta + \frac{1}{2}\left|\nabla\phi\right|^2 \in S_F, \tag{9}$$

which is the time dependent version of the Bernoulli equation. Finally we also apply the kinematic boundary condition that fluid particles move at the fluid velocity:

$$\frac{\mathrm{D}\mathbf{x}}{\mathrm{D}t} = \nabla\phi \in S_F. \tag{10}$$

The equations (9) and (10) are now suitable for time-stepping the location $\mathbf{x}$ and potential ϕ of nodes on the free surface. At each timestep we can set up a mixed boundary value Laplace problem. The location of the moving free surface is found by integration of (10). The Dirichlet data ϕ is known on the free surface from integration of (9) , and the Neumann data $\frac{\partial\phi}{\partial n}$ is known on the body surfaces from the no-penetration condition (6).

2.2 Time-stepping

The integration of equations (9) and (10) is performed by solving the Laplace problem at discrete time steps. The most commonly used method is the 4th

order Runge-Kutta integrator, although alternatives such as predictor-corrector methods and Taylor series have been used successfully.

The most efficient and accurate method for time-stepping is still an open area of discussion. Clamond et al. (2007) argue in favour of an explicit method with variable timestep, such as the Runge-Kutta-Fehlberg integrator. However, this is in the context of a spectral scheme, where the representation in terms of Fourier components allows the linear contribution to be integrated without error for large timesteps. In a non-spectral scheme, the high frequency linear components can not be treated so easily, and this may reduce the potential benefit of a variable step size.

It might be expected that symplectic integrators would be appropriate for the treatment of water waves, due to their ability to conserve energy evenly at all frequencies. However, improved performance is yet to be demonstrated. Many numerical wave tanks rely on smoothing of the high wavenumber components to maintain numerical stability, and this removes much of the potential benefit of a symplectic method. Where no smoothing is used, symplectic methods have problems with stability, as reported by Clamond et al. (2007).

2.3 Re-meshing

The fluid is tracked by the location and velocity potential of nodes on the free surface. These nodes move with the fluid , and so in the simulation of steep waves they may drift considerably from their starting locations. This causes distortion of the triangular mesh required by the Laplace solver. We apply re-meshing to maintain a high quality mesh on the free surface. The trigger condition for the re-meshing is the length of any edge in the traingular mesh changing by more than 20% from its original length. The re-meshing makes use of the same shape functions as the Laplace solver, described in section 3.1.1.

Re-meshing in this way should allow for the simulation of a solid body travelling through or being inserted into the fluid. As the length of the intersection line between the solid body and free surface changes, so does the number of nodes, in order to maintain a similar resolution. However, changing the number and the location of the nodes on the intersection line in this way was observed to have an adverse effect on the stability and accuracy of the solution. Because of this problem, the nodes on the intersection line were only moved back to their original locations around the body in the re-meshing process.

2.4 Force Calculation

The hydrodynamic force and moment acting on a solid object may be found by integrating the pressure over the wetted surface. It is possible to calculate the pressure by rearranging (8):

$$\frac{p}{\rho} = -gz - \frac{\partial \phi}{\partial t} - \frac{1}{2}\nabla\phi \cdot \nabla\phi. \tag{11}$$

However, this evaluation requires knowledge of the time derivative $\frac{\partial \phi}{\partial t}$. This may be found by some form of numerical differentiation but this method has been reported to be inaccurate.

An alternatic method to calculate $\phi_t = \frac{\partial \phi}{\partial t}$ is to solve an additional boundary value problem. This has the same structure as the boundary value problem for ϕ, with the Dirichlet data on the free surface and the Neumann data on the body surfaces. On the free surface, ϕ_t is found from the Eulerian form of (9):

$$\phi_t = -g\eta - \frac{1}{2}\left|\nabla\phi\right|^2 \in S_F. \tag{12}$$

Following Wu (1998), on the solid boundaries we have

$$\frac{\partial \phi_t}{\partial n} = \left(\dot{U} + \dot{\Omega} \times X\right) \cdot \mathbf{n} - U \cdot \frac{\partial \nabla \phi}{\partial n} + \Omega \frac{\partial}{\partial n} \left[X \times (U - \nabla \phi)\right] \in S_B, \qquad (13)$$

where U and $\dot{U}$ are the translational velocity and acceleration of the body, and Ω and $\dot{\Omega}$ are the rotational velocity and acceleration relative to a body fixed coordinate X. On fixed surfaces such as tank walls or the sea bed equation (13) is simply $\partial \phi_t / \partial n = 0$.

In the case of a freely floating or moored object, we have the problem that the body acceleration required in (13) is not known until after the force acting on the body has been found. This circular dependency can be resolved by two different methods.

In the method of Wu and Eatock Taylor (1996) six auxiliary functions are introduced, one for each independent component of force and moment, and six new boundary value problems are solved, requiring six extra applications of the boundary element method. Whether this requires significantly more computational time depends on the method used to solve the system of equations. Each boundary value problem can be represented by the matrix equation $\mathbf{A}\mathbf{x}_i = \mathbf{b}_i$, where the matrix $\mathbf{A}$ is the same for both the velocity potential and all the auxiliary functions. In the case that a direct solver is used, then solving for multiple right hand side vectors $\mathbf{b}_i$ is not a problem. If an iterative solver is used however, the same savings cannot be made, and calculation of force by this method becomes relatively expensive.

The method of Ma and Yan (2009) is to use a timestepping scheme they refer to as ISITIMFB-M (iterative semi-implicit time integration method for floating bodies - modified). This method involves predicting the body acceleration and velocity by a curve fitting of the acceleration at previous timesteps. The predicted motion is used to calculate the force, which is then used to correct the

estimation of the acceleration. This prediction and correction step is iterated until a convergence criterion is met. While each iteration does require an expensive boundary element method calculation, these iterations are already required by semi-implicit scheme to calculate the fluid motion.

In the present work computations are performed only with fixed or forced bodies, and so both the body velocity and acceleration is known in advance, and there is no difficulty with equation (13). If freely moving bodies were to be simulated, the calculation of the force and body motion would require the use of either additional boundary value problems or an iterative time-stepping scheme.

2.5 Intersection Treatment

A major problem which limits the usefulness of the BEM, and surface-fitting methods in general, is the robustness of the scheme. Due to the lack of energy dissipation, there is a tendency for the highest wavenumber oscillations to be numerically unstable. In two-dimensions this leads to the "saw-tooth" instability. In three dimensions this problem is generally less severe, as the wave energy can more easily radiate outwards away from the direction of wave advance.

At the intersection line, where the free surface and body surface meet, the numerical problems are compounded by the physical behaviour of the fluid. This is made worse by the presence of flare (e.g. at the bow of an FPSO). The entry of a solid object into water often causes the formation of very thin jets of water. Not only do these features lead to overturning and local wave breaking, but their calculation is highly dependent on the local resolution of the mesh, causing the appearance of a saw-tooth pattern around the perimeter of a body.

One cause of numerical instability is a mismatch in resolution between the free and solid surfaces. If the solid surface is lacking in elements, then it cannot represent the depth variation of the higher wavenumbers. This results in an in-

accurate calculation of the free surface velocity. In the general case, the elements on a solid surface must be able to represent not only the progressive wave components, which decrease exponentially with depth, and require high resolution near the free surface, but also the evanescent wave components, which have a sinusoidal variation with depth.

2.5.1 Boundary condition

The implied boundary conditions at the intersection line may require some attention. As mentioned in section 2.1, the boundary condition in potential flow theory is the no-penetration condition. However, as discussed at length in the book by Joseph et al. (2007), when considering the velocity as a Helmholtz decomposition into an irrotational and rotational part, it is not the case in general that the irrotational part satisfies the no-penetration condition by itself. The application of this boundary condition might be expected to cause very large slip velocities, which are non-physical for a real fluid with non-zero viscosity, and this may contribute to instability.

Even for rotational flow simulations, the choice of boundary condition is not clear. As discussed in Wu et al. (2001), the no-shear condition may be more appropriate than the theoretical no-slip condition. The issue is that the boundary layer flow can be contained in a very small region, and hence the velocity gradients at an intersection line can be very large. A no-slip condition cannot be accurately imposed unless these velocity gradients can be adequately represented within the resolution of the simulation.

In the results presented in this thesis we have used the conventional no-penetration condition of potential flow theory. However, for future work, particularly regarding slam loading, it may be worthwhile to investigate alternatives such as a Robin boundary condition on the solid surface, in order both reduce numerical problems and more accurately represent the behaviour of real flow.

2.5.2 Velocity compatibility

Following the BEM calculation, the velocity at nodes on the intersection line is overdetermined. We have three components of velocity: The no-penetration condition, the tangential surface velocity from the derivative of ϕ, and the normal velocity which is the output of the BEM. Ideally the BEM would provide a velocity which is compatible with the already known components, but in practice this is not the case. As discussed by Grilli and Svendsen (1990), the possible corner singularity and the inaccuracy of the numerical integration in this region leads to a compatibility issue when combined with the use of double nodes. This problem is made worse in the simulation of steep waves, as very short waves may be formed at the intersection, which havelarge velocity gradients but cannot be treated accurately due to the limited resolution. There are several possible methods to resolve the situation.

We have the body velocity $\mathbf{v}_B$, the tangential part of the surface velocity v_t, and the normal part of the surface velocity q. The most straightforward solution would be to ignore the value of v_t, and instead just use $\mathbf{v}_B$ and q. However, this is observed to cause problems with stability. As the curvature of the mesh increases, and the surface gradient is different between neighbouring nodes, the enforced tangential velocity pushes the nodes in different directions, and increases the difference in gradient. The calculated normal velocity q can only be regarded as approximate, incorporating from both the long wavelengths and also wavelengths which are shorter than the resolution of the mesh.

A more stable alternative is to first take the velocity from v_t and q, and then enforce $\mathbf{v}_B$ by adding a component normal to the body surface. As this fixing direction is not dependent on the fluid surface gradient it does not cause instability. This procedure was used in the code described in Bai and Eatock Taylor (2007). For structures with vertical sides this method works well. Unfortunately, if the

body does not have vertical sides then this procedure can add energy to the fluid, leading to inaccurate results.

A method which was found to work reasonably well is to combine v_t and q, and then enforce $\mathbf{v}_B$ by adding an extra horizontal component. Conservation of energy is implied by the dynamic boundary condition (9), and it was found to be important that the compatibility correction did not break this by altering the vertical velocity. This method appears to give accurate results in all cases considered here. There remain issues with robustness and stability at large amplitude, which may be linked to the choice of boundary condition and the physical fluid behaviour.

2.6 Frequency Component Analysis

In order to understand the behaviour of a nonlinear flow, it can be instructive to perform a Stokes type expansion and decompose the total force or elevation into linear and nonlinear components. The modern application of Stokes expansions to analyse nonlinear water waves follows from the work of Longuet-Higgins (1962). The wave elevation and velocity potential is expressed as a pertubation series with the amplitude, and then the free surface boundary conditions are applied. For a full treatment of the topic, refer to the book by Dean and Dalrymple (1991)

In a similar manner to Fitzgerald et al. (2012), for the elevation we can write to 4th order:

$$\begin{aligned}
\eta\left(A,\theta\right) &= \eta_{11}A\cos\theta \\
&+ \eta_{20}A^2 + \eta_{22}A^2\cos 2\theta \\
&+ \eta_{31}A^3\cos\theta + \eta_{33}A^3\cos 3\theta \\
&+ \eta_{40}A^4 + \eta_{42}A^4\cos 2\theta + \eta_{44}A^4\cos 4\theta, \qquad (14)
\end{aligned}$$

where A and θ are the amplitude and phase of an incident wave group. The coefficients η_{11} etc. represent transfer functions from the imposed oscillation to the observed elevation.

The η_{11} component is called the linear term. For small amplitudes this dominates, as the higher order nonlinear terms are multiplied by higher powers of A. The frequencies of the nonlinear terms are the harmonics of the linear part. This includes difference frequency components such as η_{20} and sum frequency components such as η_{22}

We would like to be able to extract each of the nonlinear components independently, as this tells us how the elevation response changes with varying amplitude. For a narrow banded incident spectrum, part of this separation may be performed by frequency filtering, because each harmonic has a different frequency range. However for a broad spectrum, these frequency ranges overlap, and the frequency filtering is not accurate.

A method to cleanly separate the harmonics is to perform simulations or experiments with different phase, and then calculate linear combinations from the result. If we add the wave elevation resulting from a group with phase $\theta = 0°$ to the inverted group with phase $\theta = 180°$ we obtain from (14):

$$\left(\eta\left(A, 0°\right) + \eta\left(A, 180°\right)\right)/2 = \eta_{20}A^2 + \eta_{22}A^2 + \eta_{40}A^4 + \eta_{42}A^4 + \eta_{44}A^4, \qquad (15)$$

in which only the even harmonics remain. If we instead subtract the elevations we obtain:

$$\left(\eta\left(A, 0°\right) - \eta\left(A, 180°\right)\right)/2 = \eta_{11}A + \eta_{31}A^3 + \eta_{33}A^3, \qquad (16)$$

in which only the odd harmonics remain.

This linear combination provides a separation between the frequency bands, and allows frequency filtering to be used. For example the second order difference term η_{20} cannot usually be filtered from the large linear term η_{11}, as the frequency ranges overlap. It can however be filtered from the second order sum term η_{22}, as this has a much higher frequency.

The procedure may be extended by combining more waves with different phase, and more details of the useful combinations are given in section (8.2). In particular we have made use of the triple harmonics combination:

$$\left(\eta\left(A, 0^{\circ}\right) + \eta\left(A, 120^{\circ}\right) + \eta\left(A, 240^{\circ}\right)\right)/3 = \eta_{20}A^2 + \eta_{33}A^3 + \eta_{40}A^4, \qquad (17)$$

as this allows a clean separation of the third order sum term, without any contribution from the linear component.

In the following text a phase of 0° is conventionally referred to as crest focussed, and 180° as trough focussed.

3 Boundary Element Method

3.1 Laplace Solver

The BEM solves the Laplace problem by means of an integral equation over the surface, avoiding any volume integrals. We start with the general form of Green's second identity:

$$\int_V \left[u\nabla^2 \upsilon - \upsilon\nabla^2 u\right] \mathrm{d}V = \int_S u\frac{\partial \upsilon}{\partial n} - \upsilon\frac{\partial u}{\partial n}\mathrm{d}S. \tag{18}$$

By letting $\upsilon = \phi$, and choosing u to be the free space Green's function $1/4\pi r$, centred at an arbitrary point $\mathbf{x}$ within the domain, we obtain:

$$\phi(\mathbf{x}) = \int_S \left[G(\mathbf{x},\mathbf{y})\frac{\partial \phi}{\partial n}(\mathbf{y}) - F(\mathbf{x},\mathbf{y})\phi(\mathbf{y})\right] \mathrm{d}S(\mathbf{y}),\ \forall \mathbf{x} \in V, \tag{19}$$

where the kernel functions are the monopole

$$G(\mathbf{x},\mathbf{y}) = \frac{1}{4\pi r}, \tag{20}$$

and the dipole

$$F(\mathbf{x},\mathbf{y}) \equiv \frac{\partial G(\mathbf{x},\mathbf{y})}{\partial n(\mathbf{y})} = -\frac{1}{4\pi r^2}\frac{\partial r}{\partial n(\mathbf{y})}. \tag{21}$$

By considering the limit as the point $\mathbf{x}$ moves onto the border of the domain, we find the conventional boundary integral equation (Liu, 2009):

$$c(\mathbf{x})\phi(\mathbf{x}) = \int_S \left[G(\mathbf{x},\mathbf{y})\frac{\partial \phi}{\partial n}(\mathbf{y}) - F(\mathbf{x},\mathbf{y})\phi(\mathbf{y})\right] \mathrm{d}S(\mathbf{y}),\ \forall \mathbf{x} \in S, \tag{22}$$

in which $c(\mathbf{x})$ is the solid angle enclosed by the surface of the domain at that point.

The solid angle $c(\mathbf{x})$ may be calculated directly from the surface geometry. Alternatively, the approach used in Bai and Eatock Taylor (2006) is to make use of an integral identity to eliminate it. By considering the case of a unit potential $\phi = 1$, $\frac{\partial \phi}{\partial n} = 0$, we can express the solid angle as:

$$c(\mathbf{x}) = -\int_S F(\mathbf{x}, \mathbf{y}) \, \mathrm{d}S(\mathbf{y}), \tag{23}$$

and then substituting into (22) we get the weakly singular boundary integral equation:

$$\int_S F(\mathbf{x}, \mathbf{y}) \left[\phi(\mathbf{y}) - \phi(\mathbf{x})\right] \mathrm{d}S(\mathbf{y}) = \int_S G(\mathbf{x}, \mathbf{y}) \frac{\partial \phi}{\partial n}(\mathbf{y}) \, \mathrm{d}S(\mathbf{y}), \; \forall \mathbf{x} \in S. \tag{24}$$

An advantage of using integral equation (24) over (22) is that the integral with the F kernel is singular as $r \to 0$, and applying the integral identity reduces the order of the singularity. Because for small r the term $[\phi(\mathbf{y}) - \phi(\mathbf{x})]$ is $O(r)$, the $1/r^2$ singularity of the F kernel is reduced to $1/r$. As reported in Ning et al. (2010), either of these integral equations may be used, with identical results if implemented correctly.

The near-singular contributions to the integrals require some care to evaluate. Special numerical techniques such as adaptive integration or coordinate transformations may be used. In an attempt to avoid the need for this, it is possible to completely remove the singularity in both the F and G integrals by applying another integral identity. This is discussed in section 3.2.

3.1.1 Discretization

To form a system of equations from the boundary integral equation (24), the free surface and solid surface must be discretized. This is here achieved by the use of quadratic isoparametric elements. The free surface is represented by an

unstructured mesh of six node triangular elements. An unstructured mesh is sufficiently flexible to be able to fit the perimeter of an arbitrary body while avoiding elements with very small or large angles. If the surface is assumed to be non-overturning, then the mesh generation can be performed by a fast two-dimensional triangularization. We use the freely available software TRIANGLE, described in Shewchuk (1996).

The solid surfaces are represented by a structured mesh of eight node quadrilateral elements. For simple geometries, such as the walls of a wave tank or a bottom-mounted cylinder, the structured mesh generation is straightforward. For bodies which do not reach the bottom of the tank, such as a cone or a mesh representing a ship's hull, the discretization follows the pattern of the lines of latitude and longitude on a globe. The lowest quadrilateral elements are degenerate triangles, sharing a single node at the pole, but the low quality of the mesh in this region has not been observed to cause any difficulties.

The discretization allows the integrals in (24) to be evaluated by the use of Gauss-Legendre sampling points. We can write the continuous integral as a discrete sum over a total of M sampling points distributed over the free surface and body surfaces

$$\sum_{m=1}^{M} F\left(\mathbf{x}, \mathbf{y}_m\right) \phi_m w_m - \phi\left(\mathbf{x}\right) \sum_{m=1}^{M} F\left(\mathbf{x}, \mathbf{y}_m\right) w_m = \sum_{m=1}^{M} G\left(\mathbf{x}, \mathbf{y}_m\right) q_m w_m, \; \forall \mathbf{x} \in S \quad (25)$$

This summation is valid for any point $\mathbf{x}$ on the surface. The sampling point weight w_m is the multiple of the local Jacobian and the weight given to this point by the integration rule. The values $\mathbf{y}_m$, ϕ_m and $q_m = \partial\phi/\partial\hat{n}$ are the coordinate, velocity potential and normal velocity at sampling point m. These sampling point

values are related to the nodal values by the use of shape functions $N_j(\xi_1, \xi_2)$:

$$\mathbf{y}_m(\xi_1, \xi_2) = \sum N_{k,m}(\xi_1, \xi_2)\, \mathbf{x}_k, \tag{26}$$

$$\phi_m(\xi_1, \xi_2) = \sum N_{k,m}(\xi_1, \xi_2)\, \phi_k, \tag{27}$$

$$q_m(\xi_1, \xi_2) = \sum N_{k,m}(\xi_1, \xi_2)\, \left.\frac{\partial \phi}{\partial n}\right|_k, \tag{28}$$

where (ξ_1,ξ_2) are local coordinates within an element.

By evaluating (25) at every node, we can represent the whole system as a matrix equation of the form

$$\left[\begin{array}{cc} \mathbf{A}^B & \mathbf{A}^F \end{array}\right] \Phi_{\text{unknown}} = \left[\begin{array}{cc} \mathbf{B}^B & \mathbf{B}^F \end{array}\right] \Phi_{\text{known}}. \tag{29}$$

The known vector is comprised of the Neumann data at body nodes, combined with the Dirichlet data at free surface nodes:

$$\Phi_{\text{known}} = \{q_{B1},\, q_{B2},\, \ldots, q_{BN_B},\, \phi_{F1},\, \phi_{F2},\, \ldots \phi_{FN_F}\}, \tag{30}$$

while the vector of unknowns is the complementary data:

$$\Phi_{\text{unknown}} = \{\phi_{B1},\, \phi_{B2},\, \ldots \phi_{BN_B},\, q_{F1},\, q_{F2},\, \ldots, q_{FN_F}\}. \tag{31}$$

The matrices $\mathbf{A}$ and $\mathbf{B}$ represent the combination of application of the shape functions to find the sampling point data from the nodal data, the appropriate weighting for each sampling point, and then the multiplication by the kernel function G or F. The left portion of each matrix corresponds to the contribution from body surface nodes, while the right portion corresponds to the free surface

nodes. By rearranging (25), we can write:

$$\begin{aligned}
\mathbf{A}^B &= \mathbf{F}^B \times \operatorname{diag}\left(\mathbf{w}^B\right) \times \mathbf{N}^B - \operatorname{diag}\left(\mathbf{F}^B \mathbf{w}^B\right), \\
\mathbf{A}^F &= -\mathbf{G}^F \times \operatorname{diag}\left(\mathbf{w}^F\right) \times \mathbf{N}^F, \\
\mathbf{B}^B &= \mathbf{G}^B \times \operatorname{diag}\left(\mathbf{w}^B\right) \times \mathbf{N}^B, \\
\mathbf{B}^F &= -\mathbf{F}^F \times \operatorname{diag}\left(\mathbf{w}^F\right) \times \mathbf{N}^F + \operatorname{diag}\left(\mathbf{F}^F \mathbf{w}^F\right). \qquad (32)
\end{aligned}$$

The matrices $\mathbf{G}^B$, $\mathbf{G}^F$, $\mathbf{F}^B$, and $\mathbf{F}^F$ are the kernel matrices. Each element is the result of evaluating one of the two kernel functions (20) or (21) between a node and a sampling point. Each row of these matrices corresponds to a single node. Each column corresponds to a single sampling point. These matrices are not square, the kernel matrix $\mathbf{G}^B$ covers every node on all surfaces, but only the sampling points on the body surface. Likewise the $\mathbf{G}^F$ matrix covers every node, but only the sampling points on the free surface, and similarly for the F kernel matrices.

The weighting vectors $\mathbf{w}^B$ and $\mathbf{w}^F$represent the integral weight and the Jacobian at each sampling point. $\mathbf{w}^B$ contains values for the body surface sampling points and $\mathbf{w}^F$ the free surface sampling points. The notation $\operatorname{diag}(\cdot)$ refers to creating a diagonal matrix from a vector.

The shape function matrices $\mathbf{N}^B$ and $\mathbf{N}^F$ transform the nodal data to sampling point data. Each row of $\mathbf{N}^B$ corresponds to a sampling point on a body surface, while each column corresponds to a node on a body surface, and similarly for $\mathbf{N}^F$. These matrices are very sparse, as the values at each sampling point only depend on the nodes which comprise that element, six for triangular quadratic elements elements and eight for quadrilateral quadratic elements.

After the matrices $\mathbf{A}$ and $\mathbf{B}$ are calculated, the matrix equation (29) may be solved by a standard method such as LU decomposition or a Krylov subspace

method.

3.1.2 Fast Multipole Method

For a simulation with a large number of nodes, the matrices in (29) become very large, and solving the system of equations becomes very time consuming. If we consider a three dimensional simulation of resolution k, then the number of nodes required is $O(k^2)$, and the size of the matrices is $O(k^4)$. This rapid increase in complexity limits the feasibility of high-resolution simulations. Fortunately, it is possible to avoid the need to calculate each element of these large matrices, by application of the Fast Multipole Method.

The only full matrices which appear in (32) are the kernel matrices, which involve the calculation of a $1/r$ or $1/r^2$ kernel between every pair of nodes and sampling points. If there are N nodes in the simulation, then this is an $O(N^2)$ calculation. By exploiting the behaviour of the Laplace kernels and grouping together distant interactions, the FMM can reduce this to $O(N)$ (Greengard and Rokhlin, 1987). For a parallel implementation of the algorithm, Greengard and Gropp (1990) showed that the expected time requirement grows as $\log P$ when dividing the work across P processors, and Cruz et al. (2010) report over 85% parallel efficiency using 64 processors.

By applying the FMM we can calculate the matrix products in (29) without actually forming the full matrices. This is sufficient for the use of an iterative solver, but removes the possibility of using a direct solver.

The FMM works by expressing the kernel function as an expansion about a point $\mathbf{y}_c$:

$$G(\mathbf{x}, \mathbf{y}) = \sum_i G_i^x(\mathbf{x}, \mathbf{y}_c) G_i^y(\mathbf{y}, \mathbf{y}_c). \tag{33}$$

By using an expansion of this form, the integral can be rewritten to avoid the

pairing of all sampling points and nodes.

$$\int G(\mathbf{x},\mathbf{y})\, q(\mathbf{y})\, \mathrm{d}S(\mathbf{y}) = \sum_i G_i^x(\mathbf{x},\mathbf{y}_c) \int G_i^y(\mathbf{y},\mathbf{y}_c)\, q(\mathbf{y})\, \mathrm{d}S(\mathbf{y}). \tag{34}$$

For the three-dimensional Laplace problem, the expansions used for the kernels (20) and (21) are

$$G(\mathbf{x},\mathbf{y}) = \frac{1}{4\pi} \sum_{n=0}^{\infty} \sum_{m=-n}^{n} \overline{S_{n,m}}(\mathbf{x}-\mathbf{y}_c)\, R_{n,m}(\mathbf{y}-\mathbf{y_c}), \tag{35}$$

$$F(\mathbf{x},\mathbf{y}) = \frac{1}{4\pi} \sum_{n=0}^{\infty} \sum_{m=-n}^{n} \overline{S_{n,m}}(\mathbf{x}-\mathbf{y}_c)\, \frac{\partial R_{n,m}(\mathbf{y}-\mathbf{y_c})}{\partial n(\mathbf{y})}, \tag{36}$$

which is valid as long as the expansion point is closer to the sampling point than the node,

$$|\mathbf{y}-\mathbf{y}_c| < |\mathbf{x}-\mathbf{y}_c|. \tag{37}$$

The solid harmonic functions $R_{n,m}$ and $S_{n,m}$ in (35) and (36) are given by

$$R_{n,m}(\mathbf{x}) = \frac{1}{(n+m)!} P_n^m(\cos\theta)\, e^{im\phi} r^n, \tag{38}$$

$$S_{n,m}(\mathbf{x}) = (n-m)! P_n^m(\cos\theta)\, e^{im\phi} \frac{1}{r^{n+1}}, \tag{39}$$

where P_n^m is the associated Legendre function

$$P_n^m(x) = \left(1-x^2\right)^{m/2} \frac{\mathrm{d}^m}{\mathrm{d}x^m} P_n(x). \tag{40}$$

By a suitable choice of expansion points $\mathbf{y}_c$, and repeated application of the expansions, the direct relationship between the sampling points and nodes is avoided, and the calculation of the integrals by the matrix-vector products in (32) is reduced to an $O(N)$ operation. Further detail regarding the FMM is

presented in the book by Liu (2009).

Three different implementations of the FMM, described by Ying et al. (2004), Shen and Liu (2007), and Cruz et al. (2010) were investigated. Unfortunately due to some technical issues with the configuration of thrid party libraries I was not successful in applying parallel versions of these codes to the high performance hardware of the Oxford Supercomputing Centre (OSC), which limited the maximum size of simulations that could be performed. Within the project both a parallel $O(N^2)$ code and a serial $O(N)$ code were implemented. With the hardware available and the size of simulations performed, the $O(N^2)$ code was faster. For future larger scale work a fully parallel $O(N)$ code would be desirable.

3.2 Desingularized Integral Equation

As discussed above, the integrands in the boundary integral equations (24) and (22) are singular, and this can cause difficulty for the numerical integration. The use of simple Gaussian quadrature rules is inaccurate when the sampling points are near to the nodes.

There are two methods in the literature for treating the singular integrals. The first, as used by Grilli and Svendsen (1990) in two-dimensional work, is to use adaptive integration. This involves a repeated subdivision of the elements, adding more sampling points, until acceptable accuracy is reached. The second is to use a local coordinate transformation described in Eatock Taylor and Chau (1992):

$$x_i = \sum_{j=1}^{3} L_j(r_1, r_2)\, x_i^{(j)}, \tag{41}$$

$$L_1 = 1 - r_1,\; L_2 = r_1(1 - r_2),\; L_3 = r_1 r_2. \tag{42}$$

This maps a triangular region to a unit square in (r_1, r_2) coordinates. A standard

quadrature rule can be applied to the unit square, which provides an integration scheme which remains accurate even with a low-order singularity at the corner of the triangular region.

An alternative method, not previously applied to water wave problems, is to remove the singularity from the integral equation, potentially avoiding the need for any special integration method. By using the integral identity identified by Liu and Rudolphi (1999):

$$\int F(\mathbf{x},\mathbf{y})\,(\mathbf{y}_k-\mathbf{x}_k)\,\mathrm{d}S(\mathbf{y}) = \int G(\mathbf{x},\mathbf{y})\,\hat{n}_k(\mathbf{y})\,\mathrm{d}S(\mathbf{y}) \tag{43}$$

in the weakly singular integral equation (24), we can obtain the non-singular boundary integral equation found by

$$\int_S F(\mathbf{x},\mathbf{y})\left[\phi(\mathbf{y})-\phi(\mathbf{x})-\nabla\phi(\mathbf{x})\cdot(\mathbf{y}-\mathbf{x})\right]\mathrm{d}S(\mathbf{y}) = \int_S G(\mathbf{x},\mathbf{y})\left[\nabla\phi(\mathbf{y})-\nabla\phi(\mathbf{x})\right]\cdot\hat{n}(\mathbf{y})\,\mathrm{d}S(\mathbf{y}),\ \forall\mathbf{x}\in S. \tag{44}$$

For small r, we see that in the integral with the F kernel the term $[\phi(\mathbf{y})-\phi(\mathbf{x})-\nabla\phi(\mathbf{x})\cdot(\mathbf{y}-\mathbf{x})]$ is $O(r^2)$, and this cancels with the $1/r^2$ singularity. Likewise the term $[\nabla\phi(\mathbf{y})-\nabla\phi(\mathbf{x})]$ is $O(r)$, and cancels the $1/r$ singularity of the G kernel. Both of the integrals have been reduced to $O(1)$ for small r.

3.2.1 Discretization

By introducing integration sampling points, we can write the new non-singular equation (44) as a discrete sum:

$$\sum_m F(\mathbf{x},\mathbf{y}_m)\left(\phi_m-\phi(\mathbf{x})-\mathbf{v}(\mathbf{x})\cdot(\mathbf{y}_m-\mathbf{x})\right)w_m = \sum_m \left[G(\mathbf{x},\mathbf{y}_m)\left[q_m-\mathbf{v}(\mathbf{x})\cdot\hat{n}(\mathbf{y}_m)\right]\right]w_m,\ \forall\mathbf{x}\in S. \tag{45}$$

We first wish to establish whether this new integral equation will be prohibitively slow to solve. Each integration with a kernel has a large cost. By rewriting (45) as a series of separate summations:

$$\begin{aligned}\sum_m F(\mathbf{x},\mathbf{y}_m)\,\phi_m w_m + \mathbf{v}(\mathbf{x})\cdot\sum_m F(\mathbf{x},\mathbf{y}_m)\,\mathbf{y}_m w_m \\ + [\phi(\mathbf{x}) - \mathbf{v}(\mathbf{x})\cdot\mathbf{x}]\sum_m F(\mathbf{x},\mathbf{y}_m)\,w_m \\ = \sum_m G(\mathbf{x},\mathbf{y}_m)\,q_m w_m + \mathbf{v}(\mathbf{x})\cdot\sum_m G(\mathbf{x},\mathbf{y}_m)\,\hat{n}(\mathbf{y}_m)\,w_m, \quad (46)\end{aligned}$$

we can see that in comparison with (25) there are six new integrations required. These are the three components of $\sum F\mathbf{y}_m$, and the three components of $\sum G\hat{n}(\mathbf{y}_m)$. Crucially, these extra integrations only depend on the geometry, and not any part of the unknown vector. This means that within an iterative matrix equation solver these new calculations only need to be performed once, and the cost of each iteration is not greatly increased.

Compared to the weakly singular formulation (25), the non-singular form has the added complication of finding the velocity $\mathbf{v} = \nabla\phi$ at the nodes. This consists of two components, one normal to the surface and one tangential. The component of $\nabla\phi$ which is normal to the surface is available directly as the Neumann data, which is part of the known vector on the body surfaces, and part of the unknown vector on the free surface. The tangential part of $\nabla\phi$ is calculated by numerical differentiation, which is performed by using the shape functions of the triangular or quadrilateral elements.

3.2.2 Performance of the Nonsingular Integral Equation

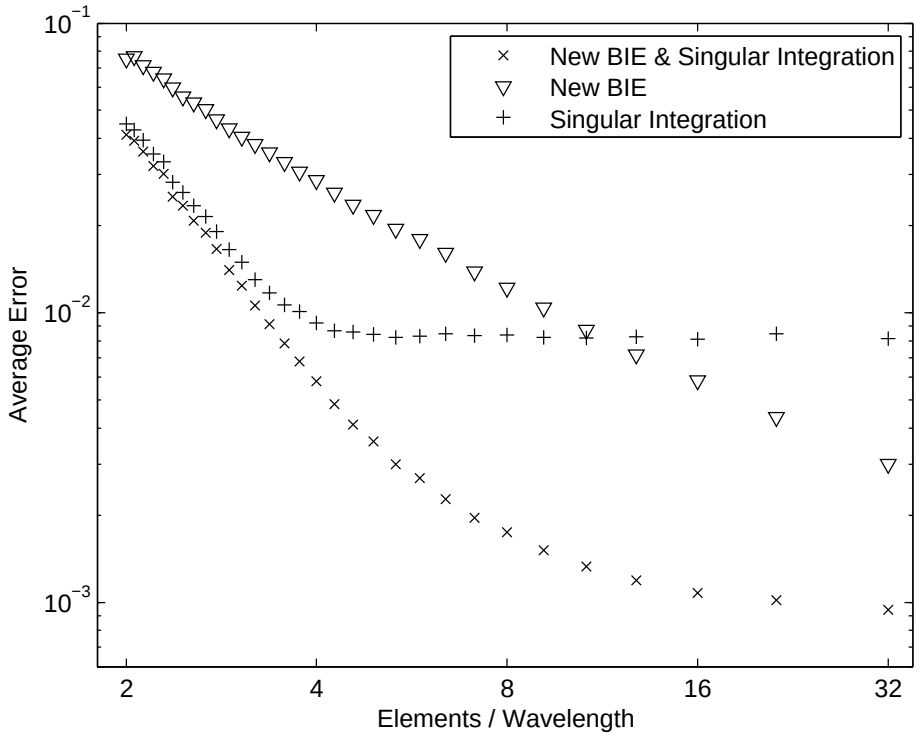

Figure 3: Laplace solver accuracy

In order to assess the benefit of the new integral equation in comparison to the coordinate transformation method (42), I set up a simple test case. The computational domain used is a rectangular cuboid. On the upper surface the Dirichlet condition potential is specified as the sinusoid $\phi = \sin(kx)$. On the other sides and lower surface the Neumann boundary condition is $v_n = 0$. The length of the cuboid is chosen to allow an integer number of wavelengths, avoiding any conflict between the boundary conditions at the edges. The depth is sufficiently large so that $\tanh(kh) \approx 1$. The width of the region should in theory have no effect on the solution, but was set at 25% of the length.

This test case corresponds to the physical situation of a linear standing wave as it passes horizontal, where the instantaneous free surface is flat. This choice of boundary condition allows the error to be evaluated for a situation similar to

those arising in fully non-linear simulations, and has a simple exact solution for the vertical velocity on the free surface.

Figure 3 shows the average error in the computed vertical velocity as a function of the resolution. This average is calculated by an integral over the free surface: $error = \frac{1}{A}\int |v_{\text{theory}} - v_{\text{computation}}|\,\mathrm{d}S_F$. It can be seen that applying a combination of both the new boundary integral equation (44) and the singular integration technique (42) provides superior accuracy. The result of not using either the desingularized integral equation or coordinate transformation is not displayed but is highly inaccurate.

At low resolution, the major source of error is due to the shape functions of the surface elements being unable to represent accurately either the boundary condition or the solution. This can be seen in the straight line power-law type relationship to the left of the figure.

At higher resolution, the approximation error decreases, and the integration error becomes increasingly important. The inaccuracy of the integration leads to high wavenumber noise in the solution. This can be seen most clearly in the case of using just the coordinate transformation, where there is no improvement in accuracy above four elements per wavelength. In the simulation of steep wave events there is a physical transfer of energy to the mesh-scale wavelengths, and it is important that this physical energy transfer is not dominated by numerical noise. The coordinate transformation method was found to introduce a lot of mesh-scale noise even at large numbers of elements per wavelength, while the new integral equation performed much better in this respect.

The performance of the new integral equation by itself at low resolution is slightly puzzling. In comparison to the coordinate transformation method it has a lower noise limit, but is less accurate for the low resolutions where the approximation error is large. One possible reason for this is the different number of sampling points used by the two methods. Each quadratic triangle contains

four sampling points, but the coordinate transformation method changes this to nine sampling points mapped into a triangle when there is a singularity.

The accuracy of the Laplace solver, particularly at very low resolutions, has important consequences for the stability of the numerical scheme. Due to the possibility of "saw-tooth" type instabilities, it is important both to limit the introduction of mesh-scale noise, and to avoid the magnification of mesh-scale oscillations that are already present.

3.3 Conclusion

This chapter has outlined the use of the boundary element method for solving the Laplace problem associated with water waves. Green's second identity leads to an integral equation over the boundary of the domain. This is then discretized to a linear system of equations, suitable for solving with standard direct or iterative methods. The application of the Fast Multipole Method reduces the computational complexity of the surface integrals from $O(N^2)$ to $O(N)$, while maintaining a form suitable for iterative solvers.

A new form of desingularized integral equation is presented, with the motivation of improving the accuracy of the near-singular integrals in a computationally efficient manner. This is shown to work well in conjunction with a coordinate transformation method. There is a an extra computational cost due to additional kernel integrations in setting up the system of equations, but very little additional work is required at each iteration of a solver.

4 Wave Damping and Generation

In this section we develop a method used to generate incident waves and damp outgoing waves. This method enables numerical simulations to be carried out in a small computational domain surrounding a body. There is no need to accurately model the mechanics of a paddle or to represent a large tank to avoid reflections. Instead, accurate results can be obtained with a domain with a radius even as small as a single wavelength.

4.1 Theory

4.1.1 Wave Damping

A straightforward method of wave damping is to add dissipative terms to the nonlinear free surface boundary conditions (9) and (10):

$$\frac{\mathrm{D}\phi}{\mathrm{D}t} = -g\eta + \frac{1}{2}\left|\nabla\phi\right|^2 - \omega_0\gamma\phi, \tag{47}$$

$$\frac{\mathrm{D}\eta}{\mathrm{D}t} = \nabla\phi - \omega_0\gamma\eta, \tag{48}$$

where ω_0 is a characteristic angular frequency, and $\gamma\left(x, y\right)$ is a damping strength function. This strength function varies from zero for no damping to order unity for full damping. It is possible to choose a different strength function for the two boundary conditions, but the performance is better when they are kept identical.

Unfortunately, as discussed in Clamond et al. (2005), the damped equation (47) does not perform very well. This is because the physical quantity that should be damped is the velocity, while equation (47) applies damping to the velocity potential. With this in mind, we instead use a different dissipative term:

$$\frac{\mathrm{D}\phi}{\mathrm{D}t} = -g\eta + \frac{1}{2}\left|\nabla\phi\right|^2 - \omega_0\nabla_H^{-1}\gamma\nabla_H\phi, \tag{49}$$

in which ∇_H and ∇_H^{-1} are the horizontal gradient and inverse horizontal gradient. The motivation is to transform from potential to velocity, then apply the damping, and then transform back to potential. An algorithm for the calculation of the required inverse gradient is given in section 8.1. The vertical component of the velocity is not directly controlled by either equation (48) or equation (49). The vertical velocity is instead calculated at each timestep as a result of the BEM calculation.

Equation (49) uses horizontal gradients, rather than the gradient tangent to the free surface, largely because the required derivatives and integrals are more straightforward to implement. The use of tangent derivatives might be considered to be more correct, in the sense that damped part of the velocity should be orthogonal to velocity calculated by the Laplace solver. In practice there is little difference between the two gradients except in extremely steep waves. In general, the damping velocity term $\gamma\nabla_H\phi$ will have a rotational component. This rotational component obviously cannot be represented by a potential, and is ignored by the inverse gradient.

The kinematic damping acts to add or remove fluid from the wave tank. This seems to be necessary for achieving good damping in a short space. In order for a numerical wavetank to behave as if it were unbounded, there must be a mechanism to remove volume which would otherwise have flowed out of tank, otherwise this extra volume could only be redistributed back into the tank. This can be seen in a case such as a soliton, where removal of volume is necessary to prevent reflection. It would be possible to maintain conservation of volume by only applying dynamic damping, however this requires a much larger damping region with a very gradual increase in strength. As described below, equations (48) and (49) only provide good performance if used together. If strict conservation of volume were required, analogous to a physical wavetank, it may be that a viscous type method such as described in Cho and Kim (2008) would be preferred.

The conservation of volume can also be used as a check on the accuracy of a simulation. This could still be applied even with the removal of volume by equation (48), so long as a record is kept of the volume removed by the kinematic damping.

4.1.2 Wave Generation

The damping method described above can be considered as a form of proportional control, towards the condition of zero velocity and zero elevation. We now address the issue of wave generation: If the damping method can remove waves, could it also introduce them?

The established methods for generation of waves in numerical work are either to simulate a piston or paddle type wavemaker, or to simply specify an initial condition and apply no extra forcing. Both methods have limitations, but can be used to produce a variety of sea states. For example Kim et al. (1998) combined the two methods, imposing a uniform current with an initial condition and creating regular waves with a piston wavemaker.Zhang et al. (2012)

A major issue with the existing methods which we seek to address is that they cannot combine wave generation with the damping of the outgoing waves. A wavemaking piston will perfectly reflect any outgoing waves which reach it back into the computational domain. Simulations such as Kim et al. (1998) are commonly performed in a square tank with a piston on one wall, and with this setup only the downstream wall can have damping applied to prevent reflection. No damping is applied to the piston wall or side walls, as this would interfere with the wave generation.

To apply combined wave generation and damping in our numerical scheme, we simply modify the damped free surface boundary conditions (48) and (49) to:

$$\frac{\mathrm{D}\phi}{\mathrm{D}t} = -g\eta + \frac{1}{2}\left|\nabla\phi\right|^2 - \omega_0 \nabla_H^{-1} \gamma \nabla_H \left(\phi - \phi_0\right), \tag{50}$$

$$\frac{\mathrm{D}\eta}{\mathrm{D}t} = \nabla\phi - \omega_0 \gamma \left(\eta - \eta_0\right), \tag{51}$$

where $\phi_0\left(x, y, t\right)$ and $\eta_0\left(x, y, t\right)$ are chosen to represent an incident wave. This might be anything from a small sinusoidal wave to a complex multi-directional sea-state. There are some limits with generating non-physical wave shapes, as the full non-linear equations are still being applied, just guided towards a desired profile and velocity.

Equations (50) and (51) will control the wave elevation and velocity towards that of a desired incident wave, just as damping controls the elevation and velocity towards zero. The degree of control is governed by the strength function $\gamma\left(x, y\right)$. Crucially, any waves which travel from a clear or uncontrolled region (where $\gamma = 0$) into a region where γ is nonzero should undergo no more reflection than with simple damping.

For the simulation of wave-structure interaction, we envisage a central clear region surrounded by an annular damping and generation region. This is illustrated and explained further below. The aim is to have the clear region, and any structure within it, to behave as if it were surrounded by a large ocean of water, despite being in a small computational domain.

4.1.3 Condition at Edge of Numerical Tank

When generating a wave in this manner, there may be an issue with compatibility at the edge of the tank. While the free surface is being encouraged to have a certain horizontal velocity, the side walls are stationary, and this causes a problem at the intersection line. One straightforward solution to this problem is to apply a velocity condition on the side wall, matching the incident wave. However, in

order to describe accurately the velocity profile with depth a high resolution mesh on the side walls is required. It would be preferable to use as few elements on the side wall as possible, perhaps just one or two for the entire depth of tank, but with a coarse sidewall mesh the incompatibility at the intersection line is inevitable.

A more efficient solution developed here involves applying a much stronger version of the wave damping. Instead of damping the time derivatives, an update equation is applied at the end of a timestep:

$$\eta_{new} = \eta - \beta \left(\eta - \eta_0 \right), \tag{52}$$

$$\phi_{new} = \phi - \beta g \Delta T \left(\eta - \eta_0 \right), \tag{53}$$

where β is another damping strength function, and ΔT is the timestep of the simulation. The motivation of using an update equation of this form is the ability to specify very strong control, without introducing problems related to the stiffness of the time derivatives.

As we are just using this method to remove a problem at the edge of the domain, the strength function β is simply equal to unity for nodes at the tank edge, and zero elsewhere. It is possible to have a wider region with a more gradual introduction, but we leave the damping to the time derivative terms.

In theory the update equation for the potential should be analogous to (50), with transformation to and from velocity. However, it was found to be more reliable to use the simpler method of (53).

4.1.4 Second Order Wave Generation

We now consider the choice of an incident wave which provides the potential $\phi_0(x, y, t)$ and the elevation $\eta_0(x, y, t)$ in equations (50) and (51). The generation mechanism guides the water towards the requested incident wave in the manner of proportional control, rather than enforcing it. A clearly non-physcial shape, such as a square wave for example, could not be produced even approximately.

More subtle is the behaviour when the requested incident wave does not quite satisfy the fully nonlinear boundary conditions by itself. This is the case when constructing a steep wave from sinusoidal components, as is typically done when creating a focussed wave group. If a steep sinusoid is requested as an incident wave, then the wave generation will provide proportional control towards this nonphyscial shape, while the nonlinear boundary conditions will cause deviation. The resulting wave which is created will be neither the pure sinusoid nor have the natural bound nonlinear structure, but will instead contain nonlinear error waves.

For certain cases, accurate nonlinear solutions exist which are suitable for use as an incident wave, for example the fifth order Stokes wave described by Fenton (1985). We would however like to be able to construct more general waves from frequency components, without encountering large nonlinear error waves.

For moderate steepness, we find it is important to correct the incident wave to 2nd order. Assuming that an incident wave is constructed from frequency components, we follow the procedure in Dalzell (1999), to find the sum and difference frequency contributions from each pair of components.

Each first order component has amplitude a_j, angular frequency ω_j, and heading angle θ in the horizontal plane. The vector of wavenumber components is κ_j, so that the scalar wavenumber in the x direction is $|\kappa_j| \cos\theta$ and in the y direction $|\kappa_j| \sin\theta$. Using the phase function $\psi_j = \kappa_j \cdot \mathbf{X} - \omega_j t$, each frequency component

has a contribution by itself:

$$\begin{aligned}\phi_j &= a_j \frac{g}{\omega_j} \frac{\cosh\left(|\kappa_j|\,(z+h)\right)}{\cosh\left(|\kappa_j|\,h\right)} \sin\psi_j \\ &+ \sum_j a_j^2 \frac{3\omega_j}{8} \frac{\cosh\left(2\,|\kappa_j|\,(z+h)\right)}{\sinh^4\left(|\kappa_j|\,h\right)} \sin\left(2\psi_j\right), \end{aligned} \tag{54}$$

$$\begin{aligned}\eta_j &= a_j \cos\psi_j \\ &+ \frac{a_j^2\,|\kappa_j|}{4\tanh\left(|\kappa_j|\,h\right)} \left[2 + \frac{3}{\sinh^2\left(|\kappa_j|\,h\right)}\right] \cos\left(2\psi_j\right) \\ &- \frac{a_j^2\,|\kappa_j|}{2\sinh\left(2\,|\kappa_j|\,h\right)}. \end{aligned} \tag{55}$$

For every pair of frequency components ω_1 and ω_2 we add the terms:

$$\begin{aligned}\phi &= a_1 a_2 A_p\left(\kappa_1,\,\kappa_2\right) \frac{\cosh\left(|\kappa_1+\kappa_2|\,(z+h)\right)}{\cosh\left(|\kappa_1+\kappa_2|\,h\right)} \sin\left(\psi_1+\psi_2\right) \\ &+ a_1 a_2 A_m\left(\kappa_1,\,\kappa_2\right) \frac{\cosh\left(|\kappa_1-\kappa_2|\,(z+h)\right)}{\cosh\left(|\kappa_1-\kappa_2|\,h\right)} \sin\left(\psi_1-\psi_2\right), \end{aligned} \tag{56}$$

$$\begin{aligned}\eta &= a_1 a_2 B_p\left(\kappa_1,\,\kappa_2\right) \cos\left(\psi_1+\psi_2\right) \\ &+ a_1 a_2 B_m\left(\kappa_1,\,\kappa_2\right) \cos\left(\psi_1-\psi_2\right), \end{aligned} \tag{57}$$

where the wave-wave interaction coefficients are:

$$\begin{aligned}A_p\left(\kappa_1,\,\kappa_2\right) &= -\frac{\omega_1\omega_2\left(\omega_1+\omega_2\right)}{D_p\left(\kappa_1,\,\kappa_2\right)} \left[1 - \frac{\cos\left(\theta_1-\theta_2\right)}{\tanh\left(|\kappa_1|\,h\right)\tanh\left(|\kappa_2 h|\right)}\right] \\ &+ \frac{1}{2D_p\left(k_1,\,k_2\right)} \left[\frac{\omega_1^3}{\sinh^2\left(|\kappa_1|\,h\right)} + \frac{\omega_2^3}{\sinh^2\left(|\kappa_2|\,h\right)}\right], \end{aligned} \tag{58}$$

$$
\begin{aligned}
A_m\left(\kappa_1,\,\kappa_2\right) &= \frac{\omega_1\omega_2\left(\omega_1-\omega_2\right)}{D_m\left(\kappa_1,\,\kappa_2\right)}\left[1+\frac{\cos\left(\theta_1-\theta_2\right)}{\tanh\left(\left|\kappa_1\right|h\right)\tanh\left(\left|\kappa_2 h\right|\right)}\right] \\
&+ \frac{1}{2D_m\left(\kappa_1,\,\kappa_2\right)}\left[\frac{\omega_1^3}{\sinh^2\left(\left|\kappa_1\right|h\right)}-\frac{\omega_2^3}{\sinh^2\left(\left|\kappa_2\right|h\right)}\right], \qquad (59)
\end{aligned}
$$

$$
\begin{aligned}
B_p\left(\kappa_1,\,\kappa_2\right) &= \frac{\left(\omega_1^2+\omega_2^2\right)}{2g}-\frac{\omega_1\omega_2}{2gD_p\left(\kappa_1,\,\kappa_2\right)}\left[1-\frac{\cos\left(\theta_1-\theta_2\right)}{\tanh\left(\left|\kappa_1\right|h\right)\tanh\left(\left|\kappa_2 h\right|\right)}\right] \\
&\times \left[\left(\omega_1^2+\omega_2^2\right)+g\left|\kappa_1+\kappa_2\right|\tanh\left(\left|\kappa_1+\kappa_2\right|h\right)\right] \\
&+ \frac{\left(\omega_1+\omega_2\right)}{2gD_p\left(\kappa_1,\,\kappa_2\right)}\left[\frac{\omega_1^3}{\sinh^2\left(\left|\kappa_1\right|h\right)}+\frac{\omega_2^3}{\sinh^2\left(\left|\kappa_2\right|h\right)}\right], \qquad (60)
\end{aligned}
$$

$$
\begin{aligned}
B_m\left(\kappa_1,\,\kappa_2\right) &= \frac{\left(\omega_1^2+\omega_2^2\right)}{2g}+\frac{\omega_1\omega_2}{2gD_m\left(\kappa_1,\,\kappa_2\right)}\left[1+\frac{\cos\left(\theta_1-\theta_2\right)}{\tanh\left(\left|\kappa_1\right|h\right)\tanh\left(\left|\kappa_2 h\right|\right)}\right] \\
&\times \left[\left(\omega_1^2-\omega_2^2\right)+g\left|\kappa_1-\kappa_2\right|\tanh\left(\left|\kappa_1-\kappa_2\right|h\right)\right] \\
&+ \frac{\left(\omega_1-\omega_2\right)}{2gD_m\left(\kappa_1,\,\kappa_2\right)}\left[\frac{\omega_1^3}{\sinh^2\left(\left|\kappa_1\right|h\right)}-\frac{\omega_2^3}{\sinh^2\left(\left|\kappa_2\right|h\right)}\right], \qquad (61)
\end{aligned}
$$

where

$$
D_p\left(\kappa_1,\,\kappa_2\right)=\left(\omega_1+\omega_2\right)^2-g\left|\kappa_1+\kappa_2\right|\tanh\left(\left|\kappa_1+\kappa_2\right|h\right), \qquad (62)
$$

$$
D_m\left(\kappa_1,\,\kappa_2\right)=\left(\omega_1-\omega_2\right)^2-g\left|\kappa_1-\kappa_2\right|\tanh\left(\left|\kappa_1-\kappa_2\right|h\right). \qquad (63)
$$

4.1.5 Breaking Suppression

With a surface-tracking scheme, breaking of short waves is a problem that can cause a premature end to the simulation. While smoothing is in general to be avoided to improve accuracy, it can be essential to prevent high wavenumber components from becoming too large. Here we have developed a method to prevent the formation of overturning waves by applying smoothing based on the curvature. Firstly a smoothed surface elevation $\tilde{\eta}$ is calculated, and then an update equation similar to equations (52) and (53) is applied at the end of a

timestep:

$$\eta_{new} = \eta - \omega_0 \Delta T \left(r_c \nabla_H^2 \eta\right)^2 (\eta - \tilde{\eta}), \tag{64}$$

$$\phi_{new} = \phi - \omega_0 g (\Delta T)^2 \left(r_c \nabla_H^2 \eta\right)^2 (\eta - \tilde{\eta}), \tag{65}$$

where r_c is a chosen cut-off radius of curvature.

The motivation behind this approach is that the smoothed elevation $\tilde{\eta}$ removes the overturning high wavenumber components, and may allow the simulation to continue where otherwise it would fail. The scaling with curvature is very rapid, ensuring that the main structure of the flow is affected as little as possible. Even the high wavenumber components are damped only when necessary, and are not much changed if the overall curvature is low. This does directly correspond to any physical smoothing mechanism, and should be considered as a purely numerical method for selectively removing the energy of the short waves.

While we found that this method did allow the simulaion of slightly larger amplitudes, it was not used for the results in sections 5 and 6, as the introduction of numerical smoothing can obscure the details of the physical behaviour. For very high steepness and overturning flow the robust treatment of a surface-capturing scheme would be required.

4.2 Wave Damping

In this section we investigate the performance of the new damping method outlined in section 4.1.1. We demonstrate the ability to absorb a wave with a relatively small damping region, and prevent reflection from the edge of a computational domain. This is a very useful feature for a numerical wave tank, as it allows a small domain to be used, providing a significant saving in computational effort.

4.2.1 Transmission Test

In order to assess the performance of the damping region, we first use a test case in which we can isolate the transmission and reflection properties. A small regular wave is generated at one end of a long tank, passes through a damping region in the centre of the tank, then finally meets a second damping region at the far end. The damping strength function γ for the central damper is a triangle function, with base one wavelength and height $2\gamma_0$. The terminal damping region is longer and more gentle, and is intended to absorb the waves completely, although it is not completely successful in this regard and does cause some reflection. This layout is illustrated in figure 4

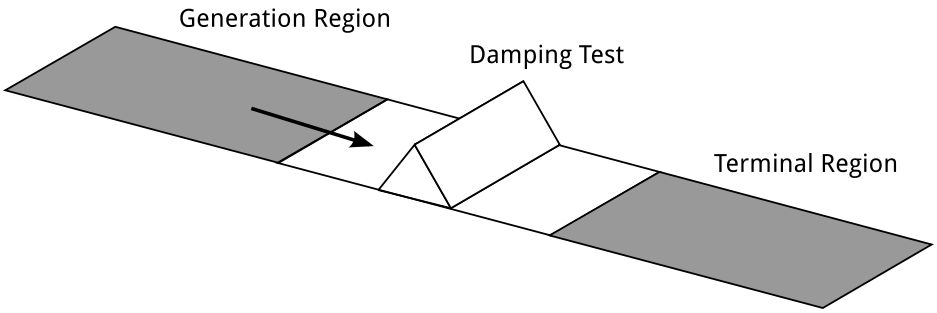

Figure 4: Damping test layout

For this investigation a 2D version of the solver was used, as this enabled a much wider range of coefficients to be simulated. Each simulation was allowed to run for sufficiently long to reach a steady state. The generated wave was allowed sufficient time to propagate through the test region, partially reflect off the terminal damping region, and return to the test region.

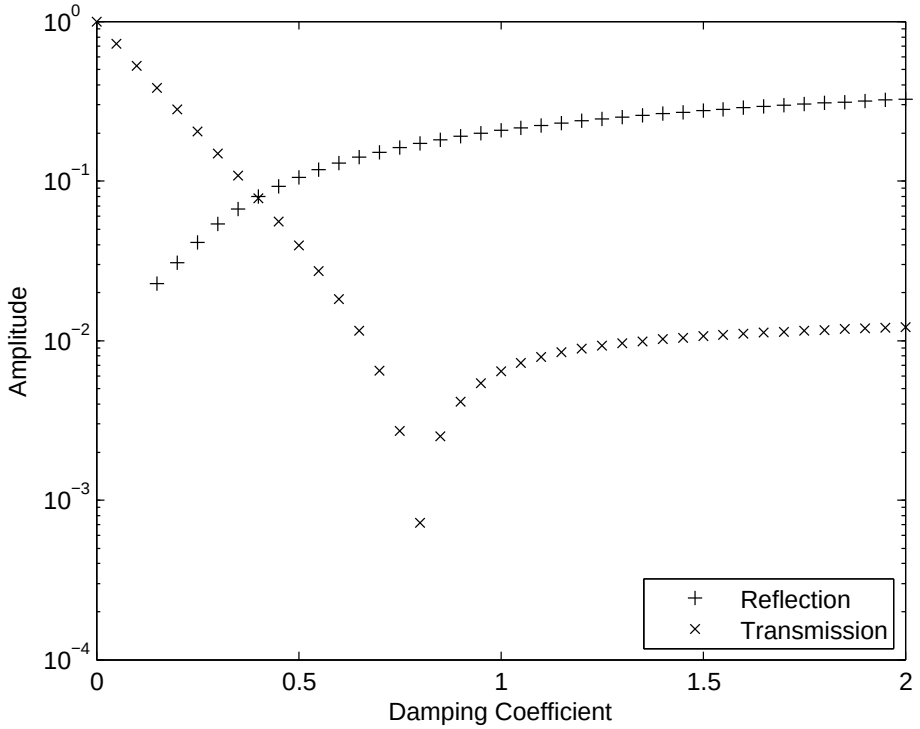

Figure 5: Kinematic damping only (eq. (48)), length 1 wavelength

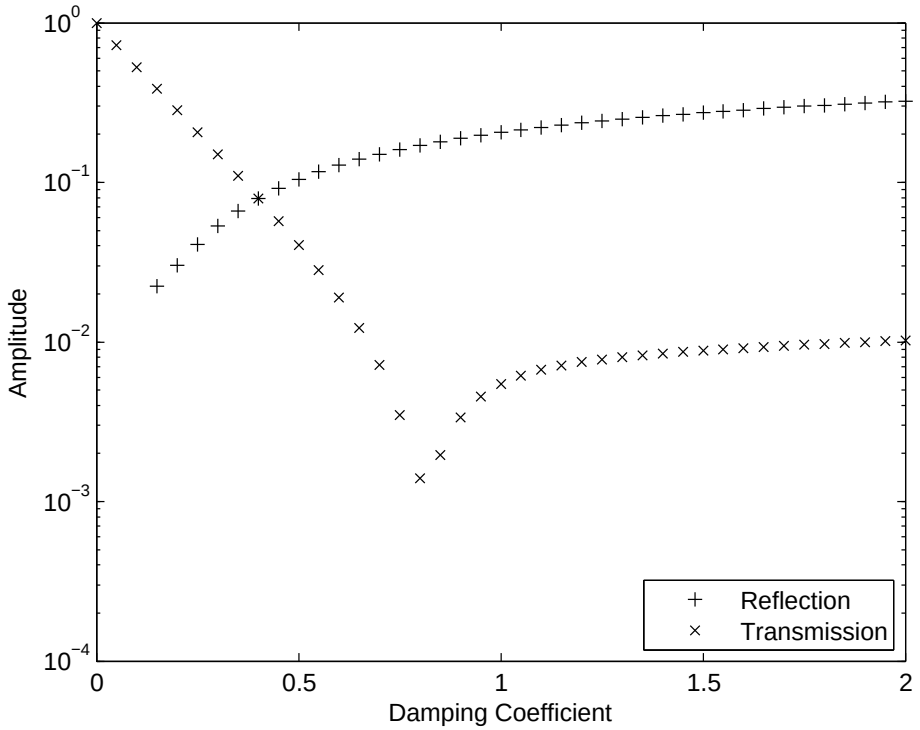

Figure 6: Dynamic damping only, (eq. (49)), length 1 wavelength

Figures 5 and 6 show the performance of a short damping region, when damping is applied to only one of the two boundary conditions, either the kinematic condition (48) or the dynamic condition (49). For a damping coefficient γ_0 of zero, the wave passes through the test region unaltered, with transmission coefficient of unity. As the strength of the damping region increases, the size of the transmitted wave decreases, but the size of the reflected wave also increases. The size of the reflected wave for small damping coefficient is not plotted, as it was polluted by waves which pass through the test region, reflect from the "terminal" region, and pass through the test region again in the opposite direction.

The amplitude of the reflected wave was measured over a length two wavelengths long, one wavelength upstream of the damping region. By combining the Fourier transforms of the elevation and the velocity data it is possible to distinguish between the incident wave travelling downstream and the reflection travelling back upstream. The amplitude of the reflected wave was taken as the sum of each upstream travelling frequency component, although there was negligible leakage to different frequencies. This amplitude was then further time-averaged over two wave periods. Conversely the amplitude of the transmitted wave was measured over a patch downstream of the damping region, and is the sum of frequency components travelling downstream, having already passed through the damping region.

The amplitude of the transmitted wave has a minimum around $\gamma_0 = 0.8$. This may correspond to a form of "critical" damping. By analogy with damped simple harmonic motion, small coefficients lead to underdamping, and large coefficients to overdamping. At $\gamma_0 = 0.8$ the wave is damped without overshooting the desired elevation. In a full wave tank it may not be possible to make full use of this critical damping effect, as a range of different frequency waves would be present.

It can be seen from figures 5 and 6 that applying damping to just one boundary

condition is not very effective. With a damping region of one wavelength, the best performance involves a reflected wave and a transmitted wave each of around 10% of the original amplitude. For acceptable performance the damping region would need to be more gentle, with a lower γ_0, and applied over a region of many wavelengths.

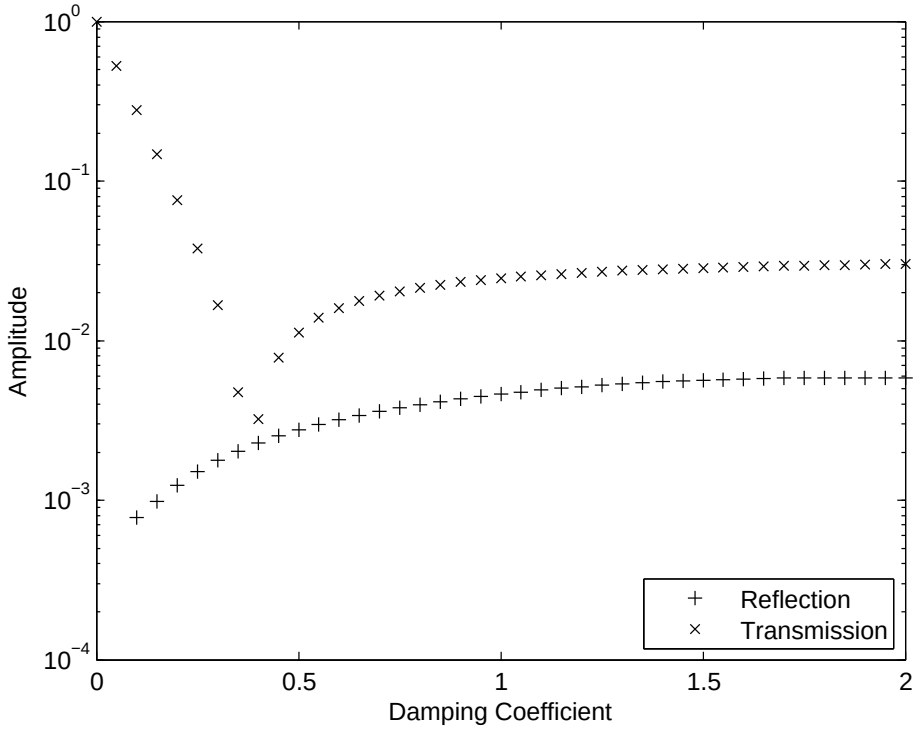

Figure 7: Combined damping, length 1 wavelength

Figure 7 shows the effect of applying equal damping to both the boundary conditions. The amplitude of the reflected wave is greatly reduced. The size of the transmitted wave increases slightly compared to the single boundary condition damping. This is partly a side effect of less wave energy being reflected. The minimum in the transmission curve moves from 0.8 to 0.4, which is consistent with effectively applying twice as much damping for the same value of γ_0.

Overall, the damping region applied to both boundary conditions demonstrates excellent performance. In a region which is only a single wavelength long, the wave damping can reduce both the transmitted and reflected waves to around

0.3% of the incident wave.

4.2.2 Reflection Test

In a practical scenario, the damping region will likely be used at the edge of a numerical tank, backed up by a solid wall. The test case in the previous section was useful as it allowed the reflection and transmission to be looked at separately. With a damping region placed next to a wall, the aim is to prevent the incident wave from reflecting from the wall, while avoiding early reflection from the damping region itself.

The layout of this test case with a wall is illustrated in figure 8. The damping function γ is a ramp, of length L with height γ_0/L. This resembles the first half of the triangle function used in the transmission test. Both kinematic and dynamic boundary conditions were damped equally.

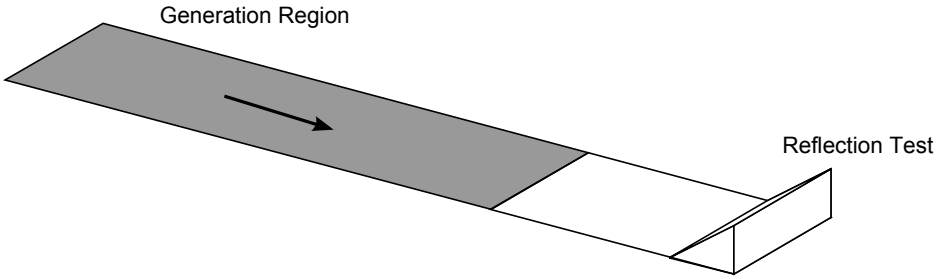

Figure 8: Reflection test layout

We investigated the effect of varying both the length and the strength of the damping region, as shown in figure 9.

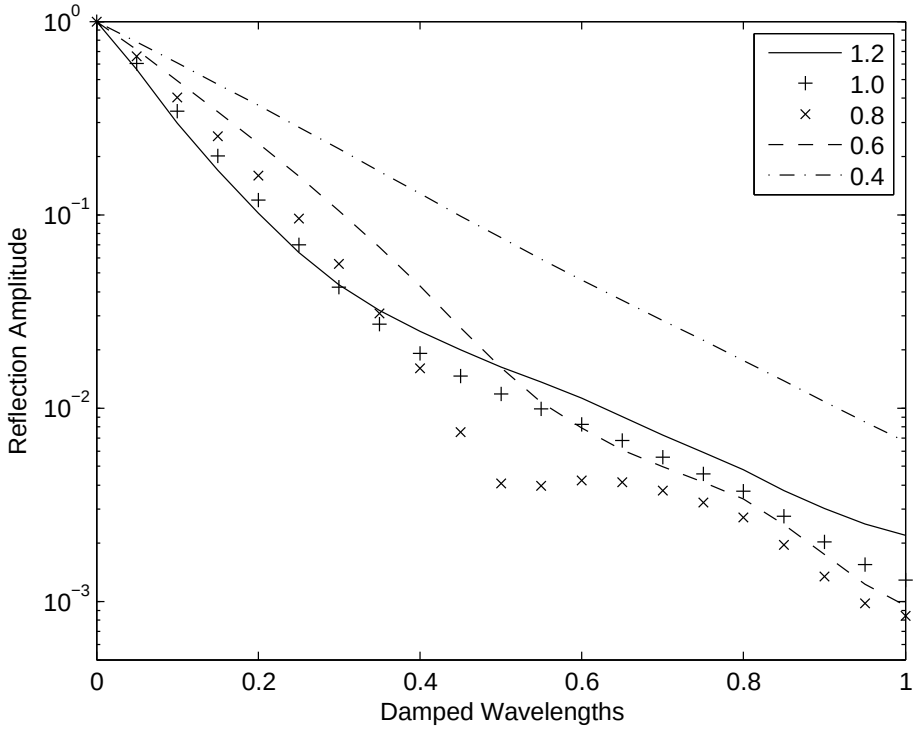

Figure 9: Combined damping at a wall, for different values of the damping coefficient γ_0

For a damping region of zero length, the entire incident wave is perfectly reflected by the wall. As the length of damping region increases, more of the wave can be absorbed without reflection.

The coefficient $\gamma_0 = 0.8$ works well across the full range of lengths, which is consistent with the low transmission identified in the previous section. The underdamped coefficients 0.6 & 0.4 do not have the strength for the very short length, but as they involve more gradual damping, might be expected to cause a lower amount of early reflection from the front of the damping region, and would perform well if applied over a much longer region if very high absorption were required. The overdamped coefficients are superior for the extremely short damping regions.

With a suitable choice of damping strength, the method presented here is capable of practically eliminating large reflections from a wall in very little space.

A damping region of half a wavelength can reduce the reflection to around 0.3%. Allowing a full wavelength reduces the reflection to less than 0.1%. Even a very short damping region of just 0.2 wavelengths can provide a reduction in the size of the reflected wave to 10%.

4.2.3 Choice of Damping Strength Function Shape

The strength functions used in the previous tests were the simple ramp and triangle. Alternative functions have been tested, including a quadratic and a raised cosine, but were found to be inferior. The discontinuity in slope at the start of the ramp function does not appear to cause any problems. Instead, it seems that reflection from the damping region depends on the maximum gradient with which the damping is introduced. Functions which have a smooth introduction necessarily have a steeper slope subsequently for the same total strength, and so cause more reflection.

We have only presented results for single frequency waves of small amplitude in this section. Section 4.3 deals with the combined generation and damping of steep wave groups which contain a range of frequencies . The damping strength γ is scaled by a characteristic frequency ω_0. This should be chosen to represent the longest waves in the simulation with significant amplitude. The higher frequency waves do not travel as quickly, so there is more time for the damping region to control them. A damping strength function for higher frequency waves would be relatively steeper, so the higher frequency components will not suffer from early reflection from the damping region. The long, low frequency waves require the most space to damp, and scaling for a low frequency will ensure that the higher frequencies are adequately damped.

4.3 Wave Generation

In this section we investigate the ability of the wave generation method to produce steep NewWave groups. Unlike section 4.2, we treat the full 3D problem in a circular tank. An example computational mesh is shown in figure 10.

The size of the numerical wave tank used is scaled according to the wavelength λ_0 of the peak frequency. All the results in this section are performed in a tank of radius $2\lambda_0$. At the centre of the tank, where a body could be located, there is a "clear region" in which no damping or wave generation is performed. Waves in this region satisfy the natural nonlinear boundary conditions. This region is chosen to have a radius of $0.5\lambda_0$, although this may be varied. A large clear region would require a larger tank, while a smaller clear region may compromise the physical behaviour of the waves, especially in the presence of a solid body.

The generation and damping region begins at a radius of $0.5\lambda_0$ and extends outwards to the edge of the tank, for a total length of $1.5\lambda_0$. The strength function used is a ramp increasing with radius, and coefficient 0.8, scaled with the angular frequency of the spectral peak ω_0. At a radius of $1.0\lambda_0$ the mesh elements begin to decrease in resolution, saving computational effort. This mesh stretching can be clearly seen in figure 10. While the clear region and the innermost part of the generation region are at a high resolution, the outer part of the wave tank is only required for the generation of the long wave components, and these can be represented on a coarse mesh. The outer wall is modelled by just a single element for the entire depth, as all the wave generation and damping is performed in the interior.

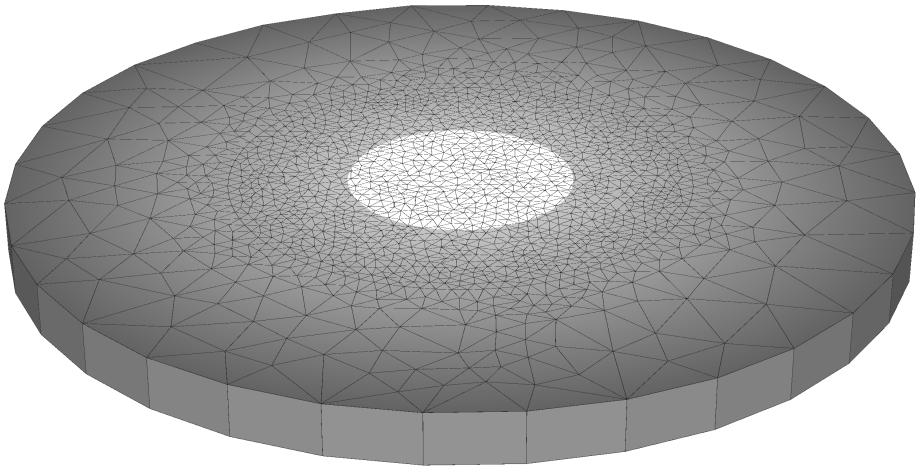

Figure 10: Computational mesh, showing annular wave generation region and central clear region

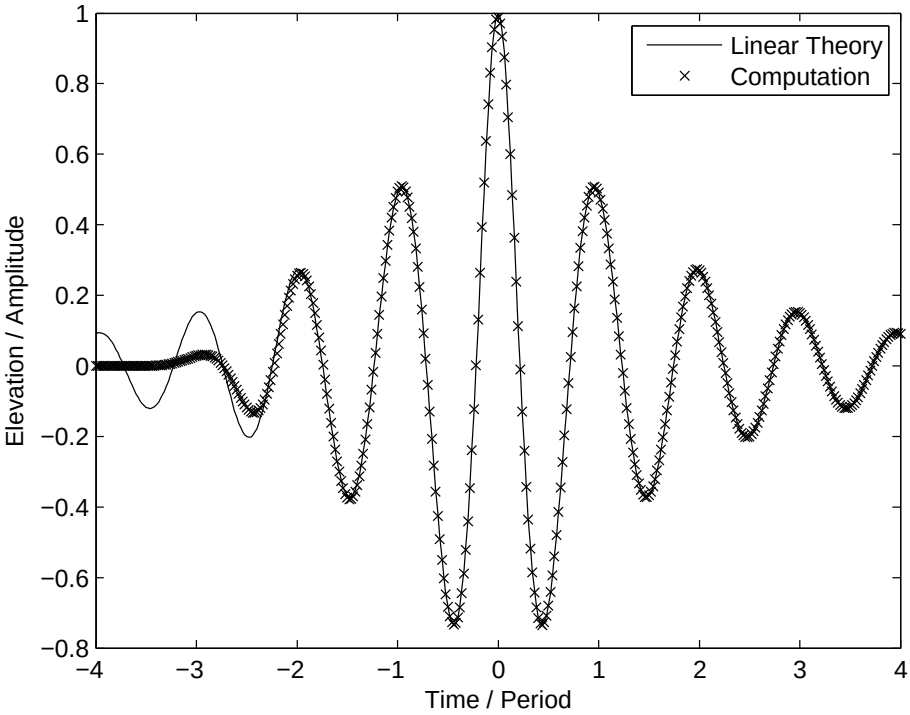

Figure 11: Generation of a small amplitude wave group

Figures 11 and 12 show the generation of a small unidirectional NewWave group, with focus at the centre of a circular tank. A Jonswap spectrum was used, with a peak frequency of 0.61 Hz and peak enhancement coefficient $\gamma = 3.3$, with water depth of 0.505m. Although the wave is unidirectional, the generation region has circular symmetry, with no preferred direction. It is not restricted to creating waves in one direction only. This is discussed further below.

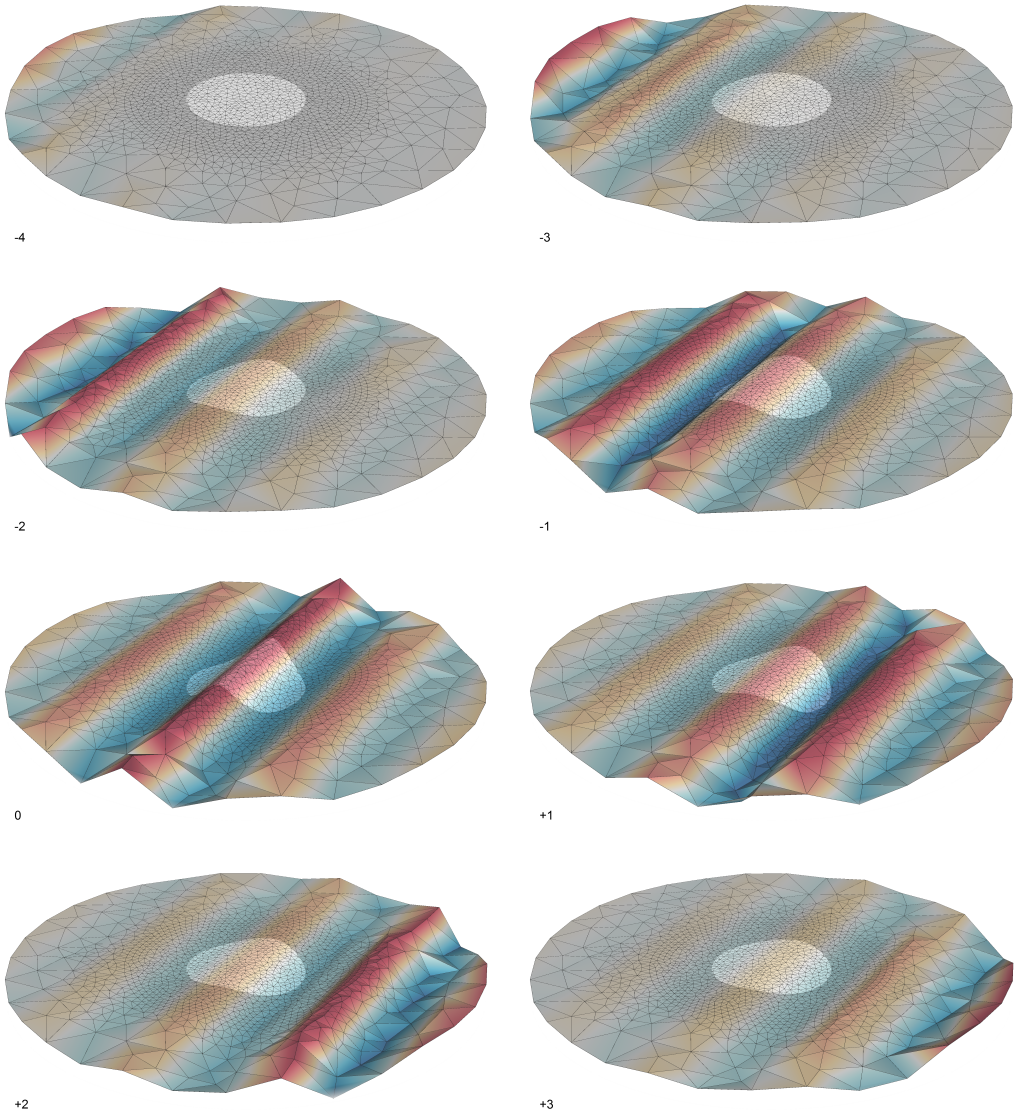

Figure 12: Generation of a small amplitude wave

The initial condition is chosen as the incident wave elevation and potential 4 periods before focus, multiplied by the square of the damping strength func-

tion. This creates a flat spot in the clear region, which would be suitable for placing a solid body. Alternatively the entire simulation could start from rest, but this would cause a longer lag time before the elevation at the centre of the tank begins to match the desired profile. The unsquared damping strength function is not used to construct the initial condition because it has a discontinuous slope, and this causes the creation of very high wavenumber components. The squared damping strength function is a sufficiently smooth ramp function that these unwanted waves are avoided.

After the starting periods, in which the wave must travel across the clear region, the wave generation procedure can be seen in figure 11 to produce the requested wave group almost exactly. The annular generation region is able to create accurately small unidirectional waves that travel into the clear region. On the far side of the clear region, the generation region again damps the free surface towards the requested incident wave, and prevents any reflection from the tank wall.

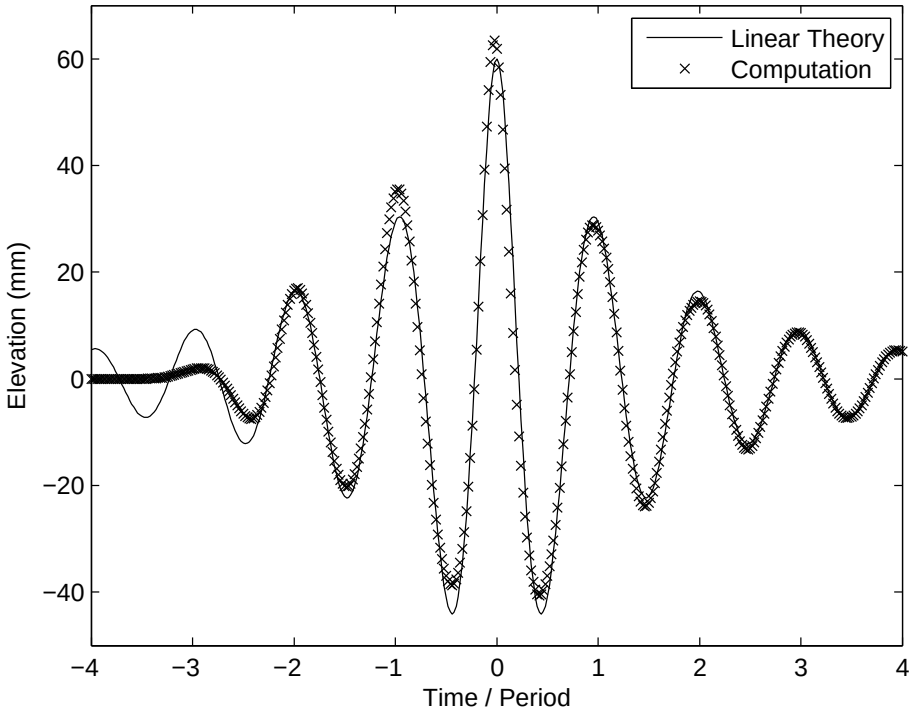

Figure 13: Generation of a nonlinear wave group ($kA = 0.1$), including second order error waves

Figure 13 shows the generation of a wave group with steepness $kA = 0.1$. Unlike the small wave shown in figure 11, there is deviation from the requested incident wave, at $t = 0$ and elsewhere. There are two reasons for this, both associated with nonlinearity. First, the wave should undergo nonlinear steepening as it passes across the clear region, as a natural consequence of the physical behaviour. This steepening will occur to a limited extent even within the generation region. Second, the requested incident wave does not satisfy the nonlinear boundary conditions by itself, as it is created assuming linear theory but is moderately steep. This causes the creation of what are known as error waves.

In order to check that the generated wave does not have a strong dependence on the grid, we repeat the simulation using a coarser mesh as shown in figure 14. Based on linear dispersion the incident wave has a central wavelength of 3.312 m. The fine mesh has a scale of 0.225 m, and the coarse mesh a scale of 0.376 m.

These scales are imposed as an area constraint in the mesh generation, so that no triangular element has an area larger than $0.5 \times scale^2$.

It can be seen in figure 14 that there is only a very slight deviation caused by the mesh scale. This is most noticeable at the central peak, and is consistent with the coarse mesh not being able to fully represent the highest wavenumber components, particularly the second order sum components. To demonstrate full convergence would require a computationally expensive very fine mesh.

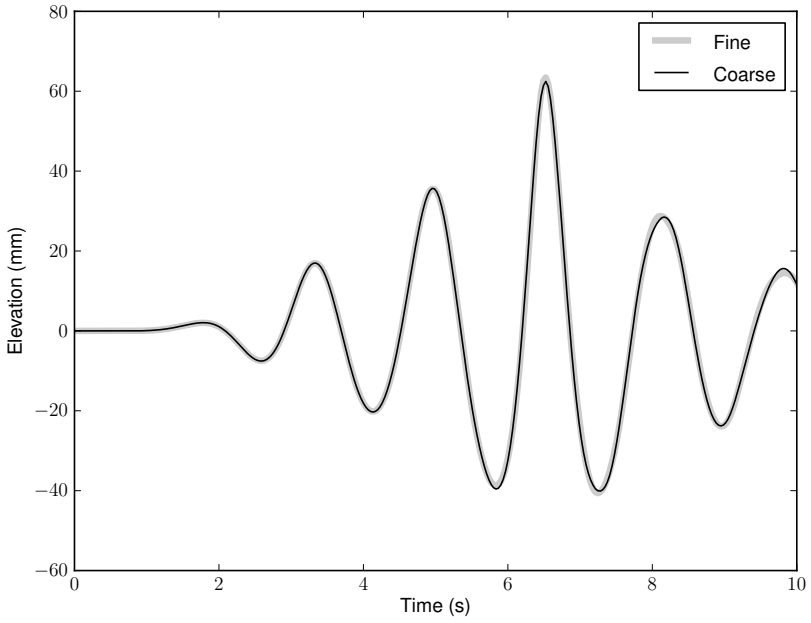

Figure 14: Convergence of wave generation

The result of figure 13 will be highly dependent on the size of the clear region. With only 0.5 wavelengths, the wave is steep within the generation region, and does not have time to fully develop. The clear region could be increased in size, until the waves are sufficiently linear in the generation region. However, while the wave group is a focussed event, it still involves steep waves for many wavelengths and periods before and after focus, and increasing the size of the clear region is very computationally expensive.

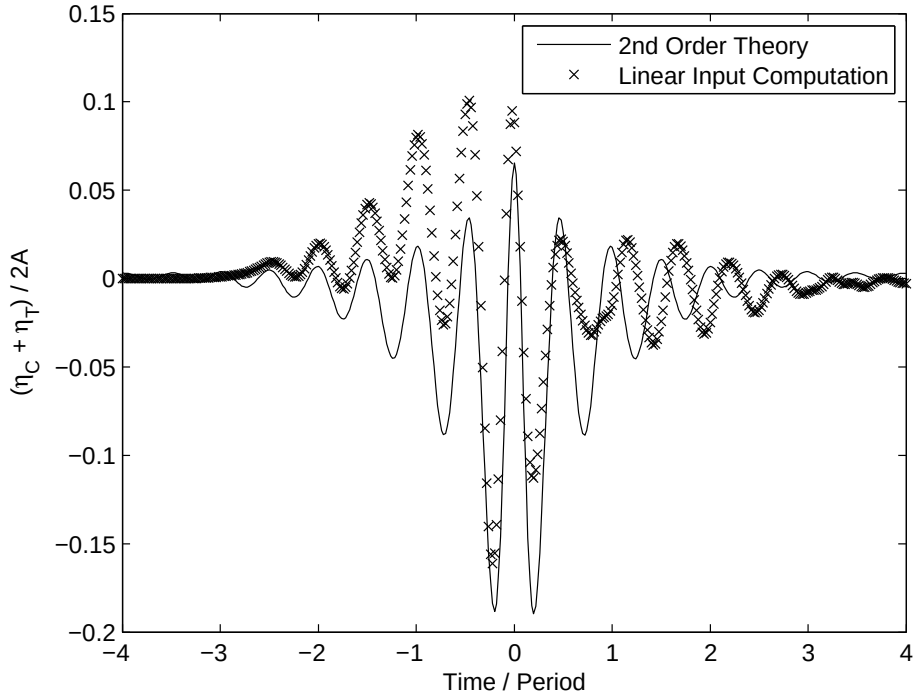

Figure 15: Second order behaviour of wave generation, including error waves.

The nonlinear behaviour that occurs for a steep wave with a linear input profile can be seen in figure 15. This graph plots the sum of a crest-focussed and a trough focussed wave, which eliminates the linear term and higher order odd harmonics. Compared to the elevation predicted by second order theory, the computation shows the existence of large error waves. Before the focus time the second order sum term behaves roughly correctly, reproducing the double frequency component. However, the quickly propagating error wave associated with the second order difference term causes a large set-up. After the focus time, the slowly propagating error wave associated with the second order sum is large, and has opposite phase to the expected nonlinear behaviour.

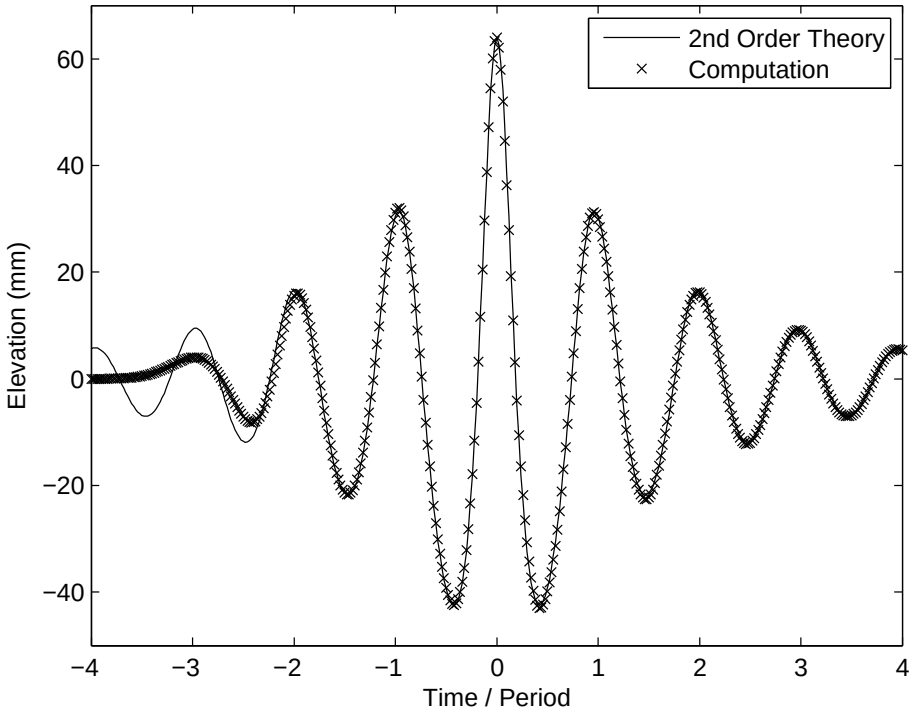

Figure 16: Generation of a nonlinear wave group ($kA = 0.1$), after applying correction to second order.

The error waves present in figures 13 and 15 are the result of requesting the generation of a non-physical linear profile. The situation can be improved by correcting the input wave to second order, by the method presented in Dalzell (1999) and described in section 4.1.4. The results of this correction are shown in figure 16. With the second order error waves removed, the wave generation procedure is once again able to create accurately the desired wave group.

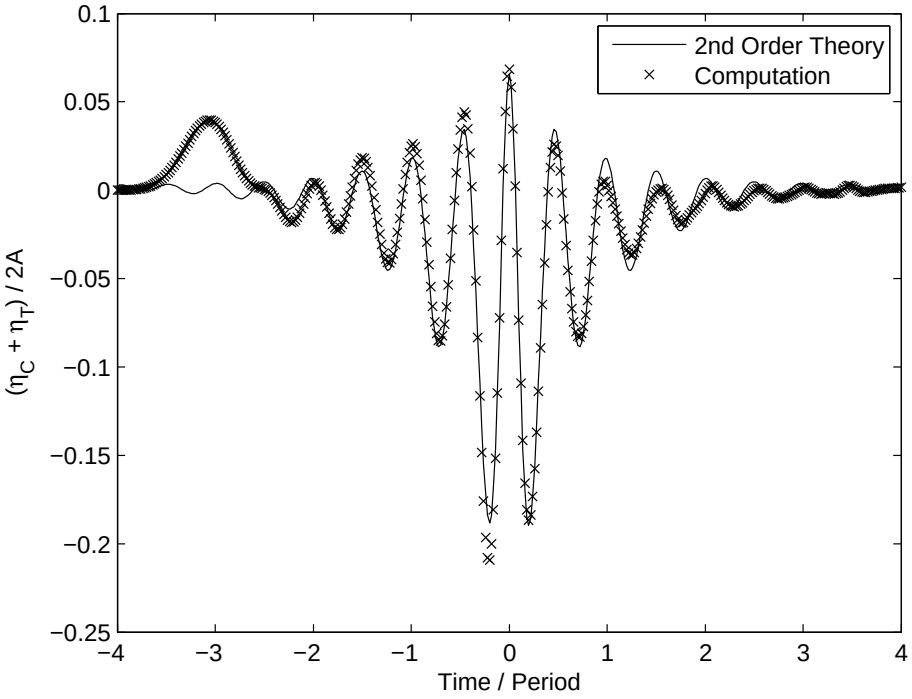

Figure 17: Second order behaviour

Figure 17 shows the second order behaviour obtained by eliminating the linear term. The computation reproduces the theoretical profile reasonably well, but is not perfect. By comparison with figure 15, it appears that some of the error wave might remain. This is indicated as there is the same set-up before focus and reduction in amplitude after focus. The deviation three periods before focus is associated with a starting transient. The wave generation method does not conserve volume, and some of the extra mass which is introduced propagates as a long wave.

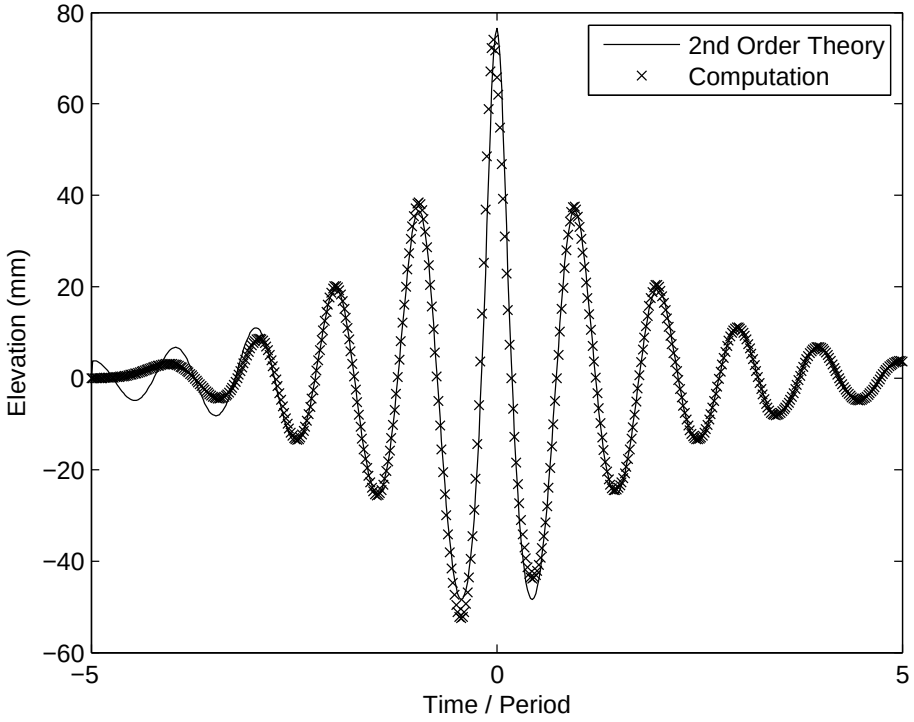

Figure 18: Generation of a steeper wave, $kA = 0.2$

Figure 18 demonstrates the importance of the higher order nonlinear effects at higher steepness. For this case the central frequency is 0.82 Hz, and $kA = 0.2$. One of the 3rd order effects is to change the phase speed, and the focal point is moved slightly in the direction of travel. This effect of this is particularly evident in the troughs adjacent to the central peak. The peak is slightly lower and arrives earlier than predicted by the 2nd order theory.

These higher order non-linear effects evident in figure 18 are largely a consequence of the real physical behaviour, rather than error waves. An upper bound for the increase in phase speed can be obtained by considering the narrow banded limit of a single frequency. From the third order dispersion relation for a stokes wave (Whitman, 1974):

$$\omega^2 = (gk \tanh kh) \left\{ 1 + \frac{9 - 10 \tanh^2 kh + 9 \tanh^4 kh}{8 \tanh^4 kh} (kA)^2 \right\} + O\left((kA)^4\right), \quad (66)$$

by inserting the relevant parameters we find in this case that the maximum possible increase in phase speed is $c_{nonlinear} = 1.025 \times c_{linear}$.

The size of the clear region will have an effect on the location of the focal point. In the case studied the clear region covers a distance of 0.5 wavelengths, in which the wave travels faster than linear theory. A larger clear region would result in a larger change in the focal position. However, this is not an obstacle that prevents the use of the generation mechanism presented here, as the shift in focus location can be compensated for. If a precise focal location were required, such as at the bow of an FPSO, then a trial run can be performed first without the vessel, and then the vessel placed where the maximum elevation occurs.

5 Validation

5.1 Surge Force on a Cylinder

To further validate the wave generation, we demonstrate the ability to reconstruct waves produced in an experimental tank, and compare the surge forces acting on a bottom mounted cylinder. For this geometry we can perform a comparison with experiments performed in the shallow water basin at DHI, reported in Zang et al. (2010).

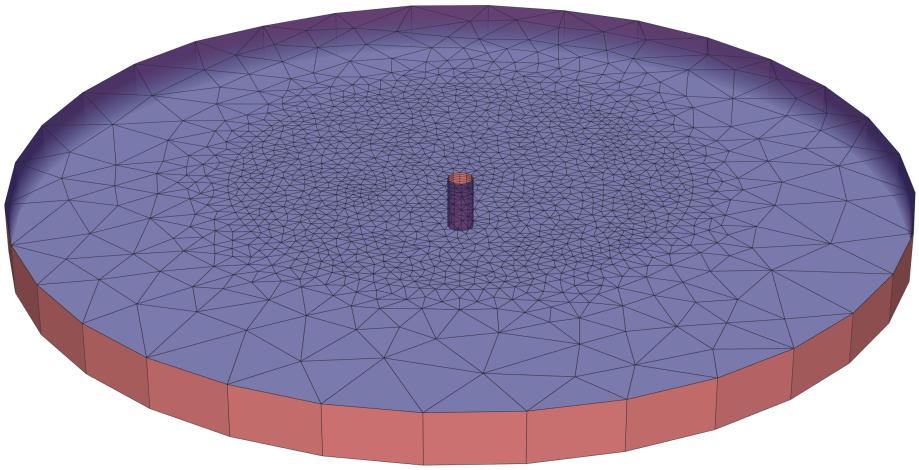

Figure 19: Cylinder mesh

A wave group was created with peak frequency of 0.820 Hz, in water of depth 0.505 m. The elevation of the incident wave was recorded, and then a bottom mounted cylinder of diameter 0.25m was placed in the tank, with the leading edge at the focal point. The computational mesh for our simulations is shown in figure 19. The mesh is consistent with those used for the investigation of wave generation in section 4.3 and the convergence study described in section 6.3.

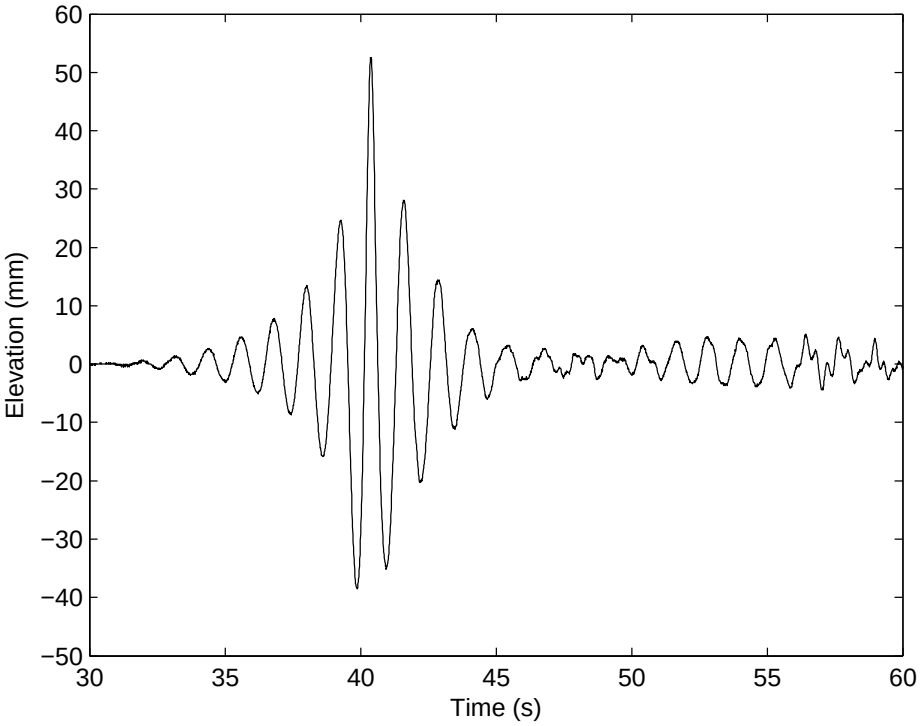

Figure 20: Experimental wave elevation

Figure 20 shows the elevation of the wave group produced with a paddle, in the absence of the body for the experimental results. A side effect of the paddle dynamics is the creation of slowly moving double frequency error waves, which can be seen at around 48 seconds. Compared to the computational simulations presented below, the experimental wave is created much further from the focus, and this causes the slow error waves to arrive well after the focussed group. Later, around 54 seconds, we can see the effect of partial reflection from the beach at the end of tank.

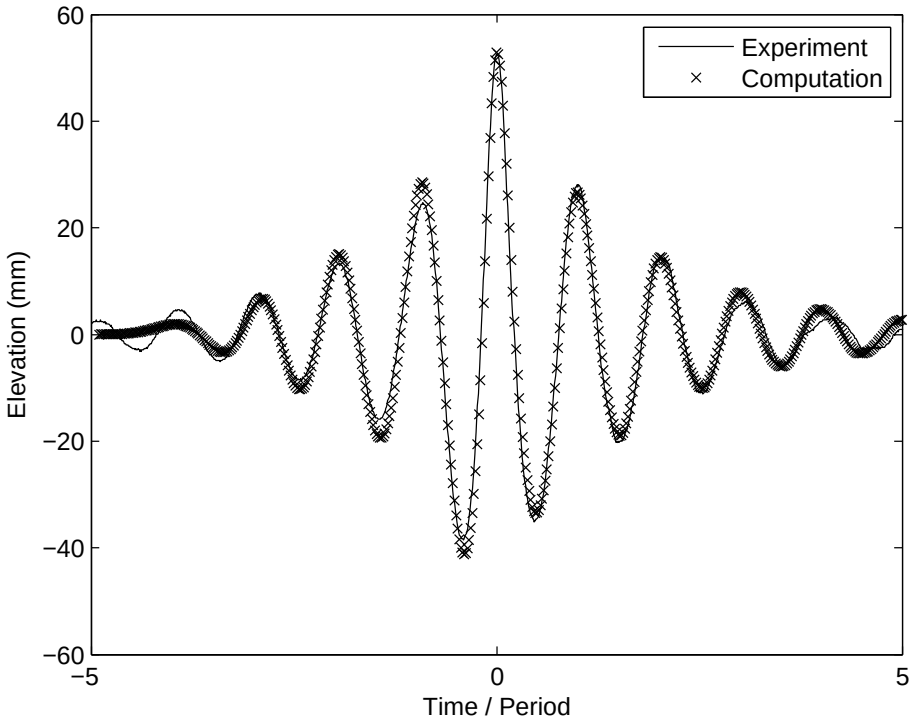

Figure 21: Reproducing the experimental wave

We here model the experimental wave as a second order NewWave, with amplitude 52 mm, and steepness $kA = 0.15$. Judging by the relative size of the troughs either side of the central peak, the focus location is slightly downstream of the measured location. Figure 21 shows an attempt to reproduce numerically this wave. The chosen focus location was 0.125 m downstream of the elevation gauge, which corresponds to 6% of a wavelength. It can be seen that this was too much of a compensation from focus, and a smaller correction of 0.05 m would have been a better choice.

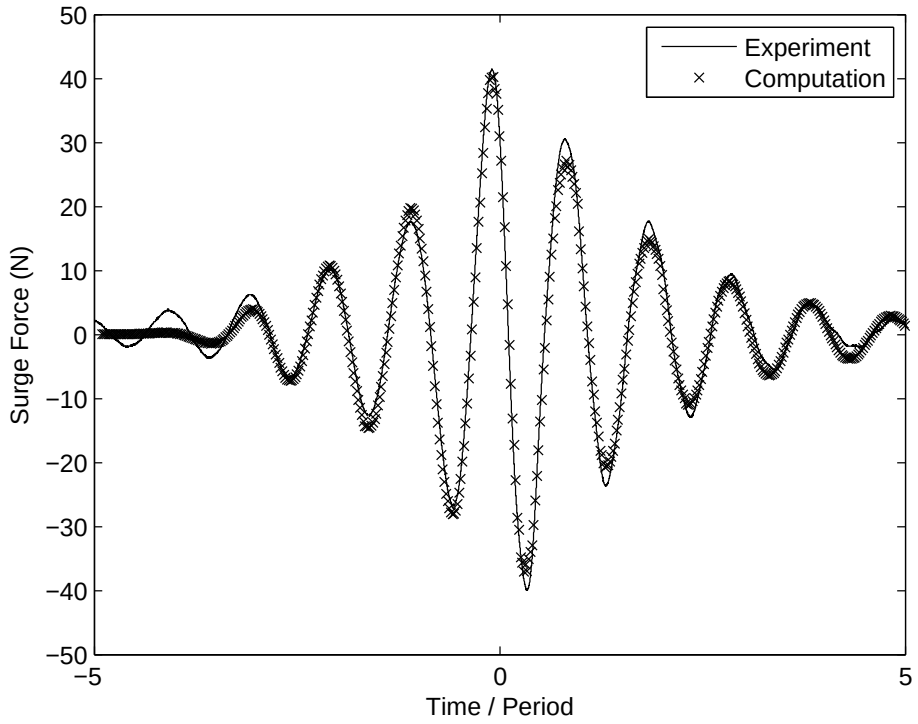

Figure 22: Reproducing the experimental force

Using this same incident wave, the surge force on a cylinder for both the experiment and computation is shown in figure 22. There is good agreement between the two. The computation overestimates the magnitude of the force before focus, and underestimates it afterwards, but this is consistent with the differences in the incident wave shown in figure 21.

5.2 Run-up and Heave Force for an Oscillating Cone

One of the features of some FPSO's is the flared bow, and the strongly nonlinear behaviour that this causes. For large motions the flared bow can often lead to overturning flow. Even for relatively small motions, this geometry can cause numerical problems associated with only partly resolving the very short scale features of the flow.

In order to validate the performance of the code with a flared object, we attempt to reproduce some experimental results reported by Drake et al. (2009).

The model used in these experiments was a right circular cone which is forcibly oscillated in heave by an electric motor. The initial draught is 148 mm, in water of depth 1.01 m. The experimental tank is rectangular, with a width of 2.5 m and length of 17 m, with the cone positioned centrally.

As reported in Drake et al. (2009), the vertical position of the cone $w(t)$ is given by a Gaussian wave packet

$$\begin{aligned} w(t) &= -A\mathrm{Re}\left(\sum_n \alpha_n \exp(i\omega_n t)\right), \\ \alpha_n &= \frac{1}{\sigma\sqrt{2\pi}} \exp\left(\left(\omega_n - \omega_0\right)^2 / 2\sigma^2\right) \Delta\omega, \\ \sigma &= \omega_0/2\pi, \end{aligned} \tag{67}$$

where A is the amplitude (the maximum heave displacement), ω_0 is the central frequency, and ω_n the discrete frequencies each $\Delta\omega$ apart which are used to represent the continuous spectrum.

The experiments were performed with amplitudes of 50 mm and 25 mm. The larger amplitude causes overturning flow, which the present simulations cannot handle, so we focus on the smaller 25 mm amplitude only. The experiments were repeated with central frequencies of $\omega_0 = n\pi/3$ rad $\cdot$ s^{-1}, for $n = 1, 3, \ldots 9$. For the lower frequencies, there is an issue with reflection from the tank walls in the experimental data. The reflection occurs only at low frequency because the long waves created by the radiation travel faster, and the oscillation of the cone takes more time to complete. Rather than model the effect of the reflection from the tank walls, we wish to demonstrate the damping method developed in this thesis and simulate a very small tank. For this purpose we can compare with the higher frequency experimental results at $n = 7$ and $n = 9$.

The size of the simulated tank is chosen based on the wavelength corresponding to the central frequency. The central clear region is of radius 0.25 wavelengths,

the high resolution region has a radius of 0.5 wavelengths, and the tank wall is at 1.5 wavelengths. For $n = 7$, these radii correspond to 0.287 m, 0.573 m, and 1.720 m. For the higher frequency case of $n = 9$, these lengths are shorter, at 0.173 m, 0.347 m, and 1.041 m. The computational mesh for the high frequency case is shown in figure 23.

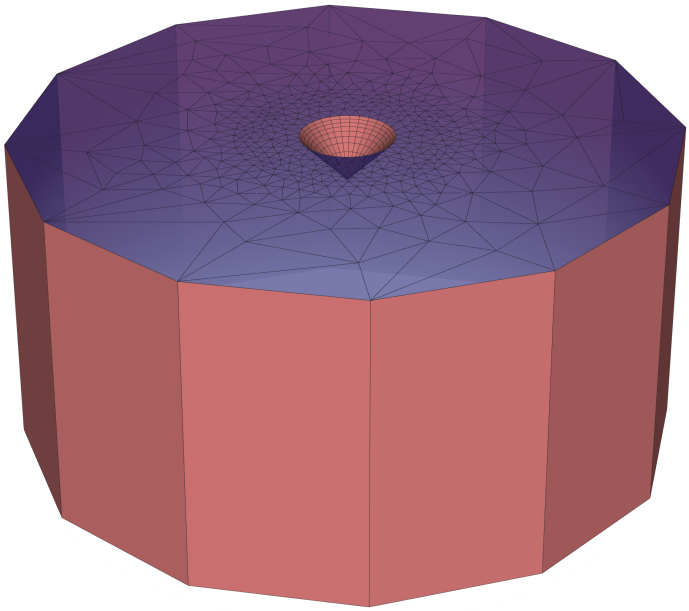

Figure 23: Cone mesh, $n = 9$

For the case $\omega_0 = 7\pi/3$ rad $\cdot$ s^{-1}, the nondimensional heave forces calculated by the simulation and the experimental results are shown in figure 24. There is quite good agreement between the two, despite the use of a very small tank.

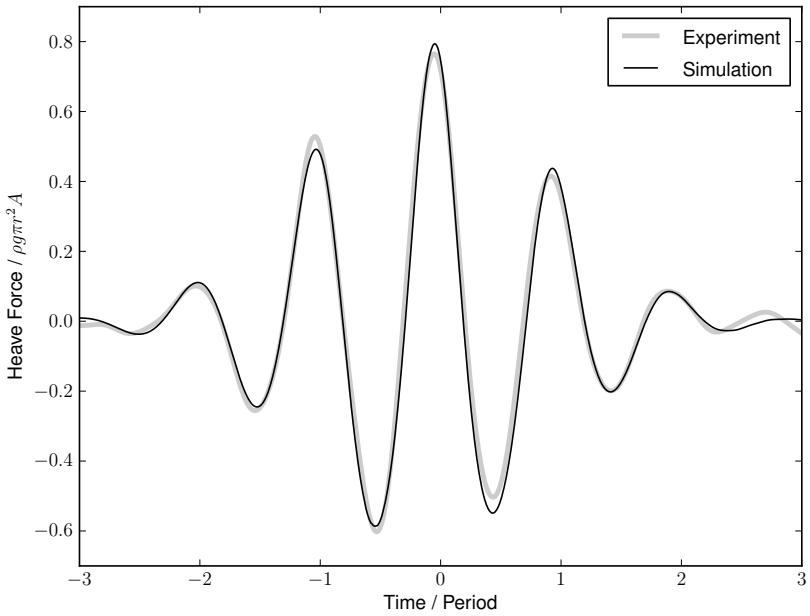

Figure 24: Heave force, $n = 7$

Figure 25 shows the the run-up at the high frequency case $\omega_0 = 9\pi/3$ rad$\cdot$s^{-1}, this time with a trough focussed motion. The simulation displays some interesting structure at the crest (around 0.5 periods after the minimum), which is perhaps evidence of the highly nonlinear behaviour. Unfortunately a filtering process has been applied to the experimental data as part of the data capture, and this has removed some of the high frequency information.

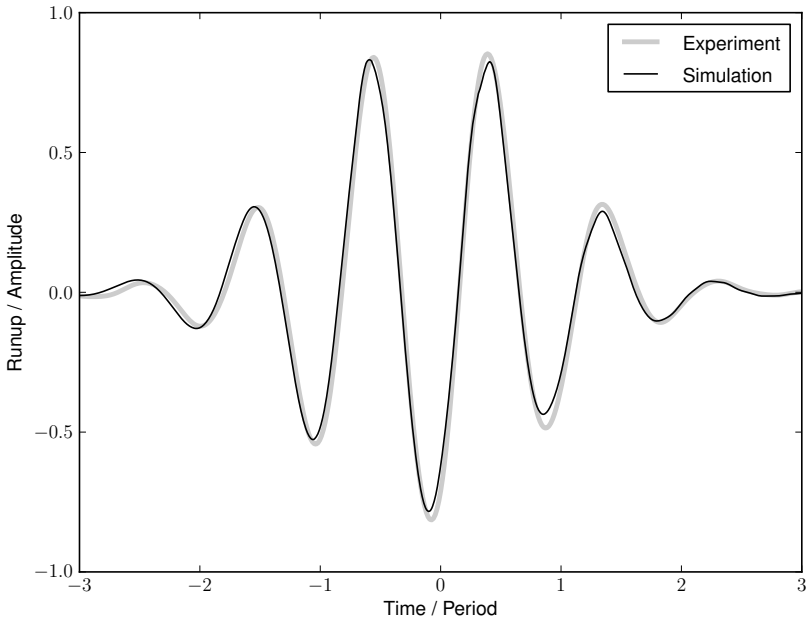

Figure 25: Run-up, $n = 9$

In order to examine the nonlinear behaviour, we perform simulations with both a crest focussed and a trough focussed oscillation, for $n = 7$. Figure 26 shows the heave force for these two simulations.

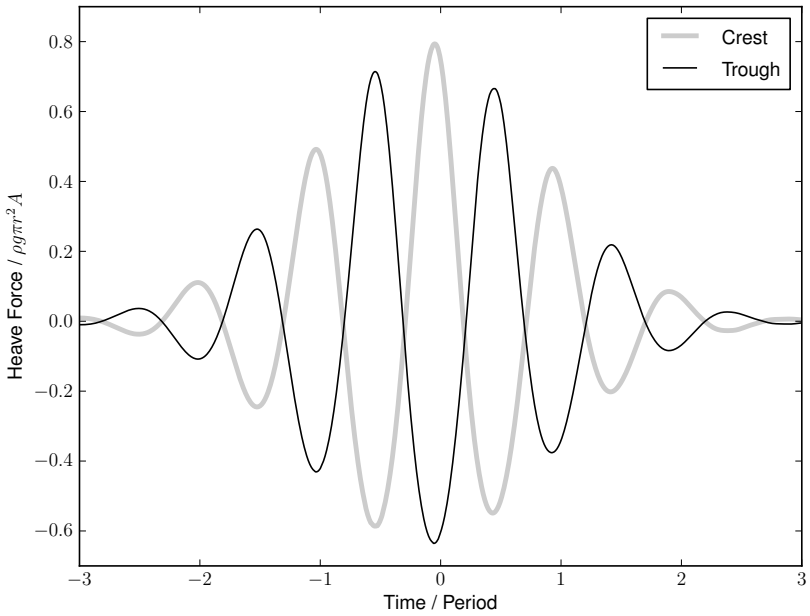

Figure 26: Crest and trough focussed forces, $n = 7$

By combining the crest and trough focussed simulations we are able to eliminate either the odd or even harmonics. Figure 27 shows the result of this procedure in the frequency domain. The linear term with a peak at $\omega = 7.3$ rad $\cdot$ s^{-1} is largest, but there is a significant contribution from second order effects at both the sum and difference frequency. Because the linear spectrum is sufficiently narrow, there is a clear separation between the sum and difference frequencies. It may also be possible to identify third order behaviour at the triple frequencies around 22.0 rad$\cdot$s^{-1}, although there is significant noise created at the intersection line.

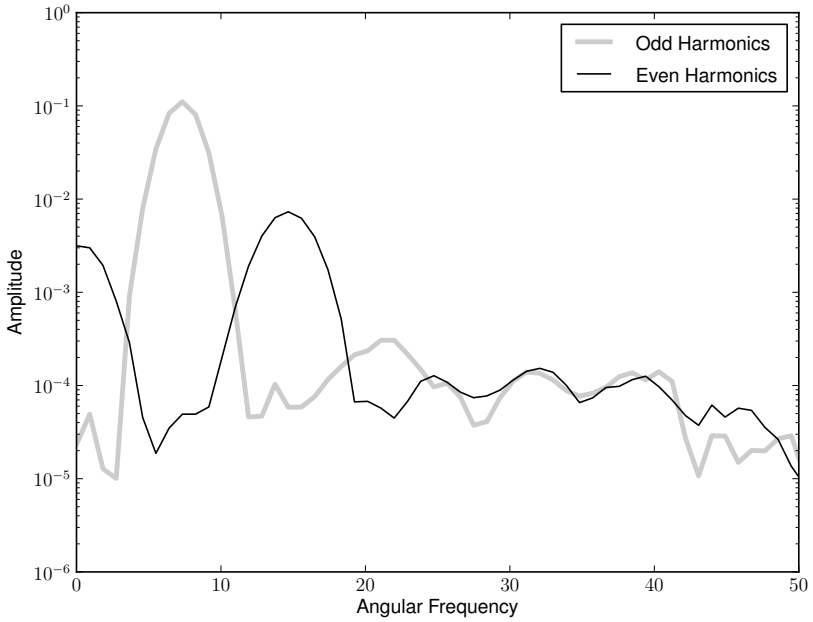

Figure 27: Force FFT, $n = 7$

5.3 Conclusion

In this chapter we have presented comparisons with two sets of experimental results: A fixed bottom-mounted cylinder and an oscillating cone. Both simulations show good agreement with the experimental results, and lead to further insight into the nonlinear effects.

These simulations also demonstrate the potential of the new wave damping and generation method described in section 4. Whereas the experiments were performed in large rectangular tanks, we are able to perform the comparsions with a small circular computational domain without the problems caused by reflection. For the cylinder case, this involves the simultaneous generation of an incident wave with the damping of the outgoing diffracted wave.

Having established the validity of the scheme, including the use of the new desingularized integral equation described 3.2, in section 6 we perform a more detailed investigation regarding an FPSO model. For this geometry we hope to

demonstrate not only agreement with experimental results, but that the numerical simulation can provide further understanding that goes beyond what is revealed by the experiments.

6 Wave groups incident on an FPSO

We also performed a series of fully nonlinear simulations for a focussed wave group interacting with a simplified FPSO model. For this purpose we selected the same geometry as used in physical wave-tank experiments reported by Zang et al. (2006). The goal was to reproduce the experimental results obtained by R. Gibson in a wave channel at Imperial College, demonstrating the ability to model the wave behaviour correctly, and investigating nonlinear diffraction effects.

The FPSO model may be described as a vertical sided cuboid with cylindrical ends. The total length of the model was 1125 mm, the width 325 mm and the draught 125 mm. The principal computational mesh used for the FPSO and surrounding water is shown in figure 28. Each boundary element shown is quadratic, either a 6-node triangle for the free surface elements or a 8-node quadrilateral for the solid surface elements. The elements on the underside of the FPSO are heavily distorted triangles, degenerate quadrilaterals, all sharing a common node at the centre of the flat underside. The low quality of the mesh in this region is not believed to cause any problems, as only the long wave components have any influence at depth, and these decay exponentially towards the centre of the underside. The motivation was to save on the number of elements required in a region of little flow, however an extra ring of structured elements might have been preferable in order to preserve the quality of the corner between the side and underside, or an unstructured mesh could have been used over the entire bottom surface.

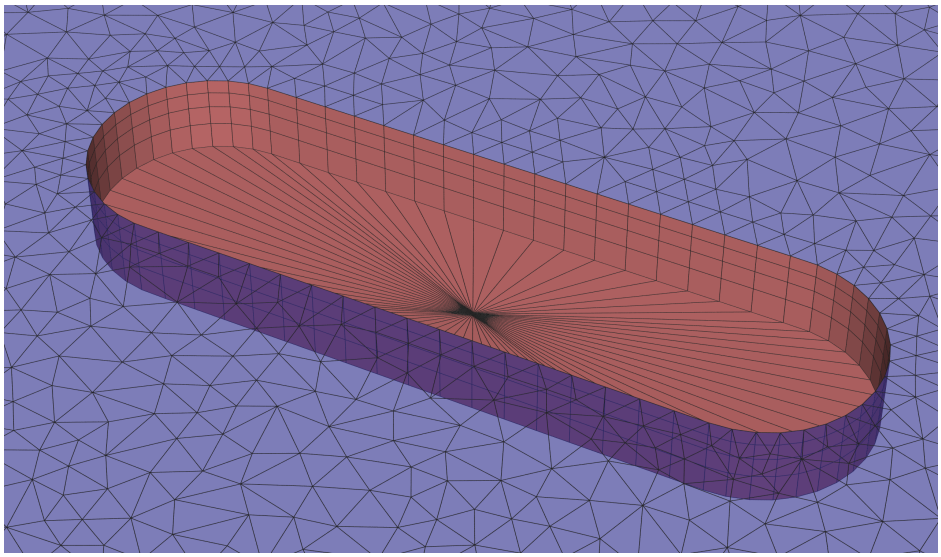

Figure 28: FPSO mesh detail

In the experiments analysed by Zang et al. (2006), the incident wave is nominally a plane focussed group based on a top hat spectrum. The wave periods are uniformly distributed between 0.8 and 1.2 seconds. This leads to a frequency range of $5.24 \leq \omega \leq 7.85$ rad $\cdot$ s^{-1}, but with a non-uniform distribution which is biased towards the lower frequencies. The experimental tank was a long rectangular channel of width 2.8 m, and depth 1.2 m.

In the simulations a constant time-step of 0.01s was used, corresponding to 100 steps per period, based on the average period of one second. The simulated time was from 4 seconds before focus at the bow until 8 seconds after.

Assuming linear dispersion, the components of the focussed group have a wavelength range of $2.24 \geq \lambda \geq 1.00$ metres. We used a circular numerical wave-tank of radius 4.5 m, which is only twice the wavelength of the long waves. The entire computational domain, including the FPSO at the centre, is shown in figure 29. The circular tank used in the simulation is different from the rectangular tank of the physical experiments, sharing only the water depth of 1.2 m

The mesh is required to have a high resolution in a circular region of radius 1.73 m, and a low resolution in the outer region. This resolution is imposed by

means of a minimum area constraint applied to the mesh generator. We first performed some simulations with a scale of 0.110 m and then later used a finer scale of 0.079 m in order to better resolve the third order wave components. A comparison of the results from these different resolutions is presented in section 6.3.

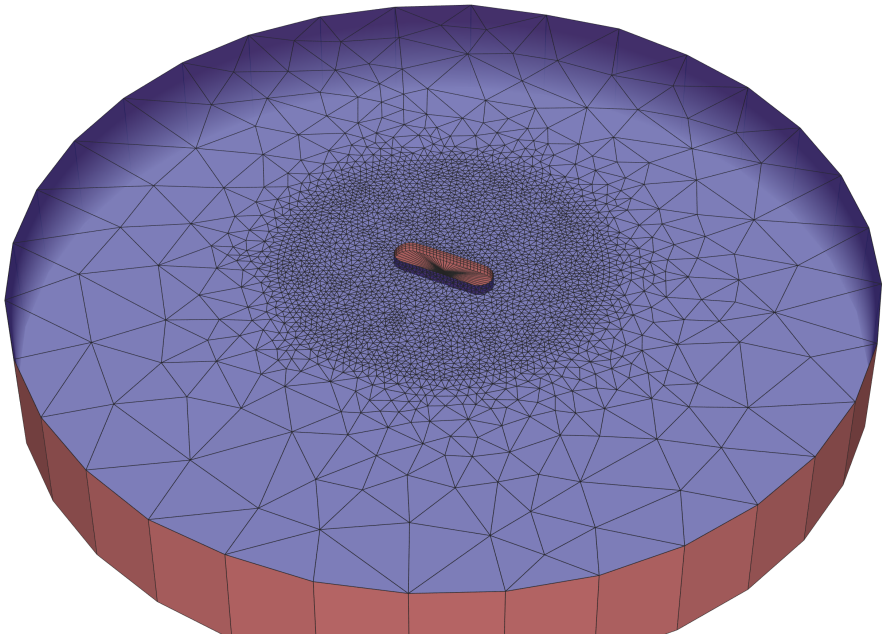

Figure 29: FPSO mesh

The wave damping/generation procedure was applied in an annular region, to produce the plane input wave and prevent reflections. The uncontrolled clear region at the centre of the tank is a circle of radius 1.42 m. At the bow and stern of the FPSO, this equates to a clear distance of 0.86 m between the FPSO and closest part of the controlled region. These measurements are indicated in diagram 30, along with the position of four named locations (Upstream, Bow, Side and Stern) at which we have analysed the elevation data. The "Bow" and "Stern" locations are 10 mm from the body, to coincide with the experimental data in Zang et al. (2006).

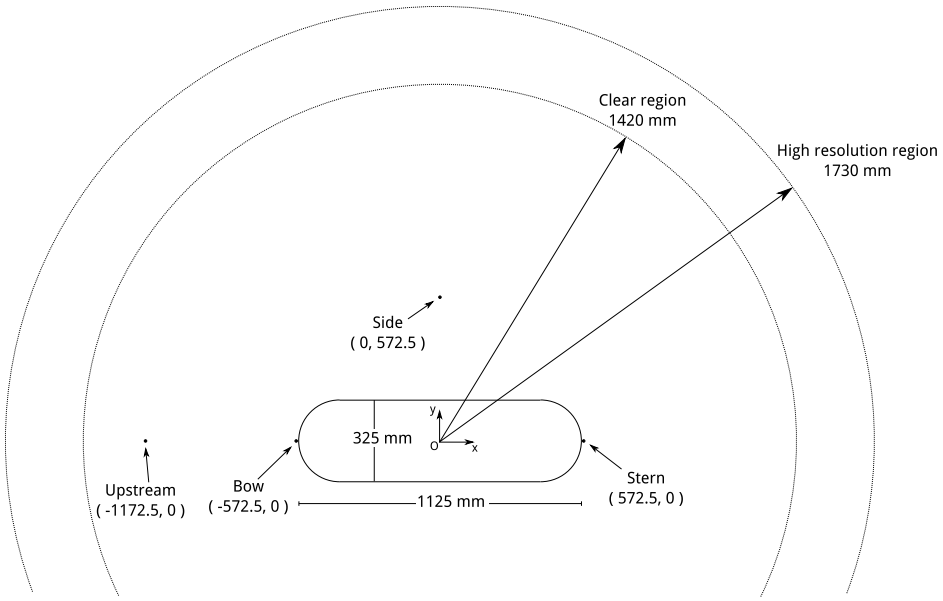

Figure 30: FPSO simulation dimensions

6.1 Reproduction of Experimental Wave

As mentioned previously, the nominal incident wave has a top hat spectrum, with a uniform distribution of wave periods. However, in the experiments analysed by Zang et al. (2006) this wave was created by a paddle and then allowed to propagate over a large distance before reaching the FPSO model. This extra travel time is important for the experiments, as it ensures that any slowly moving error waves created at the paddle arrive much later than the design wave, and do not interfere with the results. The disadvantage is that the wave profile may evolve during this travel time due to nonlinear effects.

As a result of the travel distance, we find that the experimental incident wave differs quite substantially from the nominal wave. The crests either side of the central peak are much lower than would be expected, as a result of the spectrum becoming broader. The wave group is asymmetric, indicating that the focusing of all wave components is not perfect. In our simulation, we want to keep the domain as small as possible, and attempting to replicate the incident wave by

applying the nominal spectrum would not provide a useful comparison. Instead, we can reproduce the incident wave from the experimental results.

There are two sources of data usable for this purpose. We have the elevation plotted in both the time domain and the frequency domain. Unfortunately in this particular case both have limitations as we are working from only what is published in Zang et al. (2006). The time domain data is only available for a fairly short duration, and this introduces considerable uncertainty in the frequency content. The frequency domain data only has magnitude information without the associated phases. Treating the magnitude data as if it were the real component and setting all the phases to zero creates a symmetric group. The difference between the two data sources is illustrated in figure 31.

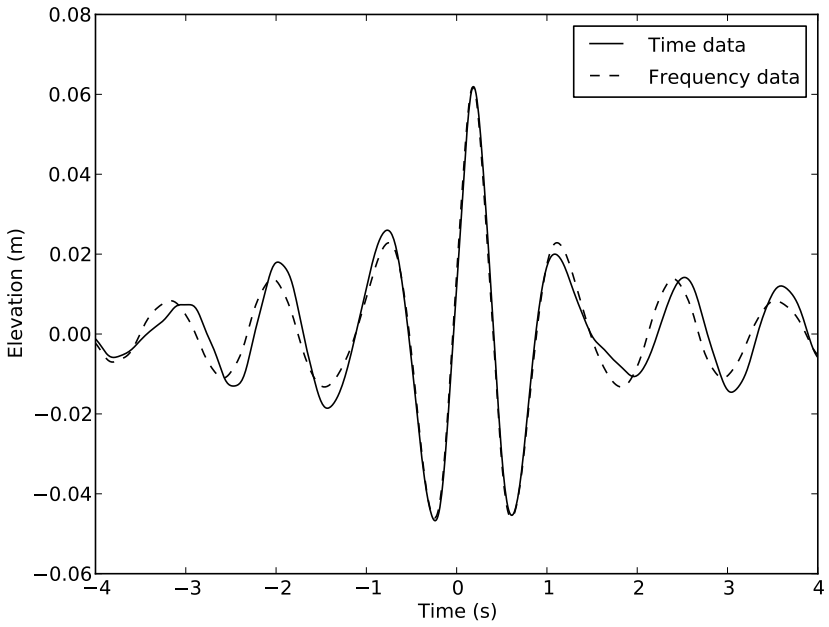

Figure 31: Linearized experimental wave

We used the time domain data, in order to capture the asymmetry. The result of applying this model of the experimental wave to our numerical tank is shown in figure 32. Results are shown for both a full amplitude simulation (with a linear

amplitude of 62 mm), and also a half amplitude simulation (31 mm) which is displayed at twice the vertical scale.

Unfortunately, the reproduction of this wave is not as exact as the comparable earlier work presented in section 4.3. We believe that this is primarily caused by third order effects. In section 4.3 we described how the wave generation procedure must be corrected to second order to avoid the creation of error waves. The wave generation used in the simulation is not correct to third order, and for the very steep wave in this case this higher order nonlinearity appears to be significant.

One third order effect is that the phase speed of the waves is slightly faster than indicated by linear dispersion. This can be seen in figure 32. The peak of the "Full Simulation" arrives earlier than requested, and is lower than the experimental wave because the group is out of focus. The "Half Simulation" wave arrives at the correct time, as the third order effects, which scale with amplitude cubed, are much smaller. The "Half Simulation" is also lower than the experimental wave at the central crest, but this is consistent with the reduced second order contribution which would be expected.

A different cause of some third order error is that the "linearized" experimental wave which we are attempting to reproduce also contains third order terms. It has been processed in a way that removes the second order nonlinearity, but not the third order (or higher odd harmonics). Treating the bound third order waves as if they were part of the linear spectrum would be expected to cause some error.

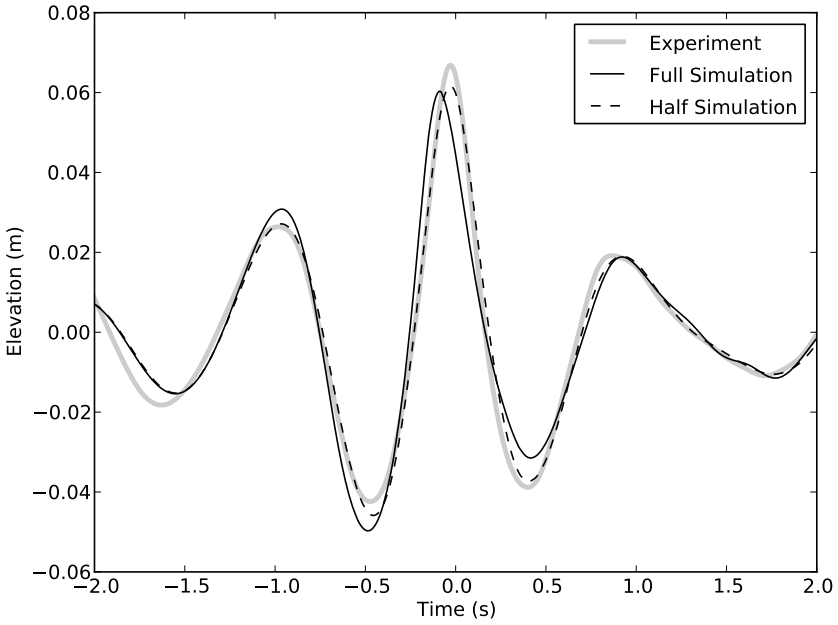

Figure 32: Reproduction of incident wave

6.2 Comparison with Experimental Results

The incident wave developed in the previous section to match the experiment has a linearized crest elevation of 62mm, leading to a steepness of $kA = 0.25$. Unfortunately we found that while the numerical wave tank could produce a wave of this size, it was too steep to obtain a stable computation with the FPSO in place, and we were unable to perform the simulation at full amplitude.

In order to provide a meaningful comparison from the simulations at half amplitude, we turn to the frequency decomposition method outlined in section 2.6. By performing a crest focussed simulation "C", and a trough focussed simulation "T", we are able to separate the linear from the second order components. This then enables the correct amplitude scaling to be applied to both the linear and second order part.

Figure 33 compares the elevation at the "Bow" location in figure 30 obtained in the experiment with the numerical simulation at half amplitude. Both the simple

linear reconstruction $2C$ and the 2nd order reconstruction $(C-T)+2\,(C+T)$ are plotted. The presence of the FPSO causes a large amplification of the central peak in the incident wave (figure 32), which is captured very well by the simulation. A large portion of this amplification is caused by 2nd order diffraction. The $2C$ reconstruction under-represents these 2nd order effects by a factor of two, and falls about 10% short at the peak elevation because of this.

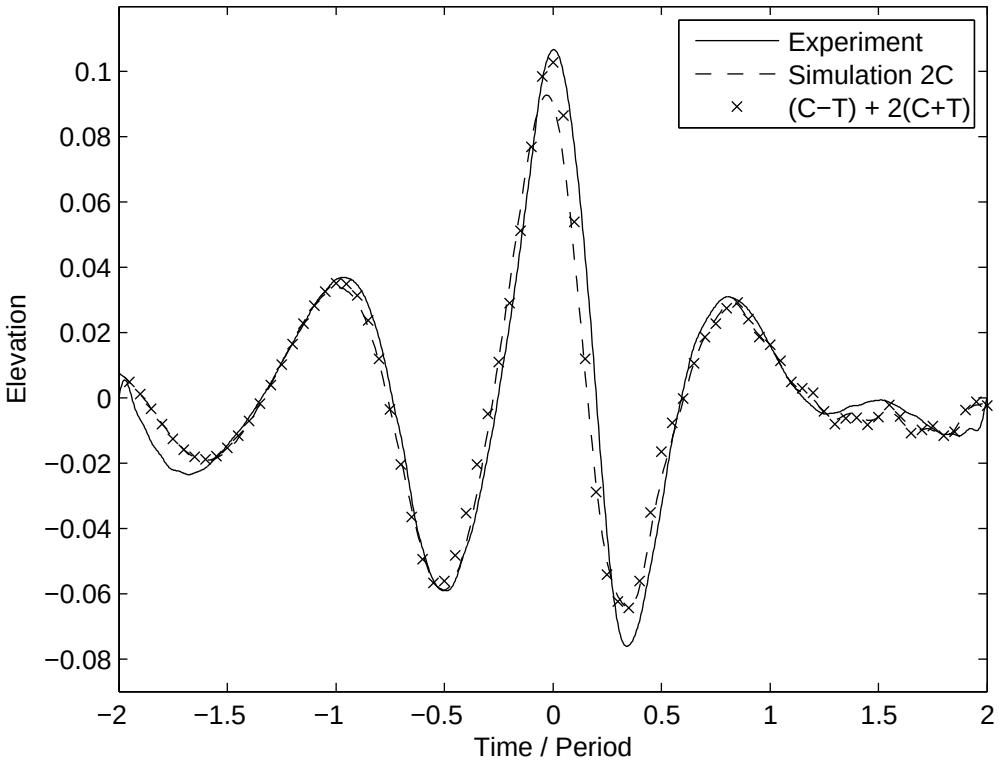

Figure 33: Elevation at bow

We now demonstrate the frequency decomposition of the elevation at the bow, and a comparison of this data with the results shown in Zang et al. (2006). Figure 34 shows the frequency content of the odd harmonics for the full amplitude wave, derived from $(C-T)$, with the FPSO in place. There is moderately strong linear diffraction, consistent with the size of the ship relative to the wavelength. There is very little 3rd order diffraction evident at this location, which would be visible at the 3rd order sum frequencies of 15 to 25 $\mathrm{rad}\cdot\mathrm{s}^{-1}$. Because of the simulation

being performed at half amplitude, the real 3rd order effects should be 4 times larger than shown in figure 34, but are still very small.

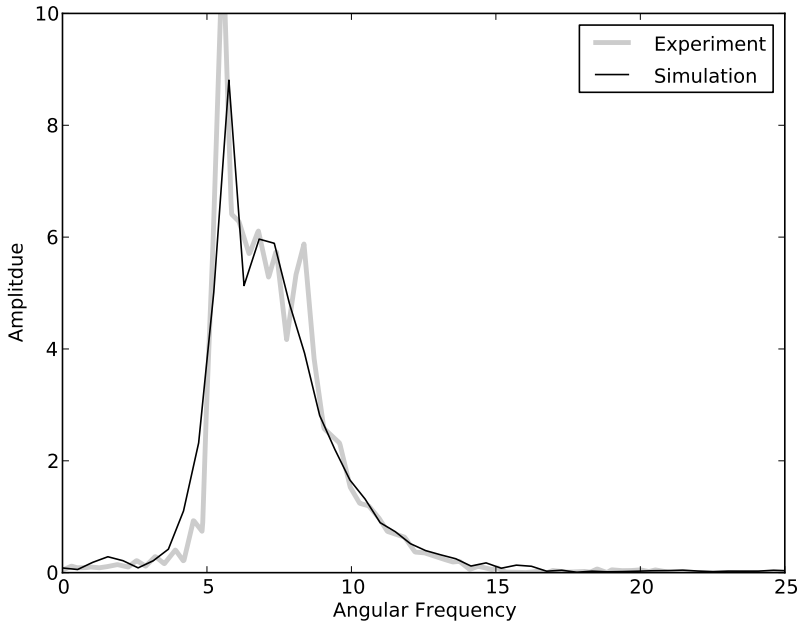

Figure 34: Frequency decomposition, odd harmonics

Figure 35 shows the even harmonics for the elevation at the bow. The second order terms have been scaled by a factor of four to represent the full amplitude experiment. The fourth order and higher terms are not scaled correctly, but are very small. There is again very good agreement with the experimental data. A small part of the second order elevation is due to the bound harmonics associated with incident wave, and also error waves in the experiment, but the majority is due to diffraction. This will be shown in section6.5.

The figure shows that there is a clear separation between the second order terms in the sum frequency range of 10 to 20 rad$\cdot$s^{-1}, and the difference frequency range of 0 to 5 rad $\cdot$ s^{-1}. The incident wave spectrum is sufficiently narrow that these regions do not overlap. This allows us to use frequency domain filtering to look at the sum and difference terms independently.

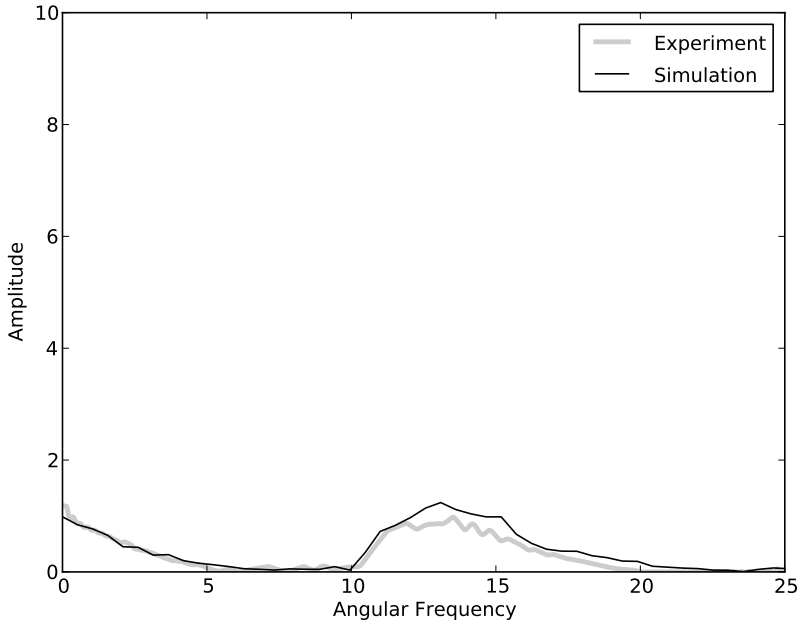

Figure 35: Frequency decomposition, even harmonics

By applying a frequency domain filter (a low pass rectangular window at $\omega = 7.5$) to the even harmonics, and then inverse Fourier transform, we get the second order difference contribution to the elevation at the bow shown as the time history in figure 36. The incident wave group has a small set-down. This is included as part of the wave generation, and then propagates the short distance across the tank as a bound wave. With the ship in place there is a substantial set-up at the bow, which contributes a significant amount to the peak elevation.

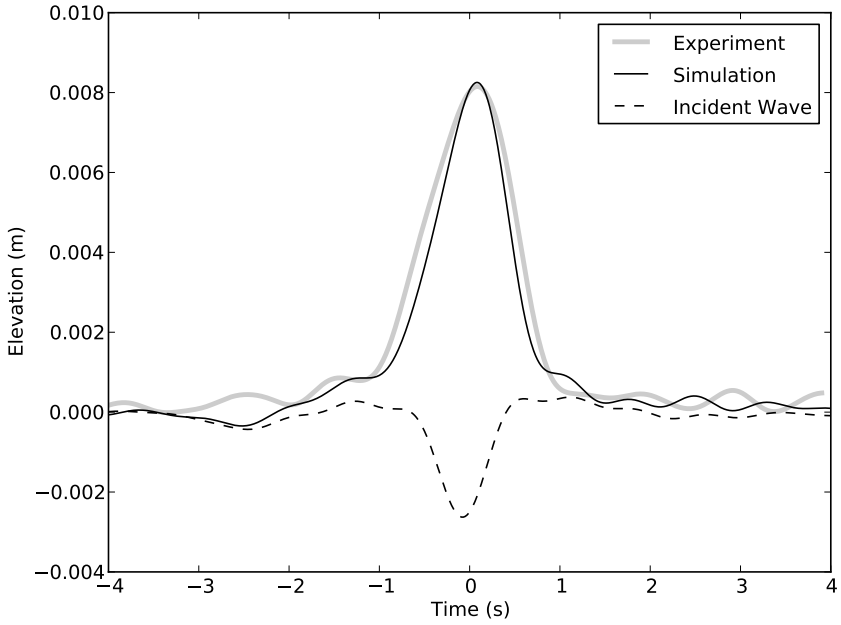

Figure 36: Second order difference component η_{20} at bow

Figure 37 shows the sum frequency elevation in the time domain. There is a small second order wave group bound to the incident wave, and a much larger group caused by the diffraction process. Unfortunately the experimental data for the sum term is not presented in the paper by Zang et al. (2006). However, given the accuracy of the total elevation in figure 33 and the difference component in figure 36 the behaviour seems correct.

There is a starting transient in the periods before focus, as the incident wave must travel across the clear region. After focus, the behaviour of the sum term is rather unstructured, but this is consistent with the behaviour of the linearized incident wave shown in figure 31. It is also possible that the elevation away from focus is partly due to the rectangular frequency filter creating a sinc function in the time domain, even though there is very little energy around the cutoff frequency.

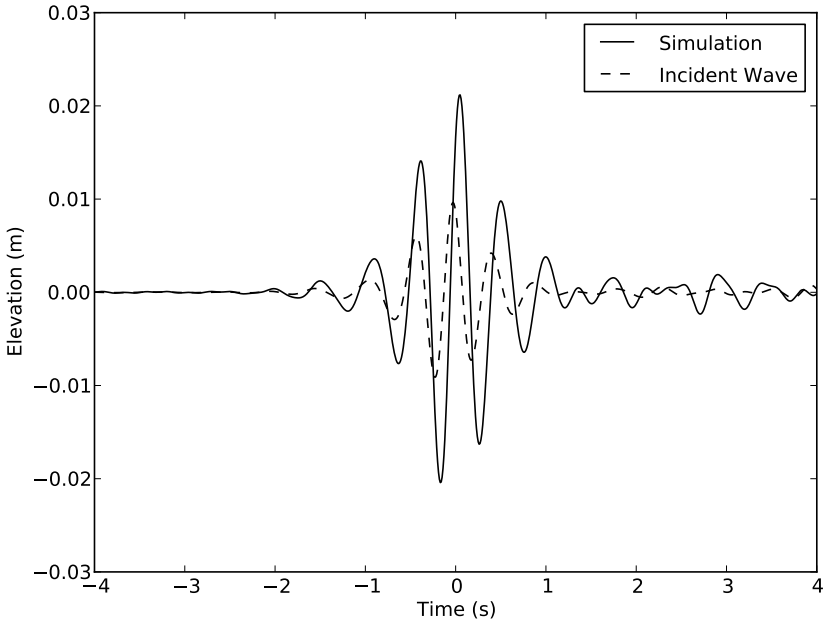

Figure 37: Second order sum component η_{22} at bow

6.3 Convergence

In order to investigate the convergence of the simulations, some calculations were repeated using both a coarse and a fine mesh. The length scale of the coarse mesh was 0.110 metres and the length scale of the fine mesh was 0.079 metres. These scales were again imposed as a maximum area constraint on the mesh generation.

Figure 38 shows the simulated elevation near the bow of the FPSO for both the fine and the coarse mesh. The linear part, obtained from a wave of small amplitude, is given for comparison. There is very good agreement at the focal crest and surrounding peaks. Both the mesh resolutions are able to capture the same nonlinear behaviour. There is a substantial amount of very high frequency noise visible from +1 to +2 seconds. The frequency of this noise corresponds to wavelengths at the resolution limit of the triangular mesh, as is shown by the different period of the oscillations observed with the fine and coarse mesh. This high frequency noise accumulates at the bow because the short wavelengths

cannot propagate through the irregular mesh. At other locations, such as shown in figures 39 and 40, this noise is not observed.

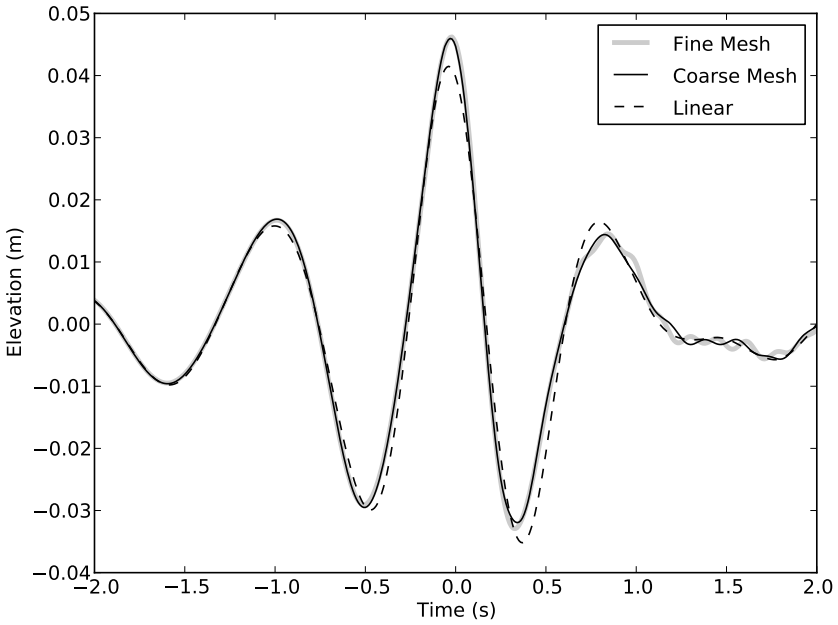

Figure 38: Convergence at bow

Figure 39 compares the simulated elevation at the "Stern" location in figure 30 for the two mesh resolutions. The agreement is good, although less exact than near the bow in figure 38. One reason for this is the importance of third order diffraction effects at this location. The coarse mesh does not have sufficient resolution to fully represent the third order behaviour, leading to a discrepancy, particularly after the main wave group has passed. At the bow, where the third order contribution is very small, the convergence is good. To demonstrate convergence of the third order diffraction, an even finer mesh would be required, but nevertheless the third order results from the fine mesh simulation appear to provide useful physical understanding, as discussed below.

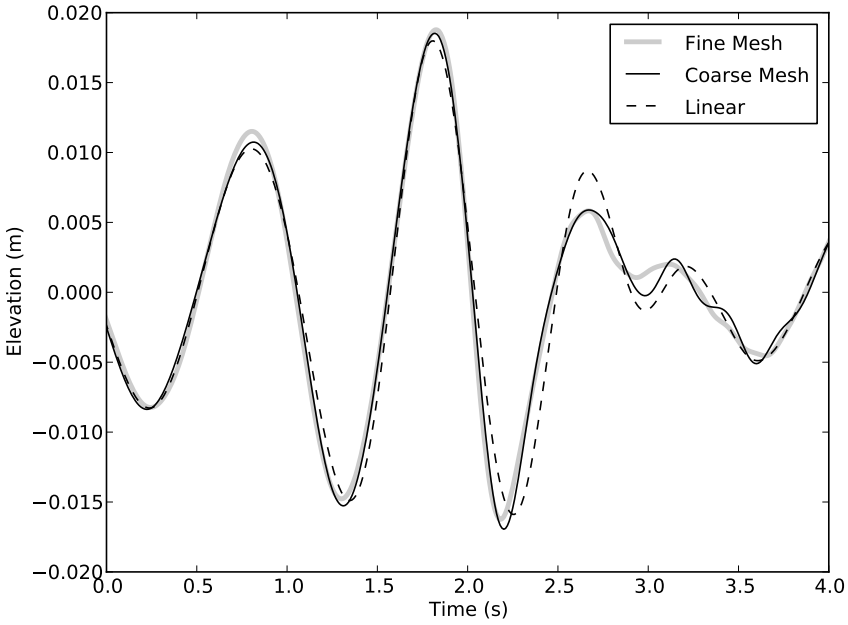

Figure 39: Convergence at stern

The accuracy of the second order results is further supported by figure 40. This shows the elevation at a point to the side of the FPSO. At around +2 seconds we can see the interference between the focussed group and the wave diffracted from the bow. There is a large second order component to this diffraction which is not present in the linear results, but is agreed on by both the fine and coarse meshes.

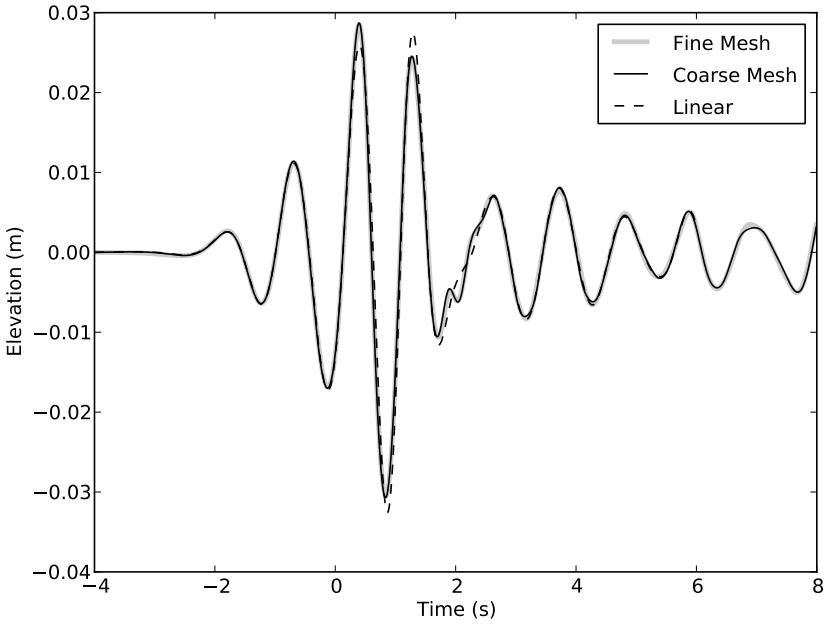

Figure 40: Convergence to side

6.4 Fourier Transforms

In order to understand the nonlinear behaviour of the system, both the physical effects and numerical artefacts, it is instructive to examine the frequency content of the simulation results. This form of analysis allows us to predict the scaling with wave amplitude, and identify areas where a simple linear simulation would be inaccurate in predicting the onset of green water or slamming events.

Figure 41 shows the Fourier transform of the elevation at the bow, on a log scale. Similar information was shown previously on a linear scale in figures 34 and 35, although in those figures the results were scaled to represent an linearized incident wave of amplitude 62 mm. In this section the results for the simulated wave of 31 mm are presented without modification. The "Even Harmonics" are obtained by the combination $\left(\eta^0 + \eta^{180}\right)/2$, the "Odd Harmonics" by $\left(\eta^0 - \eta^{180}\right)/2$, and the "Triple Harmonics" by $\left(\eta^0 + \eta^{120} + \eta^{240}\right)/3$.

The strong second order diffraction can be clearly seen, both in the even

harmonics at the sum frequencies, and the overlapping even and triple harmonics at the low difference frequencies. At this location there is no evidence of third order diffraction, which agrees with the experimental results of Zang et al. (2006).

To the right of figure 41 there is a large amount of noise created by the simulation. The peak at 40 rad $\cdot$ s^{-1} corresponds to the scale of the mesh, and saw-tooth like oscillations. This noise is primarily created at the intersection line between the body and the free surface, particularly at the bow where the incident wave is largest.

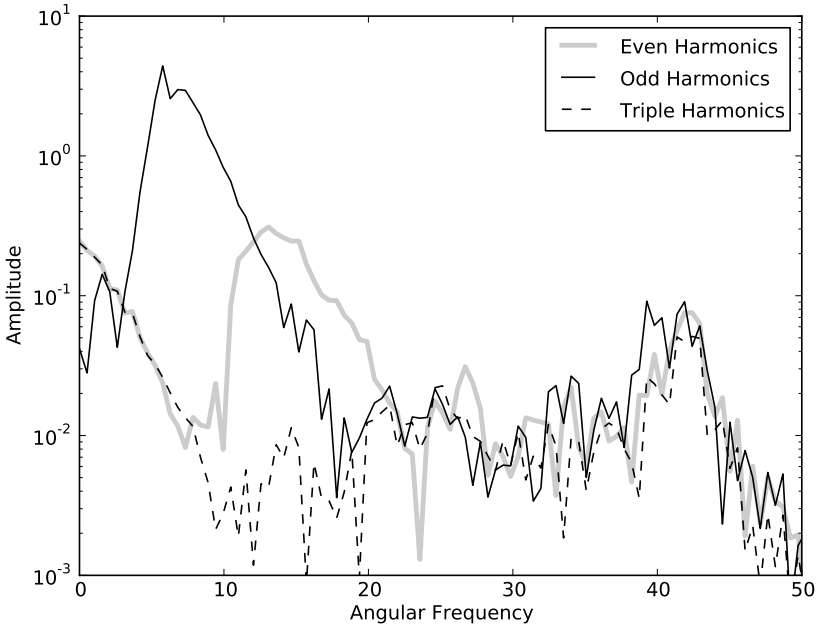

Figure 41: Spectrum at bow

Figure 42 shows the corresponding spectrum at the stern. The first order peak is reduced in size, because of the sheltering effect of the FPSO. In contrast to the bow, there is evidence of third order diffraction at this location. The curves for "Odd Harmonics" and "Triple Harmonics" both agree on the amplitude and frequency of a third order sum term around 20 rad $\cdot$ s^{-1}. The noise level is lower than at the bow, but still with a strong peak corresponding to the size of the

elements.

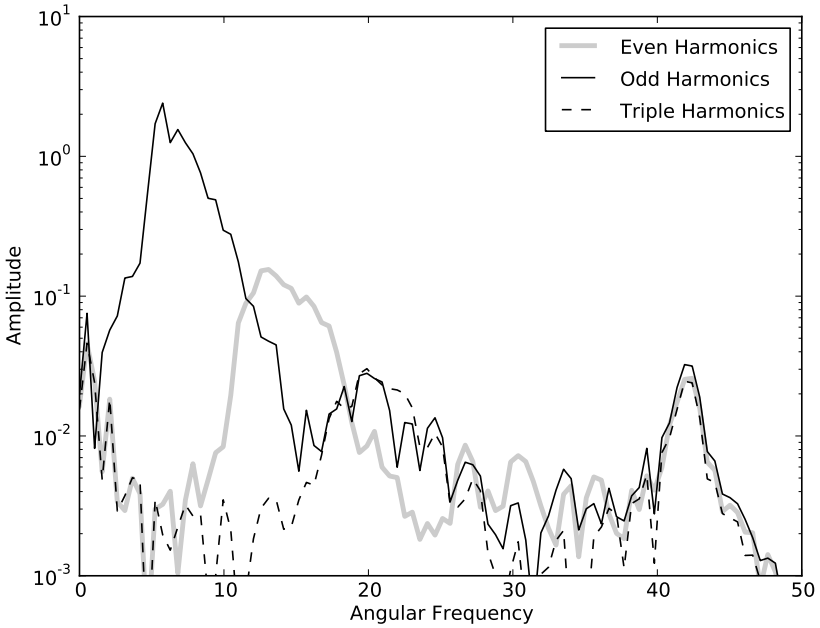

Figure 42: Spectrum at stern

Both figures 41 and 42 displayed the spectrum at locations adjacent to the FPSO model. These positions cannot verify that the diffracted wave is correctly propagating away from the body. Figure 43 shows the frequency data at the location to the side of the model. The coordinates of the point "Side" are indicated in figure 30.

The third order wave is clearly visible at this location, confirming that the mesh resolution is sufficiently fine to propagate waves in this frequency range. The high frequency noise is vastly reduced; these components are trapped near the intersection line where they are generated. There is possibly an indication of fourth order sum frequency terms in the even harmonics near 30 rad $\cdot$ s^{-1}, although this is small and overlapped by part of the third order spectrum.

The second order difference term is present but much smaller than is evident at the bow. Rather than representing the large set-up associated with diffraction, away from the body there is only the bound set-down which travels with the wave

group. The second order sum frequencies display a notable split peak. This may be the result of interference between the bound wave and the free wave created by the diffraction.

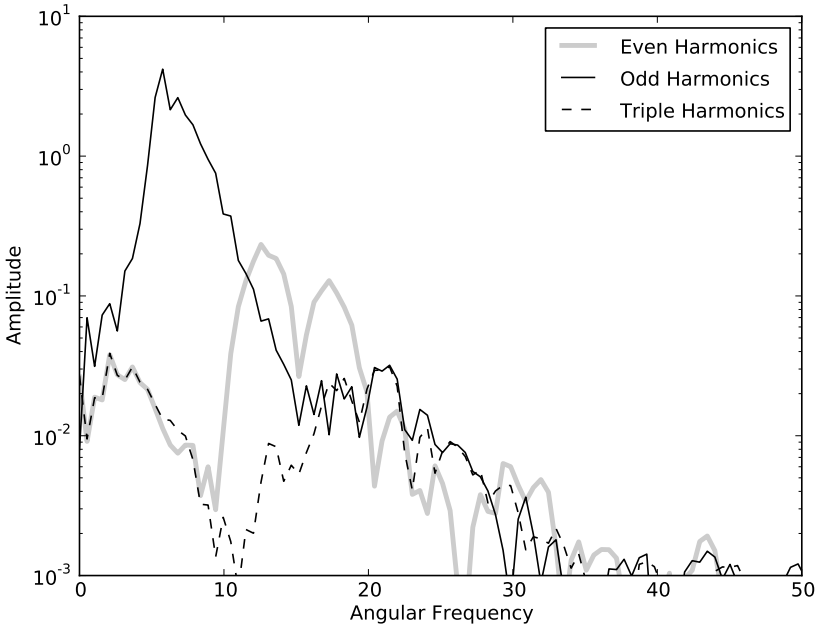

Figure 43: Spectrum to side

6.5 Nonlinear Decompositions

In this section we analyse the major nonlinear components at the four locations shown in figure 30. The third order sum term η_{33} is obtained by taking the triple harmonics $\left(\eta^0 + \eta^{120} + \eta^{240}\right)/3$, and then filtering out the low frequency component. Not shown is the η_{31} term. It is difficult to filter this component from the large linear η_{11} term, and to separate any nonlinear diffraction effects from the third order phase speed increase.

The second order terms η_{20} and η_{22} are obtained from the even harmonics $\left(\eta^0 + \eta^{180}\right)/2$ and applying a frequency domain filter to separate them. As can be seen from the figures in section 6.4, there is a clear enough distinction in their frequency ranges that this filtering is successful. Additionally, the fourth order

components (η_{40}, η_{42}, and η_{44}) have been removed by combining results from the simulated 31 mm waves with smaller 15.5 mm waves.

Figure 44 shows these nonlinear components at the upstream location. To the left of the figure, around one second before the focus at the bow, we see the bound components of the incident wave. The second order difference term is a small set-down. To the right of the figure we see the reflected wave which has reached the FPSO model and travelled back again. The second order sum term is comprised of both a small wave bound to the linear reflection, and a slower free wave.

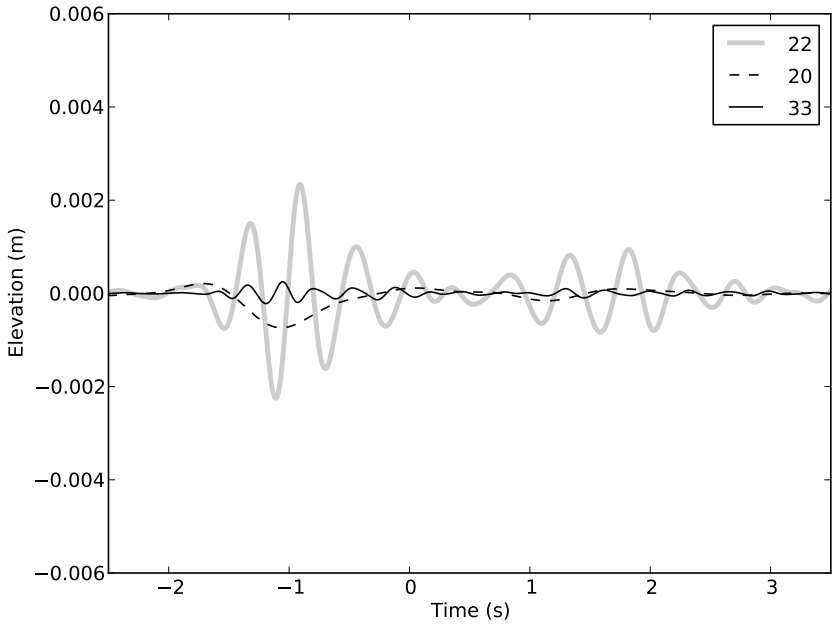

Figure 44: Nonlinear components upstream

Figure 45 shows the nonlinear components at the bow. There is a large amplification of the second order components at focus. The bound set-down of the incident wave becomes a much larger set-up. As might be expected from the spectrum in figure 41, there is very little third order diffraction at this location. The third order components are no larger than what is bound to the incident wave in figure 44. After focus, the oscillation in the η_{33} term may be non-physical noise

created at the intersection between the body and the free surface.

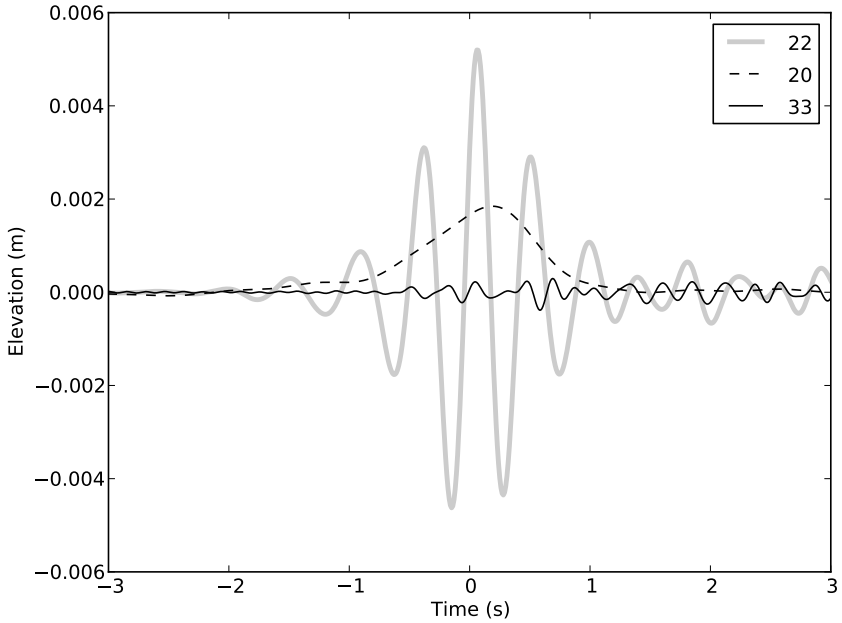

Figure 45: Nonlinear components at bow

At the stern, shown in figure 46, the incident wave is slightly out of focus due to dispersion. This would cause the second order sum packet to be longer and smaller. In addition to the dispersion, second order free waves travel more slowly and arrive later, further elongating the packet. The second order difference term is very small; the bound set-down appears to nearly cancel with the diffracted set-up at this location.

In contrast to the bow, there is a sizeable third order component here, larger than in the incident wave. This third order part appears to be mostly contained within the second order envelope, suggesting that the cause is diffraction effects at the stern, rather than slow free waves from diffraction at the bow.

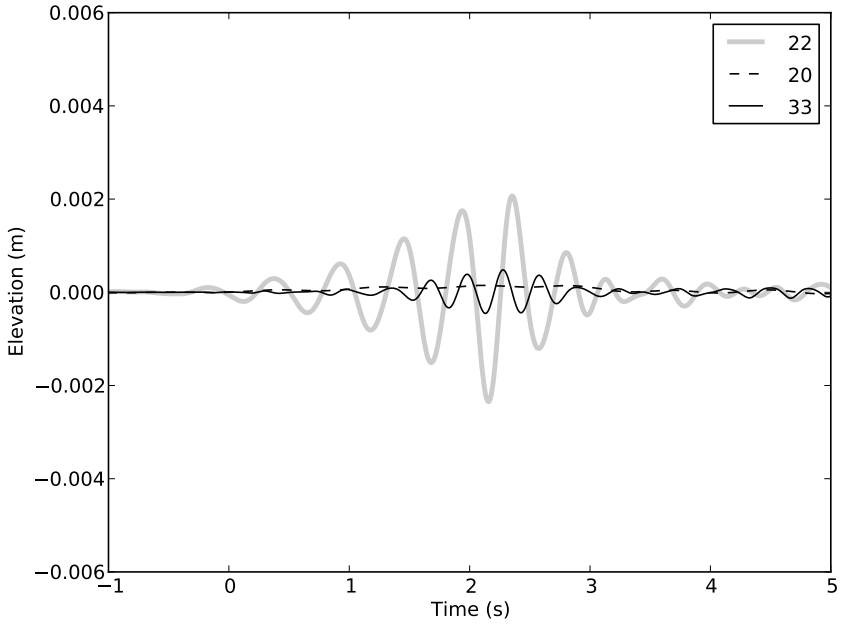

Figure 46: Nonlinear components at stern

Figure 47 shows the components at the side location. Similar to the upstream location in figure 44, we see two packets, first the incident wave, and later the reflection. There is interference between these two waves at around 1.5 seconds.

In comparison with the upstream location, the diffracted second order component here is much larger, as can be seen by the behaviour of the η_{22} component around 2 seconds after the focal event. This is partly because the side location is closer to the body, but also indicates that the second order diffraction has a preferential direction, radiating out to the side more than upstream. This directionality can be seen clearly in the visualizations in section 6.6

The diffracted third order component is larger than the bound incident wave. This indicates that there is significant higher-order diffraction, which is not evident at the bow in figure 45. The third order part arrives later than the second order, confirming that it travels more slowly and is indeed a free wave of high wavenumber.

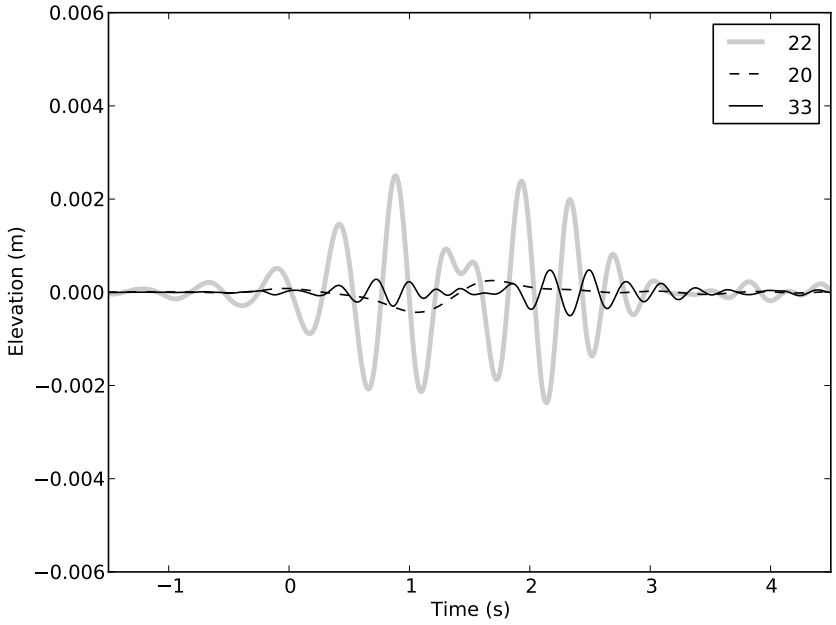

Figure 47: Nonlinear components to side

6.6 Free Surface Visualization

A major advantage which numerical simulations hold over physical experiments is the time history of the entire surface. Whereas an experiment has a limited number of wave gauges and video camera angles, the output of a simulation allows for a much more general post-processing and analysis.

An efficient procedure was developed to combine the results of multiple simulations. This allows two surfaces to be added together, which can be used to extract just the diffracted wave-field, or find harmonics by combining waves of different phases. Each simulation is performed on its own mesh with moving particles, and must be interpolated by a Cartesian grid before any combinations can be calculated.

6.6.1 Diffraction and Incident Wave

Figure 48 shows a comparison of the incident wave from section 6.1 with the diffracted wave-field that it causes. Each image is separated by one second in time, from 2 seconds before focus in the upper left image, to 5 seconds after focus in the lower right. The third image is at the focal time. The circular area (or two semicircles) does not show the entire computational grid, including the low resolution area which can be seen in figure 29. Only a region of radius 2m is displayed, compared to the tank radius of 4.5m. The wave generation and damping mechanism intrudes on the outer 0.58m of the displayed region, while the inner 1.42m is unconstrained.

In the upper half of each image we see the plane incident wave as it travels from left to right. Because the phase speed is dependent on frequency the profile changes, reaching a maximum elevation at focus, and deep troughs one second either side. The vertical axis is scaled so that it is displayed with a maximum height of 0.2m. The actual maximum elevation of the incident wave is 0.26m at focus, so in this case the incident wave has been slightly shortened for display. It can be seen from the focal time image that this is a steep wave, even when displayed slightly shorter than to scale. The full amplitude wave in the experiments of Zang et al. (2006), for which we were unable to compute the interaction, was twice as steep again.

In the lower half of each image is the diffracted wave-field which is caused by the incident wave. The outline of half the FPSO model is visible at the centre. The diffracted wave has a maximum elevation of 0.15 m, and is also scaled to a height of 0.2 m for display. In the first image, at -2 seconds, we see only artefacts created by the wave generation region. At -1 second, there is a small broad set-up visible around the entire FPSO. At focus there is a large peak at the bow which is in phase with the incident wave. In the later images we see circular

waves radiating outwards. These are both linear and 2nd order free waves. At +2 seconds there is a second large peak at the stern, this time out of phase with the incident wave. Finally at +4 and +5 seconds we see only radiating waves as they reach the damping region, and high frequency short waves left behind.

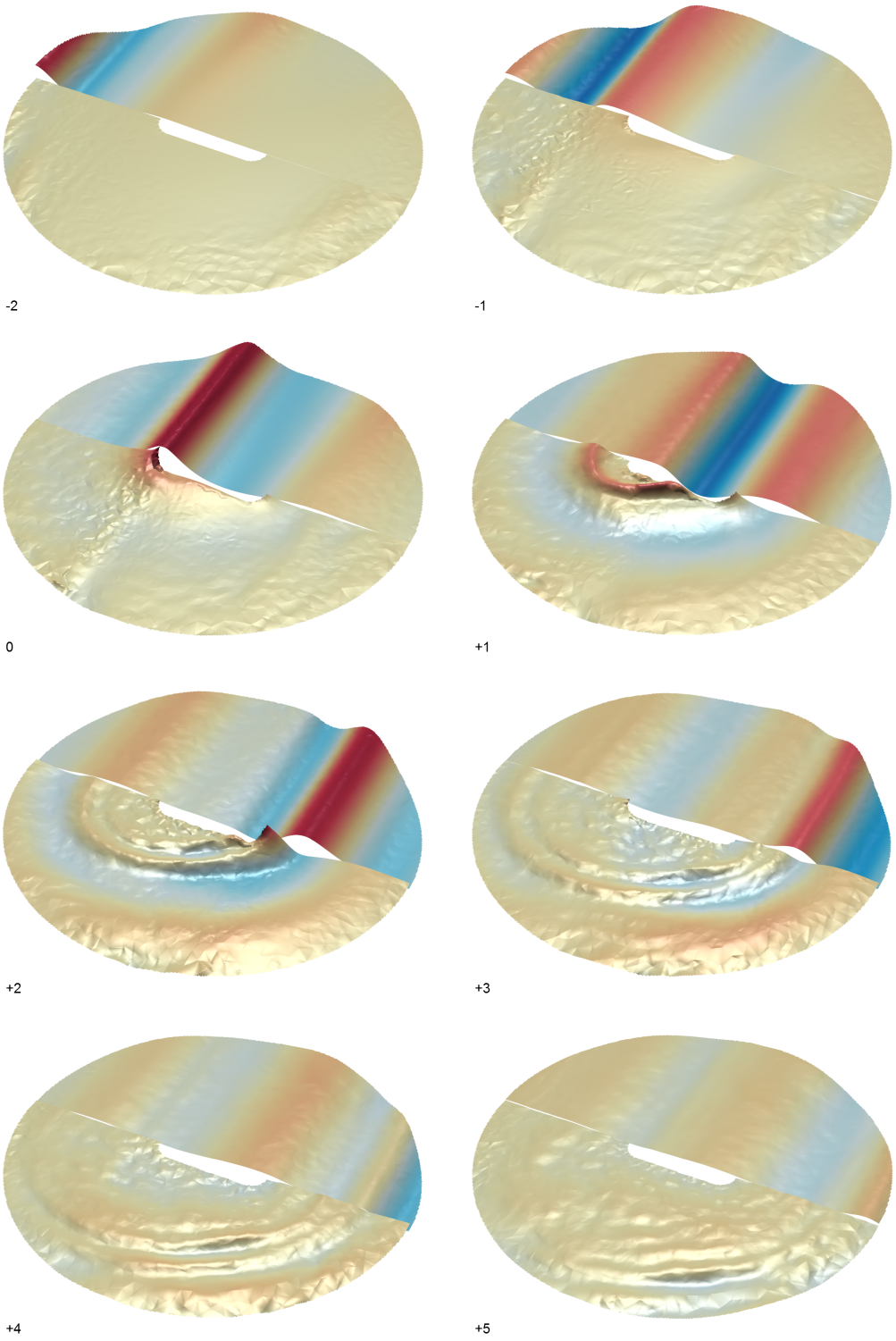

Figure 48: Incident wave (above) and diffracted wave-fields (below)

6.6.2 Second Order and Total

In order to examine the nonlinear behaviour, we can combine crest and trough focussed waves in order to extract different harmonics. Figure 49 compares the even order harmonics ($(C+T)/2$) with the crest focussed wave (both incident and diffracted parts). The maximum elevation of the total wave is 0.39 m, and the even harmonics 0.065 m. They have both been scaled to an elevation of 0.2 m in the figures.

The upper half of the plot shows the total wave, which is broadly similar to the incident wave shown previously. The effects of linear diffraction can most easily be seen in the broad peak at focus, and in the sheltering effect behind the stern at +2 seconds. The more visible outgoing waves are of short wavelength and are second order.

The even harmonics display several important features. Away from the FPSO, we can see the second order bound wave travelling with the group. This bound wave is composed of a short wavelength sum frequency component and a set-down from the difference frequencies. At focus there is a very sharp peak at the bow, again composed of sum and difference frequency components. The difference frequency set-up is not visible at -1 or +1 seconds, which is consistent with figure 36.

Most striking is the second order free wave which radiates outwards. There are two prominent crests which travel more slowly than the incident group, and get left behind by +3 seconds. There is preferential radiation to the sides and behind the FPSO, with the wave radiated directly upstream being much smaller. This directionality for the second order radiation matches that described in Buldakov et al. (2004) for diffraction by a cylinder.

As the radiated wave spreads out it reduces in size. The effect of the damping region can be observed by a comparison of the final two images. At +4 seconds

there are two crests of similar size, and at +5 the leading crest has entered the damping region and begun to reduce in size.

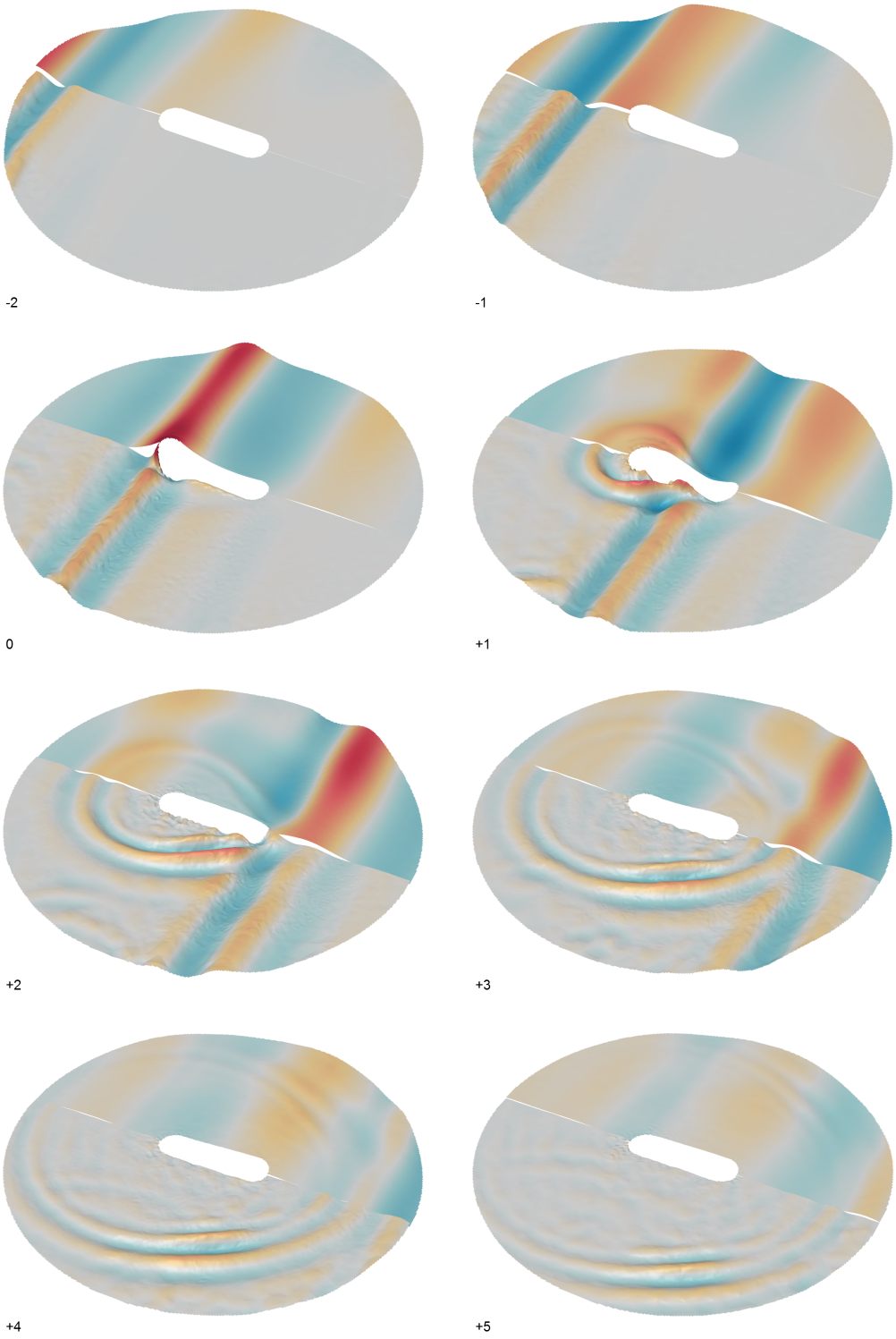

Figure 49: Even harmonics (below) and total wave-field (above)

6.6.3 Second Order Sum and Difference

It is instructive to look at the second order sum and difference terms separately. For the elevation at a single point (figures 36 and 37) we applied frequency domain filtering to separate them. The same technique could in principle be used for a surface plot, requiring a calculation of the fourier transform at every displayed surface point.

As an alternative we can separate the components by performing new simulations with phase shifts of 90° and 270°. These correspond to waves with the steepest forward and backward slope at focus. By combining the elevations from these new simulations we can extract the double harmonics without the low frequency term $(\eta^0 - \eta^{90} + \eta^{180} - \eta^{270})/4 = \eta_{22} + \eta_{42}$, and also the fourfold harmonics $(\eta^0 + \eta^{90} + \eta^{180} + \eta^{270})/4 = \eta_{20} + \eta_{40} + \eta_{44}$. Neglecting the fourth order contibutions, these provide the second order sum and difference terms without performing any frequency domain filtering.

On the left hand side of figure 50 we see the 2nd order sum frequency, this time travelling away from the camera. Most of the features of this component were discussed previously, as they were visible in figure 49. The peak at focus is lower than the complete 2nd order contribution shown in figure 49, as a large part of the peak elevation is due to the difference term. Looking sideways from the bow at focus, there is a distinct trough as the radiated wave forms. There is a very deep trough visible at +1 second to the side of the FPSO.

The right hand side shows the 2nd order difference frequency. Here we can see the bound set-down and the set-up at the bow at focus. The separation procedure has also incorporated the 4th order term and η_{44}. These waves are really too short to be accurately resolved by the mesh, but are visible because they are relatively steep. They can be seen without much coherent structure near to the FPSO in the final 4 images. At +1 second it is possible to make out a radiating 4th order

wave. We can infer that this is the η_{44} term as it has radiated at the same speed, but has half the wavelength of the corresponding 2nd order wave, which is visible in the left half of the image. This is not a free 4th order wave, which would have an even shorter wavelength, but is instead bound to the 2nd order wave. Just as a 1st order free wave develops a bound 2nd order wave, the 2nd order free wave develops its own bound wave at the double frequency.

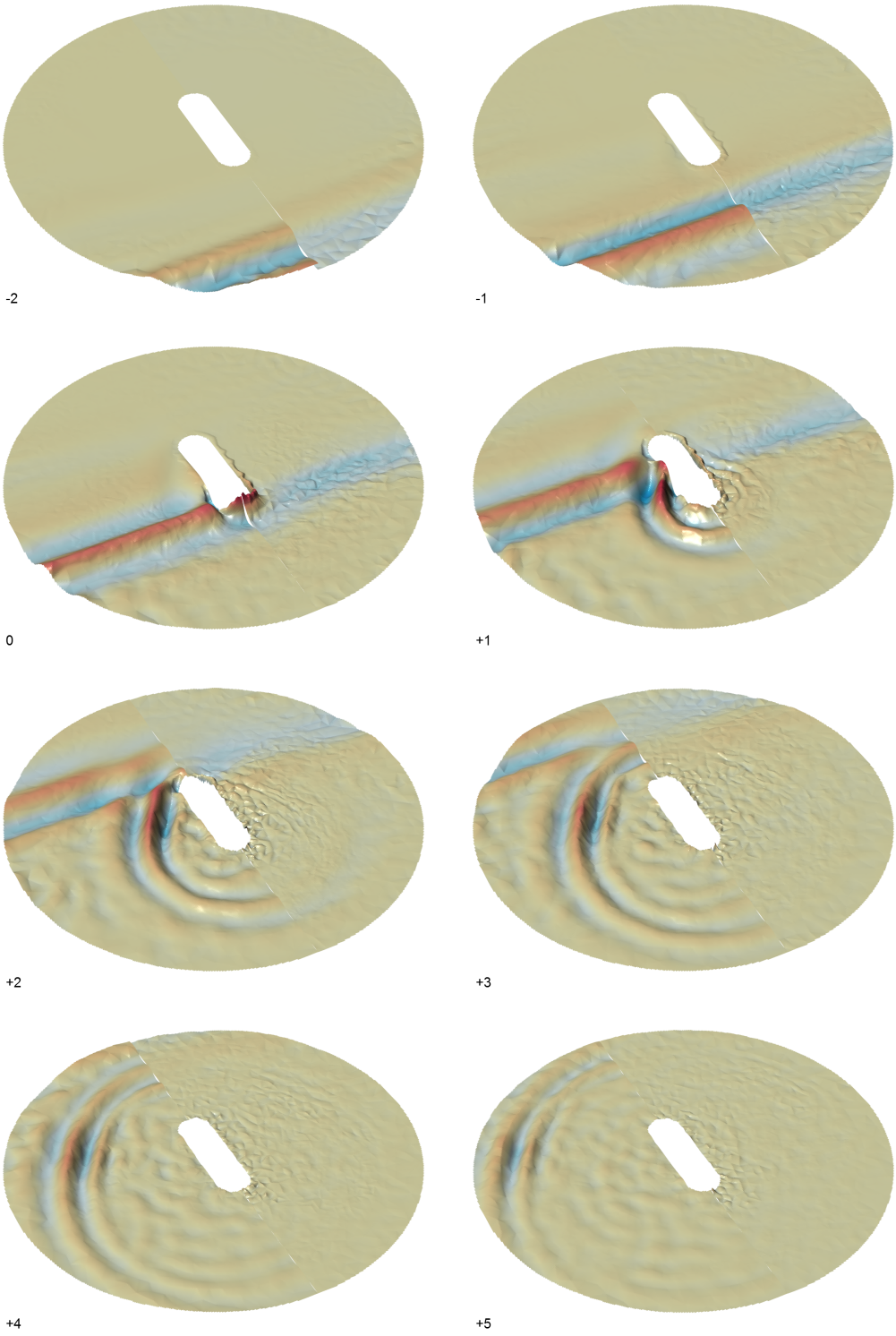

Figure 50: Second order sum (22, left) and difference (20, right)

6.6.4 Third Order Components

We now turn our attention to the nonlinear behaviour at third order. The 3rd order behaviour is found by taking the series of odd harmonics from $(C - T)/2$, and removing the linear term. The linear term can be calculated by performing a simulation at very small amplitude.

Figure 51 shows both the 3rd order components, but is dominated by the longer wavelength η_{31} term. There is an important 3rd order interaction which increases the speed of a steep wave. The wave seen travelling past the FPSO in figure 51 can best be understood as a phase shift. As the incident wave travels it deviates further from the linear position, and the 3rd order phase shift term increases. It can be seen to be much larger at +3 seconds than it is at focus. The radiated wave seen best at +2 seconds is a phase shift of the linear diffraction.

It may be recalled that the generation procedure is only correct to 3rd order. While the wave in the clear region propagates according to the full nonlinear behaviour, in the generation region the wave is prevented from travelling at full speed. This can be seen at the edge of the displayed area, particularly at the focus time. The η_{31} term is larger down the centre of the tank than it is at the edges, because at the edges it is being pegged back to the requested wave which travels slightly too slowly.

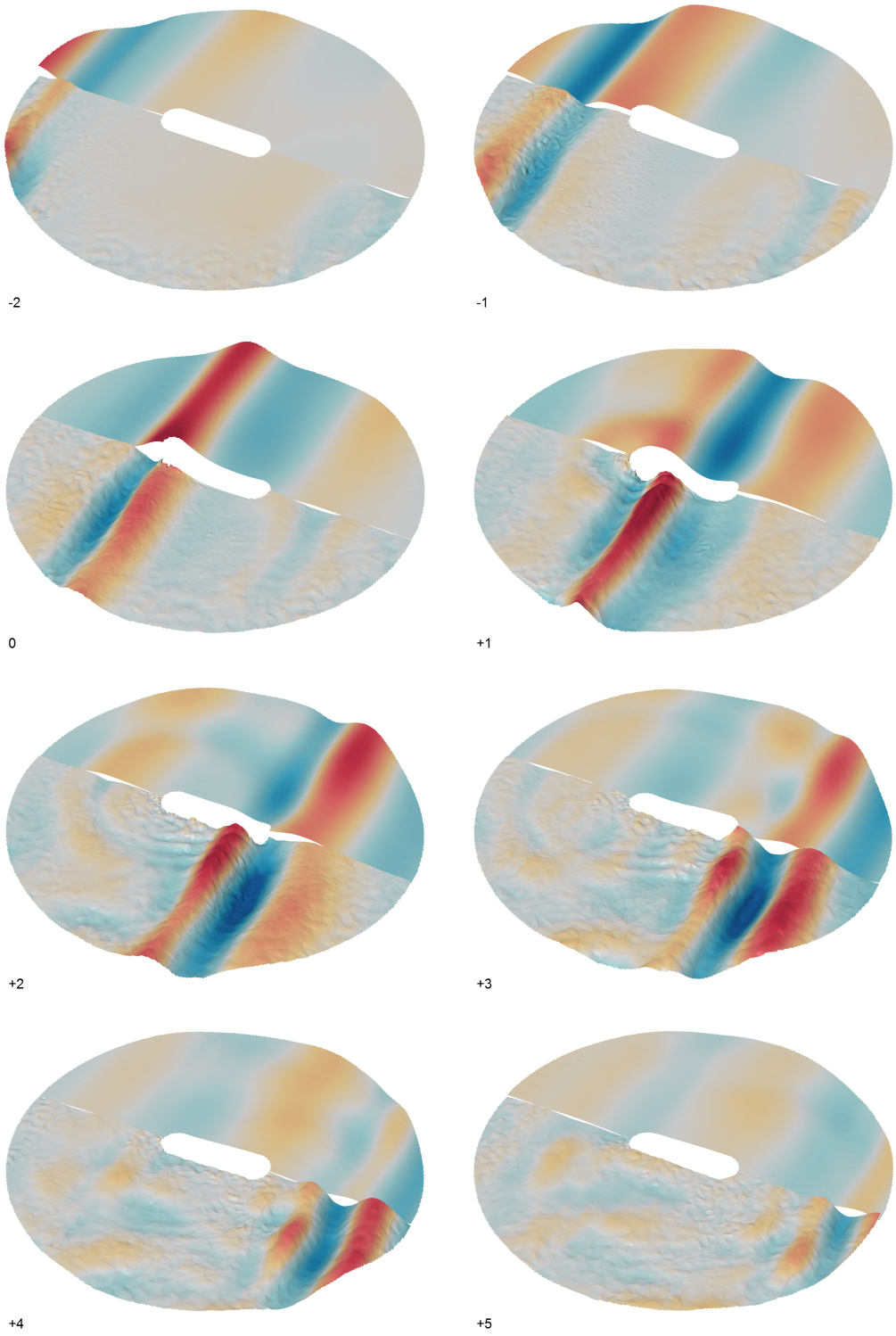

Figure 51: Third order components (31+33, below) and linear component (11, above)

6.6.5 Third Order Sum with Second Order Difference

Because the η_{31} term can grow so large, figure 51 was not useful for understanding the behaviour of the η_{33} term. To separate this we perform new simulations with phase shifts of 120° and 240°. This provides us with the combination $\eta_{20} + \eta_{33}$. The presence of the 2nd order difference term here is not too problematic as we already understand its behaviour.

Figure 52 shows a comparison of this third order combination in the lower half with the even harmonics discussed previously in the upper half. We can see the bound 2nd order difference set-down and set-up at focus familiar from figure 50. There appears to be a bound 3rd order term travelling with the wave group. At +1,+2 and +3 seconds the 3rd order radiated waves are visible. These are free waves, as they travel far slower than the incident group, and slower even than the 2nd order free waves.

The 3rd order radiation pattern bears some similarity to the 2nd order radiation. It is notable that there is almost no radiation in the upstream direction at all. This might have been expected from the spectrum of elevation at the bow shown in figure 34. The largest radiation is to the side and downstream, though more sideways than with the 2nd order radiation.

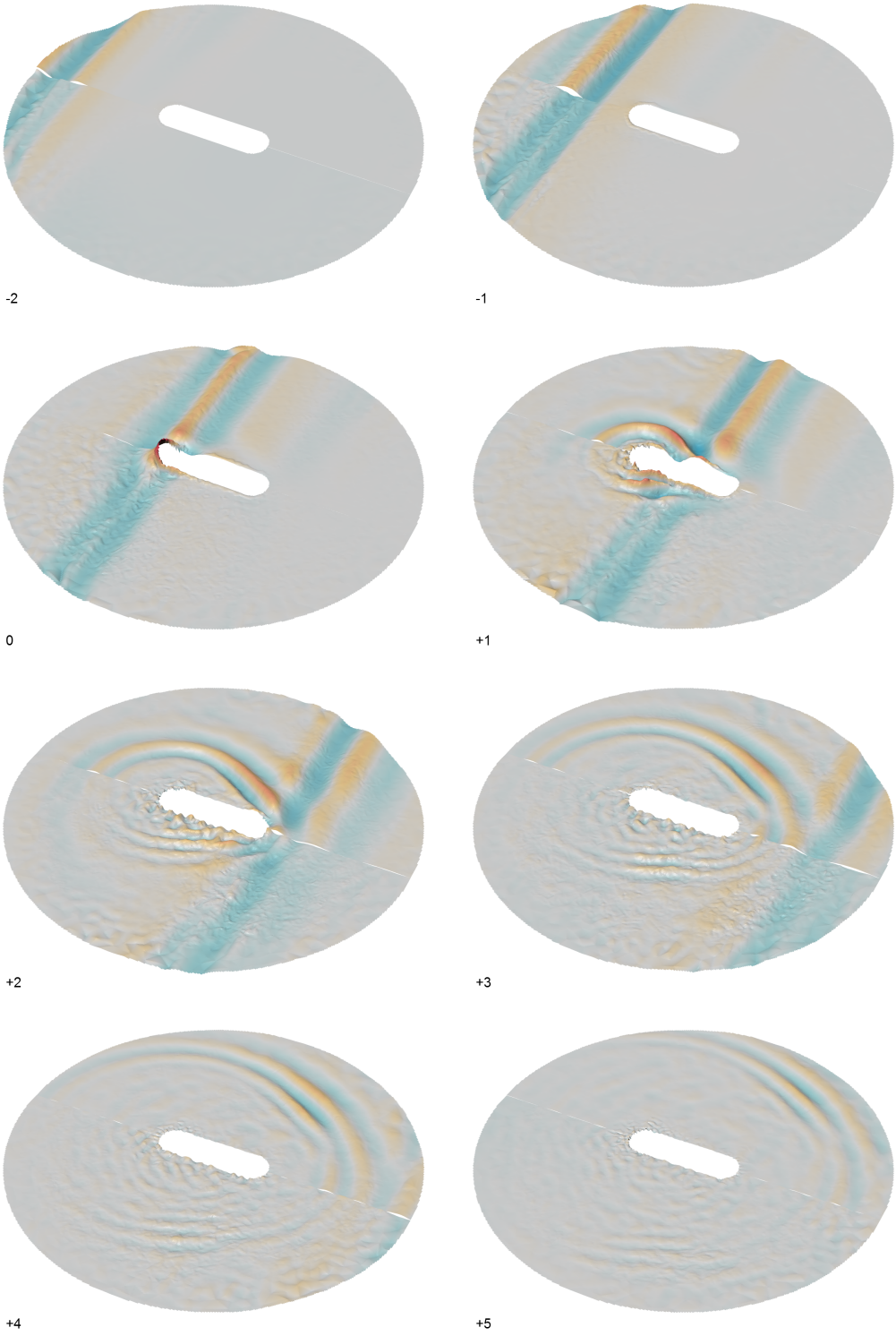

Figure 52: Triple harmonics (20+33, below) against even harmonics (20+22, above)

7 Conclusions and Recommendations for Future Work

Boundary integral methods are found to be computationally viable for high resolution fully nonlinear simulation. We achieved good comparisons to three different sets of experimental data: a bottom mounted cylinder, an oscillating cone, and an FPSO model. These three simple geometries cover the main physical features which may be present in a real FPSO.

The numerical simulation allows analysis of the high harmonics which are created by nonlinear diffraction or radiation. This analysis clarifies the physics of the wave tank experiments. Whereas a physical experiment is limited by the number of probes recording elevation data, the simulation allows the elevation at any point to be calculated in post-processing. The surface velocity data is also readily available, though not presented in this work. The calculation of force requires an additional BEM calculation, which was not performed for the FPSO model.

We were able to perform high resolution simulations even without a working parallel implementation of the Fast Multipole Method. This would greatly reduce the computational effort required, enabling larger and longer simulations. Implementing the FMM should be considered a priority before any large-scale numerical investigations are performed.

Issues with surface stability are a problem with all surface-fitting methods, and are particularly problematic with the BEM. Despite much effort, we were unable to improve on the stability of the method at the intersection line. The origin of this instability is partly due to the highly non-linear physical behaviour, and partly due to the poor resolution of these short wavenumber terms by the BEM. This buildup of noise which remains near the body can be seen in the free

surface in figures 50 and 52, where the larger linear wave has been removed, and in the frequency spectrum at the bow in figure 41.

A desingularized integral equation was demonstrated to provide an improvement to the accuracy of the integration. The benefit for the computational cost of this method compared with alternatives such as adaptive integration has not been fully assessed. Unfortunately, for steep waves the dominant source of error is the intersection line, and the desingularized equation does not help at this location.

For steep waves and flared structures it is likely that a surface-capturing scheme may be required to provide robustness. It might be possible to combine the BEM with a more robust surface description. This could be performed by a domain decomposition, applying a surface-capturing scheme in the immediate vicinity of a vessel and the BEM elsewhere. Or hypothetically by using the surface-capturing scheme to produce a smooth sub-surface suitable for the BEM calculation, and then applying the calculated velocity back to the surface-capturing scheme for timestepping.

7.1 Wave Damping

Both experimental and previous numerical work are hindered by the problem of reflections from tank walls. This problem requires that either the wave tank is very large, or that the experiments are of short duration. With the method of wave damping described in this thesis, numerical work can make use of a very small (and hence high resolution) wave tank. Long simulations, such as random sea state testing, could also be performed.

We have performed some investigation regarding the ideal strength and shape of the damping function. Varying the strength of the damping appears to exhibit behaviour analogous to damped simple harmonic motion. For the shape of the

function we could not improve on the simple ramp, which has a constant gradient.

We have not performed any systematic study regarding the size of the uncontrolled clear region surrounding a body. Further work or convergence tests may be required to establish how much space is required. It might be the case that the size of the clear region depends mostly on the evanescent wave modes present in the simulation. These are the wave components which decay exponentially with distance from the body. The interaction of evanescent modes with the wave damping region is not fully understood.

7.2 Wave Generation

The generation of an incident wave has also been problematic for both experimental and numerical work. With the new method presented in this thesis we are able to reproduce a requested wave with high accuracy, within a very small tank. For moderate steepness, it was found that the incident wave should be accurate to second order, and this correction can be calculated from a linear spectrum. For very steep waves, accuracy to third or higher order may be required.

Further work is required to establish guidelines on the initial conditions, lead time, and size of the clear and controlled regions. A steep incident wave undergoes nonlinear interaction with the outgoing radiated wave, and this interaction must occur within the clear region for complete accuracy.

In this thesis we have restricted our attention to unidirectional waves only, and have not demonstrated the generation of any directionally spread incident waves. This is not a limitation on the method, which could be used to generate crossing sea states if required. We have used circular tanks in an attempt to emphasize that there is not a preferred direction.

We have made some progress towards the exact reproduction of waves observed in experiments. This procedure could be improved or even automated,

with checks to ensure that the simulated incident wave agrees with the requested incident wave, and that the requested incident wave reproduces the observations of the experimental incident wave. This would be further complicated by directionally spread experimental data.

8 Appendix

8.1 Calculation of Inverse Gradient

The following algorithm is used to calculate the rate of change of the velocity potential due to the wave damping/generation mechanism $\omega_0 \nabla_H^{-1} \gamma \nabla_H (\phi - \phi_0)$ which appears on the right hand side of equation (50).

1. Find the relative potential $\phi - \phi_0$ at each node, where $\phi(x, y)$ is the current potential, and $\phi_0(x, y)$ is the surface potential of the incident wave.

2. Find the relative horizontal velocity $\nabla_H (\phi - \phi_0)$ by numerical differentiation.

3. Multiply by the strength function $\gamma(x, y)$ to find the damped velocity $v_d = \gamma \nabla_H (\phi - \phi_0)$ at each node

4. Choose a central node in the clear region to be undamped, $\phi_d = 0$.

5. Order the nodes by distance to the central node.

6. Working outwards, for each new node m where the damping potential has not yet been found, find its N neighbours which have already been solved.

7. Calculate the average of N path integrals from each neighbouring node $\phi_d(\mathrm{m}) = \frac{1}{N} \sum_n \phi_d(n) + [0.5 (v_d(m) + v_d(n)) \cdot (X(m) - X(n))]$

8. Repeat until the damping potential $\phi_d = \nabla_H^{-1} \gamma \nabla_H (\phi - \phi_0)$ has been found at each node

9. Multiply by the frequency constant ω_0

8.2 Extraction of Nonlinear Components

For an incident wave group with amplitude A and relative phase θ, we assume a stokes expansion of elevation η in the form:

$$\begin{aligned}\eta(A,\theta) &= \eta_{11}A\cos\theta \\ &+ \eta_{20}A^2 + \eta_{22}A^2\cos 2\theta \\ &+ \eta_{31}A^3\cos\theta + \eta_{33}A^3\cos 3\theta \\ &+ \eta_{40}A^4 + \eta_{42}A^4\cos 2\theta + \eta_{44}A^4\cos 4\theta, \end{aligned} \tag{68}$$

Similar expansions may also be written for forces or velocities. By performing calculations with incident groups of varying phase, it is possible to extract some of the nonlinear components. This extraction may be completed by the use of frequency domain filtering, and in some cases application of amplitude scaling.

The following list contains some of the more useful combinations:

- $\left(\eta^0 - \eta^{180}\right)/2 = \eta_{11} + \eta_{31} + \eta_{33}$
- $\left(\eta^0 + \eta^{180}\right)/2 = \eta_{20} + \eta_{22} + \eta_{40} + \eta_{42} + \eta_{44}$
- $\left(\eta^0 + \eta^{120} + \eta^{240}\right)/3 = \eta_{20} + \eta_{33} + \eta_{40}$
- $\left(\eta^0 + \eta^{90} + \eta^{180} + \eta^{270}\right)/4 = \eta_{20} + \eta_{40} + \eta_{44}$
- $\left(\eta^0 - \eta^{90} + \eta^{180} - \eta^{270}\right)/4 = \eta_{22} + \eta_{42}$

From Fitzgerald et al. (2012), it is also possible to make use of the Hilbert transform $H()$ in order to extract the third order components:

- $\left(\eta_0 - H\left(\eta_{90}\right) - \eta_{180} + H\left(\eta_{270}\right)\right)/4 = \eta_{11} + \eta_{31}$
- $\left(\eta_0 + H\left(\eta_{90}\right) - \eta_{180} - H\left(\eta_{270}\right)\right)/4 = \eta_{33}$

The author would like to acknowledge the use of the Oxford Supercomputing Centre (OSC) in carrying out this work

References

Adcock, T. A. A., Taylor, P. H., Yan, S., Ma, Q. W., and Janssen, P. A. E. M. (2011). Did the Draupner wave occur in a crossing sea? *Proceedings of the Royal Society A*.

Akkerman, I., Bazilevs, Y., Benson, D. J., Farthing, M. W., and Kees, C. E. (2012). free-surface flow and fluid-object interaction modeling with emphasis on ship hydrodynamics. *Journal of Applied Mechanics-Transactions of the ASME*, 79(1).

Bai, W. and Eatock Taylor, R. (2006). Higher-order boundary element simulation of fully nonlinear wave radiation by oscillating vertical cylinders. *Applied Ocean Research*, 28:247–265.

Bai, W. and Eatock Taylor, R. (2007). Numerical simulation of fully nonlinear regular and focused wave diffraction around a vertical cylinder using domain decomposition. *Applied Ocean Research*, 29(1-2):55–71.

Bai, W. and Eatock Taylor, R. (2009). Fully nonlinear simulation of wave interaction with fixed and floating flared structures. *Ocean Engineering*, 36(3-4):223–236.

Boccotti, P. (1983). Some new results on statistical properties of wind waves. *Applied Ocean Research*, 5(3):134–140.

Boo, S. (2002). Linear and nonlinear irregular waves and forces in a numerical wave tank. *Ocean Engineering*, 29(5):475–493.

Borgarino, B., Babarit, A., and Ferrant, P. (2011). Implementing a fast multipole algorithm into the diffraction/radiation software Aquaplus. *Houille Blanche-Revue Internationale de l'Eau*, (4):13–18.

Buldakov, E., Eatock Taylor, R., and Taylor, P. H. (2004). Local and far-field surface elevation around a vertical cylinder in unidirectional steep wave groups. *Ocean Engineering*, 31(7):833–864.

Celebi, M. S., Kim, M. H., and Beck, R. F. (1998). Fully nonlinear 3-D numerical wave tank simulation. *Journal of Ship Research*, 42(1):33–45.

Cho, I. H. and Kim, M. H. (2008). Wave absorbing system using inclined perforated plates. *Journal of Fluid Mechanics*, 608:1–20.

Clamond, D., Fructus, D., and Grue, J. (2007). A note on time integrators in water-wave simulations. *Journal of Engineering Mathematics*, 58(1-4):149–156.

Clamond, D., Fructus, D., Grue, J., and Kristiansen, O. (2005). An efficient model for three-dimensional surface wave simulations. part II: generation and absorption. *Journal of Computational Physics*, 205(2):686–705.

Clement, A. (1996). Coupling of two absorbing boundary conditions for 2D time-domain simulations of free surface gravity waves. *Journal of Computational Physics*, 126(1):139–151.

Cruz, F. A., Knepley, M. G., and Barba, L. A. (2010). Petfmm - a dynamically load-balancing parallel fast multipole library. *International Journal for Numerical Methods in Engineering*, 85(4):403–428.

Dalzell, J. F. (1999). A note on finite depth second-order wave-wave interactions. *Applied Ocean Research*, 21(3):105–111.

Dean, R. G. and Dalrymple, R. A. (1991). *Water wave mechanics for engineers and scientists*. World Scientific.

Dias, F. and Bridges, T. J. (2006). The numerical computation of freely propagating time-dependent irrotational water waves. *Fluid Dynamics Research*, 38(12):803–830.

Drake, K. R., Eatock Taylor, R., Taylor, P. H., and Bai, W. (2009). On the hydrodynamics of bobbing cones. *Ocean Engineering*, 36(15-16):1270–1277.

Duclos, G., Clement, A. H., and Chatry, G. (2001). Absorption of outgoing waves in a numerical wave tank using a self-adaptive boundary condition. *International Journal of Offshore and Polar Engineering*, 11(3):168–175.

Dysthe, K. B., Krogstad, H. E., and Müller, P. (2008). Oceanic rogue waves. *Annual Review of Fluid Mechanics*, 40:287–310.

Eatock Taylor, R. and Chau, F. P. (1992). Wave diffraction theory - some developments in linear and non-linear theory. *Journal of Offshore Mechanical and Arctic Engineering*, 114:185–194.

Eatock Taylor, R., Wu, G. X., Bai, W., and Hu, Z. Z. (2008). Numerical wave tanks based on finte element and boundary element modeling. *Journal of Offshore Mechanics and Arctic Engineering*, 130(3):031001.

Elias, R. N., Goncalves, M. A., Coutinho, A. L. G. A., Esperanca, P. T. T., Martins, M. A. D., and Ferreira, M. D. A. S. (2009). Computational techniques for stabilized edge-based finite element simulation of nonlinear free-surface flows. *Journal of Offshore Mechanics and Arctic Engineering-Transactions of the Asme*, 131(4).

Fenton, J. D. (1985). A fifth order stokes theory for steady waves.

Ferrant, P., Le Touzé, D., and Pelletier, K. (2003). Non-linear time-domain models for irregular wave diffraction about offshore structures. *International Journal for Numerical Methods in Fluids*, 43(10-11):1257–1277.

Fitzgerald, C., Grice, J., Taylor, P. H., Eatock Taylor, R., and Zang, J. (2012). Phase manipulation and the harmonic components of ringing forces on a surface-piercing column. *IWWWFB, Copenhagen, Denamrk*.

Fochesato, C. and Dias, F. (2006). A fast method for nonlinear three-dimensional free-surface waves. *Proceedings of the Royal Society - Mathematical Physical and Engineering Sciences*, 462(2073):2715–2735.

Fochesato, C., Grilli, S. T., and Guyenne, P. (2005). Note on non-orthogonality of local curvilinear co-ordinates in a three-dimensional boundary element method. *International Journal for Numerical Methods in Fluids*, 48(3):305–324.

Gorf, P., Barltrop, N., Okan, B., Hodgson, T., and Rainey, R. (2000). FPSO bow damage in steep waves. *Rogue waves 2000, Brest, France*.

Greengard, L. and Gropp, W. D. (1990). A parallel version of the fast multipole method. *Computers and Mathematics with Applications*.

Greengard, L. and Rokhlin, V. (1987). A fast algorithm for particle simulations. *Journal of Computational Physics*, 73:315–348.

Greengard, L. and Rokhlin, V. (1997). A new version of the fast multipole method for the Laplace equation in three dimensions. *Acta Numerica*, 6:229–269269.

Grilli, S. T., Guyenne, P., and Dias, F. (2001). A fully non-linear model for three-dimensional overturning waves over an arbitrary bottom. *International Journal for Numerical Methods in Fluids*, 35(7):829–867.

Grilli, S. T. and Svendsen, I. A. (1990). Corner problems and global accuracy in the boundary element solution of nonlinear wave flows. *Engineering Analysis with Boundary Elements*, 7(4):178–195.

Hagen, O. (2002). Statistics for the Draupner January 1995 freak wave event. *In Proceedings of the OMAE, Oslo, Norway*.

Hamano, K., Murashige, S., and Hayami, K. (2003). Boundary element simulation of large amplitude standing waves in vessels. *Engineering Analysis with Boundary Elements*, 27(6):565–574.

Hasselmann, K., Barnett, T. P., Bouws, E., Carlson, H., Cartwright, D. E., Enke, K., Ewing, J. A., Gienapp, H., Hasselmann, D. E., Kruseman, P., Meerburg, A., Müller, P., Olbers, D., Richter, K., Sell, W., and Walden, H. (1973). Measurement of wind-wave growth and swell decay during the joint north sea wave project (JONSWAP). *Deutschen Hydrographischen Zeitschrift*, 8–12.

Health and Safety Executive (2000). Offshore Technology Report - Review of green water and wave slam design and specification requirements for FPSO/FSU's. Prepared by PAFA Consulting Engineers Ltd.

Jonathan, P. and Taylor, P. H. (1997). On irregular, non-linear waves in a spread sea. *Journal of Offshore Mechanics and Arctic Engineering*, 119:37–41.

Joseph, D., Funada, T., and Wang, J. (2007). *Potential flows in viscous and viscoelastic liquids*. Cambridge University Press.

Keulegan, G. H. and Carpenter, L. H. (1958). Force on cylinders and plates in an oscillating fluid. *Journal of Res Natl. Bur. Stand*, 60(5):423–440.

Kharif, C. and Pelinovsky, E. (2003). Physical mechanisms of the rogue wave phenomenon. *European Journal of Mechanics - BFluids*, 22:603–634.

Kim, M. H., Celebi, M. S., and Kim, D. J. (1998). Fully nonlinear interactions of waves with a three-dimensional body in uniform currents. *Applied Ocean Research*, 20:309–321.

Kwon, S. H., Moon, W. M., and Lee, H. S. (2003). Experimental and numerical studies on the development of a new wave absorber. *Ocean Engineering*, 30(2):185–203.

Lee, K. H. and Mizutani, N. (2009). A numerical wave tank using direct-forcing immersed boundary method and its application to wave force on a horizontal cylinder. *Coastal Engineering Journal*, 51(1):27–48.

Lin, P. (2008). *Numerical Modelling of Water Waves: An introduction to engineers and scientists*. Taylor & Francis.

Lindgren, G. (1970). Some properties of a normal process near a local maximum. *Annals of Mathematical Statistics*, 41:1870–1883.

Liu, Y. J. (2009). *Fast multipole boundary element method: Theory and applications in engineering*. Cambridge University Press, 1 edition.

Liu, Y. J. and Rudolphi, T. J. (1999). New identities for fundamental solutions and their applications to non-singular boundary element formulations. *Computational Mechanics*, 24:286–292.

Liu, Y. M., Xue, M., and Yue, D. K. P. (2001). Computations of fully nonlinear three-dimensional wave-wave and wave-body interactions. part 2. nonlinear waves and forces on a body. *Journal of Fluid Mechanics*, 438:41–66.

Longuet-Higgins, M. S. (1962). Resonant interactions between two trains of gravity waves. *Journal of Fluid Mechanics*, 12:321–332.

Ma, Q. W., Wu, G. X., and Eatock Taylor, R. (2001). Finite element simulation of fully non-linear interaction between vertical cylinders and steep waves. part 1: Methodology and numerical procedure. *International Journal for Numerical Methods in Fluids*, 36(3):265–285.

Ma, Q. W. and Yan, S. (2006). Quasi-ALE finite element method for nonlinear water waves. *Journal of Computational Physics*, 212(1):52–72.

Ma, Q. W. and Yan, S. (2009). QALE-FEM for numerical modelling of non-linear interaction between 3D moored floating bodies and steep waves. *International Journal for Numerical Methods in Engineering*, 78(6):713–756.

Ning, D. Z., Teng, B., Zhao, H. T., and Hao, C. L. (2010). A comparison of two methods for calculating solid angle coefficients in a BIEM numerical wave tank. *Engineering Analysis with Boundary Elements*, 34(1):92–96.

Shen, L. and Liu, Y. J. (2007). An adaptive fast multipole boundary element method for three-dimensional potential problems. *Computational Mechanics*, 39(6):681–691.

Shewchuk, J. R. (1996). Triangle: Engineering a 2D quality mesh generator and Delaunay triangulator. In Lin, M. C. and Manocha, D., editors, *Applied Computational Geometry: Towards Geometric Engineering*, volume 1148 of *Lecture Notes in Computer Science*, pages 203–222. Springer-Verlag.

Sun, H. and Faltinsen, O. M. (2009). Water entry of a bow-flare ship section with roll angle. *Journal of Marine Science and Technology*, 14(1):69–79.

Sung, H. G. and Grilli, S. T. (2008). BEM computations of 3-D fully nonlinear free-surface flows caused by advancing surface disturbances. *International Journal of Offshore and Polar Engineering*, 18(4):292–301.

Takizawa, K., Yabe, T., Tsugawa, Y., Tezduyar, T. E., and Mizoe, H. (2007). Computation of free-surface flows and fluid-object interactions with the CIP method based on adaptive meshless soroban grids. *Computational Mechanics*, 40(1):167–183.

Tromans, P. S., Anaturk, A. R., and Hagemeijer, P. (1991). A new model for the kinematics of large ocean waves: Application as a design wave. *In Proccedings of the ISOPE, Edinburgh, UK*, 3:64–71.

Tsai, W. T. and Yue, D. K. P. (1996). Computation of nonlinear free-surface flows. *Annual Review of Fluid Mechanics*, 28:249–278.

Utsunomiya, T., Watanabe, E., and Nishimura, N. (2001). Fast multipole method for hydrodynamic analysis of very large floating structures. *IWWWFB, Hiroshima, Japan.*

Walker, D. A. G. (2006). Interaction of extreme ocean waves with offshore structures. *D.Phil thesis, University of Oxford.*

Wang, C. Z. and Wu, G. X. (2006). An unstructured-mesh-based finite element simulation of wave interactions with non-wall-sided bodies. *Journal of Fluids and Structures*, 22(4):441–461.

Wang, C. Z., Wu, G. X., and Drake, K. R. (2007). Interactions between nonlinear water waves and non-wall-sided 3D structures. *Ocean Engineering*, 34(8-9):1182–1196.

Westphalen, J., Greaves, D. M., Williams, C. J. K., Hunt-Raby, A. C., and Zang, J. (2012). Focused waves and wave-structure interaction in a numerical wave tank. *Ocean Engineering*, 45:9–21.

Whitman, G. B. (1974). *Linear and nonlinear waves.* Wiley Interscience.

Wu, G. X. (1998). Hydrodynamic force on a rigid body during impact with liquid. *Journal of Fluids and Structures*, 12:549–559.

Wu, G. X. and Eatock Taylor, R. (1996). Transient motion of a floating body in steep waves. *IWWWFB, Hamburg, Germany.*

Wu, G. X., Eatock Taylor, R., and Greaves, D. M. (2001). The effect of viscosity on the transient free-surface waves in a two-dimensional tank. *Journal of Engineering Mathematics*, 40:77–90.

Yeung, R. W. and Yu, X. (1995). Wave-structure interaction in a viscous fluid. *Fourteenth Intenational Conference on Offshore Mechanical and Arctic Engineering, Copenhagen, Denmark.*

Ying, L. X., Biros, G., and Zorin, D. (2004). A kernel-independent adaptive fast multipole algorithm in two and three dimensions. *Journal of Computational Physics*, 196(2):591–626.

Zang, J., Gibson, R., Taylor, P. H., Eatock Taylor, R., and Swan, C. (2006). Second order wave diffraction around a fixed ship-shaped body in unidirectional steep waves. *Journal of Offshore Mechanics and Arctic Engineering*, 128(2):89.

Zang, J., Taylor, P. H., Morgan, G., Tello, M., and Orszaghova, J. (2010). Experimental study of non-linear wave impact on offshore wind turbine foundations. *Proc. 3rd Int. Conf. on the application of physical modelling to port and coastal protection, Coastlab.*

Zhang, Y., Zou, Q., and Greaves, D. (2012). Air-water two-phase flow modelling of hydrodynamic performance of an oscillating water column device. *Renewable Energy*, 41:159–170.